

AD-A107 604

SINGER CO LITTLE FALLS NJ KEARFOTT DIV

F/6 20/8

RELAXATION PHENOMENA IN OPTICALLY PUMPED MERCURY ISOTOPES.(U)

AUG 81 J H SIMPSON, P A HEIMANN, M J KELLY

F49620-76-C-0009

UNCLASSIFIED

KO-81-15

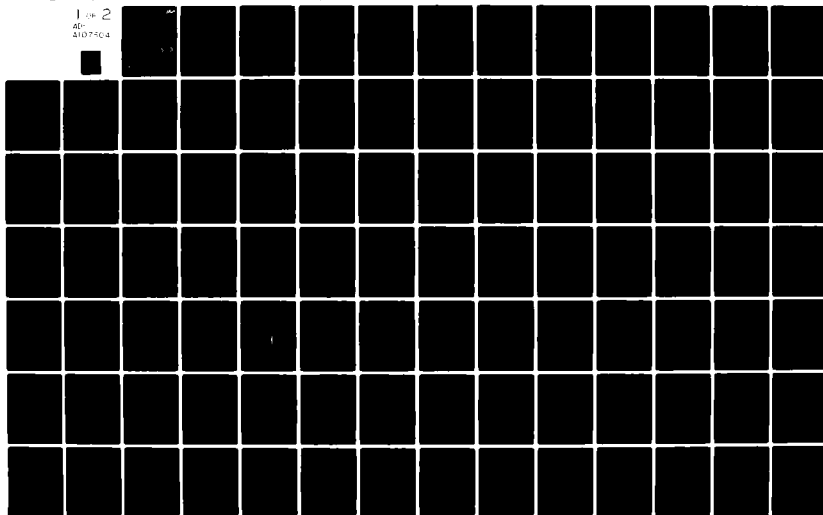
AFOSR-TR-81-0724

NL

1 OF 2

AD-

A107404



UNCLASSIFIED

LEVEL II

12

SECURITY CLASSIFICATION OF THIS PAGE (When Data Entered)

REPORT DOCUMENTATION PAGE		READ INSTRUCTIONS BEFORE COMPLETING FORM
1. REPORT NUMBER AFOSR-TR- 81 -0724	2. GOVT ACCESSION NO.	3. RECIPIENT'S CATALOG NUMBER
4. TITLE (and Subtitle) Relaxation Phenomena in Optically Pumped Mercury Isotopes		5. TYPE OF REPORT & PERIOD COVERED Final Scientific Report 1 Jul. '76 to 30 Jun. '81
7. AUTHOR(s) J.H. Simpson, P.A. Heimann, M.J. Kelly, D.I. Shernoff		6. PERFORMING ORG. REPORT NUMBER KD-81-15
9. PERFORMING ORGANIZATION NAME AND ADDRESS The Singer Co., Kearfott Div. 1225 McBride Avenue Little Falls, N.J. 07424		8. CONTRACT OR GRANT NUMBER(s) F49260-76-C-0009
11. CONTROLLING OFFICE NAME AND ADDRESS Air Force Office of Scientific Research Building 410, Bolling AFB Washington, D.C. 20332		10. PROGRAM ELEMENT, PROJECT, TASK AREA & WORK UNIT NUMBERS 61104F 2301/A4
14. MONITORING AGENCY NAME & ADDRESS (if different from Controlling Office)		12. REPORT DATE August 31, 1981
		13. NUMBER OF PAGES 102 pages
		15. SECURITY CLASS. (of this report) Unclassified
		15a. DECLASSIFICATION DOWNGRADING SCHEDULE
16. DISTRIBUTION STATEMENT (of this Report) Approved for public release; distribution unlimited.		
17. DISTRIBUTION STATEMENT (of the abstract entered in Block 20, if different from Report) <div style="text-align: right;">DTIC ELECTE NOV 20 1981 D</div>		
18. SUPPLEMENTARY NOTES		
19. KEY WORDS (Continue on reverse side if necessary and identify by block number) Transmittance, Density Measurement, Adsorption, Activation Energy, Quartz, Mercury Lamps, Dipole Moment, Magnetic Relaxation, Optical Pumping, Nuclear Magnetic Resonance, Mercury Isotopes, Quadrupole Moment, Perturbation, Mercury (Metal), Metal Vapors, (continued)		
20. ABSTRACT (Continue on reverse side if necessary and identify by block number) Relaxation measurements of optically pumped ¹⁹⁹ Hg and ²⁰¹ Hg in nuclear magnetic resonance (NMR) cells have shown that the acti- vation energy for adsorption of ground state mercury atoms ranged from .22 eV to .24 eV for a variety of materials. These measure- ments also provided a means of determining the temperature depen- dence of the product of concentration and strength of paramagnetic (continued)		

AD A107604

DTIC FILE COPY

DD FORM 1473 EDITION OF 1 NOV 65 IS OBSOLETE

81 11 10 071

UNCLASSIFIED

SECURITY CLASSIFICATION OF THIS PAGE (When Data Entered)

19 (Continued)

Silicon Dioxide, Surface Properties, Ultraviolet Radiation,
Nuclear Spin, Gyroscopes

20 (Continued)

centers on the inner cell surfaces.

The origins and effects of both randomly-fluctuating and steady-state quadrupole perturbations on ^{201}Hg have been clarified. A calculation predicts that the relaxation rate of ^{201}Hg in a cube-shaped cell should be independent of cell orientation. This prediction was verified experimentally. Another calculation, which modelled ^{201}Hg as a single four-level spin system, predicted a functional form for the non-exponential decay of ^{201}Hg in the presence of a quadrupole perturbation. These predictions were also verified experimentally.

Techniques have been developed for producing mercury NMR cells with long relaxation times and stable characteristics.

Accession For	
NTIS GRA&I	<input checked="checked" type="checkbox"/>
DTIC TAB	<input type="checkbox"/>
Unannounced	<input type="checkbox"/>
Justification	
By	
Distribution/	
Availability Codes	
Dist	Avail and/or Special
A	

TABLE OF CONTENTS

	<u>PAGE</u>
LIST OF FIGURES	iii
LIST OF TABLES	v
1. INTRODUCTION	1
2. CELL FABRICATION AND PROCESSING	3
3. CELL TESTING - EXPERIMENTAL METHOD	8
4. INTERPRETATION OF RELAXATION AND ABSORPTION MEASUREMENTS IN NMR CELLS	13
4.1 REVIEW OF MERCURY-WALL INTERACTION	14
4.2 SILICA SURFACE MODEL	15
4.3 VAPORS IN THE CELLS	22
4.4 INTERPRETATION OF RELAXATION MEASUREMENTS	23
4.5 INTERPRETATION OF RESONANT LIGHT TRANSMITTANCE MEASUREMENTS	39
4.6 COMPARISON OF CELL WALL MATERIAL	48
5. COMPLEMENTARY INVESTIGATIONS	50
5.1 ADSORPTION MEASUREMENTS OF MERCURY ON SILICA POWDER	50
5.2 CHEMISORPTION OF MERCURY ON SILICA POWDER	57
5.3 SURFACE ANALYSIS OF CELL WALL MATERIALS	61
5.4 SILICA GLASSBLOWER'S SMOKE	64
5.5 THE DARK FILM IN MERCURY LAMPS	65
6. QUADRUPOLE EFFECTS UPON THE ^{201}Hg MAGNETIC RESONANCE	66
6.1 INTRODUCTION	66
6.2 QUADRUPOLE PERTURBATIONS DUE TO THE CELL WALL	67
6.3 COMBINED QUADRUPOLE PERTURBATION/TRANSVERSE MAGNETIC FIELD/PUMPING RADIATION/RELAXATION	71
6.4 RELAXATION DUE TO A FLUCTUATING ANISOTROPIC PERTURBATION	76
7. CONCLUSIONS	78

	<u>PAGE</u>
8. REFERENCES	80
9. PUBLICATIONS	82

APPENDIX: RESEARCH OBJECTIVES & PERSONNEL

LIST OF FIGURES

<u>FIGURE</u>	<u>TITLE</u>	<u>PAGE</u>
1	Diagram of Vacuum System	5
2	Cell Test Apparatus	9
3	^{201}Hg and ^{199}Hg Relaxation Times vs Temperature for Two NMR Cells	12
4	Surface States of Fused Silica	16
5	Activation Energy Plots for Several Materials	29
6	Paramagnetic Center Concentration vs Temperature for Several Materials	31
7	Effects of Heat Treatments on τ_{201q} of Cell W-134	33
8	Effects of Heat Treatments on PMC Concentration of Cell W-134	34
9	Activation Energy Plot for Cell W-111	37
10	Calculated Variation of Transmittance with Vapor Density for a 1 cm Path Length	41
11	Transmittance Measurement Apparatus	42
12	Transmittance of Wet Cell vs Reservoir Temperature	44
13	Mercury Vapor Density vs Pump Beam Exposure for Cell W-123	47
14	Apparatus for Adsorption Experiment	52
15	Changes in Mercury Vapor Density During Mercury-Silica Adsorption Experiment	54
16	Infrared Transmittance Spectrum of Powdered Silica	58
17	Sample Holder for Infrared Transmittance Measurement Under Vacuum	60
18	Expanded-Wavelength Infrared Transmittance Spectrum of Powdered Silica Showing Surface Silanol Absorption Band	62

<u>FIGURE</u>	<u>TITLE</u>	<u>PAGE</u>
19	Angular Dependence of Quadrupole Terms (Arbitrary Scale)	68
20	Electric Field Near an Adsorbed Atom	69
21	Coupled Differential Equations	73

LIST OF TABLES

<u>TABLE</u>	<u>TITLE</u>	<u>PAGE</u>
1	Metallic Impurities in Suprasil W	20
2	Heat Treatments Received by Cell W-134	32
3	Comparison of Cell Wall Materials	49
4	Characteristics of Certain Cell Geometries	77

1. INTRODUCTION

This final scientific report describes the work supported by AFOSR Contract No. F49260-76-C-0009 from July 1, 1977 to August 31, 1981 and is a continuation of a four year effort from June 1, 1972 to June 30, 1976 supported by AFOSR Contract No. F44620-72-C-0047.¹

The program is concerned with obtaining a better understanding of the factors that affect the vapor density and the nuclear magnetic resonance (NMR) relaxation of two isotopes, ^{199}Hg and ^{201}Hg , of vapor-phase mercury in contact with the walls of a NMR cell. Knowledge of these factors will facilitate the fabrication of NMR cells with the desired characteristics of predictable and stable mercury vapor density, optimized and stable NMR signal levels, and optimized and stable relaxation times. The technique of orientation by optical pumping is employed to enhance the net nuclear magnetic moment, and optical techniques are used to monitor the dynamics of the nuclear spin system and the mercury vapor density.

The NMR cells used in this project have consisted of an ultraviolet-transmitting envelope, containing a small quantity of ^{199}Hg and ^{201}Hg in approximately equal amounts. A variety of ultraviolet-transmitting glasses, including natural fused silica, synthetic fused silica, and Corning 9741 Pyrex, have been used as envelope material. A high-purity, water-free fused silica, Suprasil W produced by Amersil Inc. has been the envelope material on which most observations have been made.

The amount of mercury introduced into each cell is controlled so that, at normal operating temperatures, no liquid droplet of mercury exists in the cell. Most of the mercury is in the vapor phase. Since the vapor density is low, the mean free path is larger than the cell dimensions. No buffer gas is intentionally introduced into the cell. Impurities are kept to a minimum. Under these conditions, the mercury atoms in the NMR cells are assumed to interact primarily

with the surface of high-purity, fused silica.

The fabrication and processing of the NMR cells is described in Section 2. The apparatus and techniques used in cell testing appear in Section 3. The theory and results of relaxation and vapor density measurements in NMR cells are given in Section 4. The results of complementary studies are presented in Section 5. These studies were performed for the purpose of providing additional or confirming information about mercury-silica interactions. The effects of quadrupole perturbations on the ^{201}Hg resonance and the information it provides about mercury-wall interactions appear in Section 6. The general conclusions are presented in Section 7.

During the course of this program it has been evident that NMR signals from optically oriented mercury nuclei reveal information about surface conditions that are not detectable currently by other means; surfaces that interact strongly with oriented mercury nuclei appear featureless under ESCA and SEM probing, for example. These interactions, which can produce splitting, and/or shifting of resonance frequencies and relaxation of the NMR signals, can be used to probe and analyze surfaces.

One inherent attribute of NMR signals as a surface probe is that the effective Q of the signals increases as the surface becomes less interacting. This allows weakly interacting surfaces to be probed with a matching increase in sensitivity.

2. CELL FABRICATION AND PROCESSING

Over a period of years, procedures have been developed to make NMR cells with a minimum of contamination. This has resulted in cells with strong signals and very long relaxation times and with reproducible characteristics. Since cell characteristics are so strongly affected by the preparation, these procedures will be described in detail.

The general operations involved in making NMR cells are:

- 1) Cleaning the stock material,
- 2) Fabrication of cell blanks and cell manifold assemblies,
- 3) Vacuum system cleaning of the glassware and the mercury,
- 4) Introducing a specified amount of mercury in the cells, and
- 5) Sealing off individual cells.

The stock material is cleaned by being scrubbed with a brush and a solution of Scrub Cleaner No.11, an alkaline abrasive agent of the Shipley Co. Inc. The mechanical action loosens and removes bulk dirt, while the cleaner chemically removes oils, greases, and soils. The material is then rinsed with distilled water and soaked in a 50% nitric acid solution for 30 minutes. This removes traces of the cleaner as well as traces of many hydroxides, oxides, and metals. The material is rinsed again with distilled water and blown dry with nitrogen.

In the glassblowing operations, controlled nitrogen pressure is used in place of the glassblower's breath. Other gases such as argon and oxygen were tried in place of the nitrogen for the fabrication of cell blanks to determine if their use would produce any effect on the cell wall characteristics; no effect was observed. Nitrogen is used in preference to argon because it is more easily removed from the vacuum system by the ionization pump. Heat is provided by an oxygen and natural gas flame from a surface-mix hand torch. The cell

blanks are typically 1 cm diameter spheres with a very narrow neck. Minimizing the size of the neck reduces cell contamination at seal-off and minimizes the geometrical quadrupole perturbation of the ^{201}Hg resonance (see Section 6). The spherical cell blanks are formed using a small lathe which allows them to be made highly uniform and to closely specified dimensions.

A diagram of the vacuum system is shown in Figure 1. The cell manifold and the rest of the diagrammed portion of the system is made from GE204 fused quartz, a high-purity, natural fused quartz made by General Electric. A quartz-to-metal seal connects this region to the rest of the system.

The configuration shown in Figure 1 is used only when a fresh supply of mercury is being introduced into the cell-making process and must be purified by multiple distillations. Only a small fraction of the mercury introduced into the vacuum system is actually needed to fill the cells with vapor, so that most of the mercury remains in the manifold tube after cell sealoff. After the individual cells are removed from the manifold, the manifold tube becomes a sealed ampoule containing clean mercury and can be attached to the vacuum system in place of the ampoule tube by means of the manifold attachment tube to provide predistilled mercury for filling subsequent batches of mercury cells. The auxiliary distillation tube and distillation cleaning procedure are then unnecessary.

Distillation cleaning is used when a fresh supply of mercury is being introduced. A droplet of the mercury is placed in region A and the vacuum system is pumped down by means of a Varian VacSorb sorption pump and a Varian VacIon ionization pump. The mercury is kept at about -60°C and the rest of the fused quartz region of the system is heated to $\sim 500^{\circ}\text{C}$ for several days until the residual system pressure falls below 10^{-7} torr. The system temperature is lowered to about 200°C before beginning the mercury distillation process. This is begun by putting a liquid nitrogen (LN) cold trap

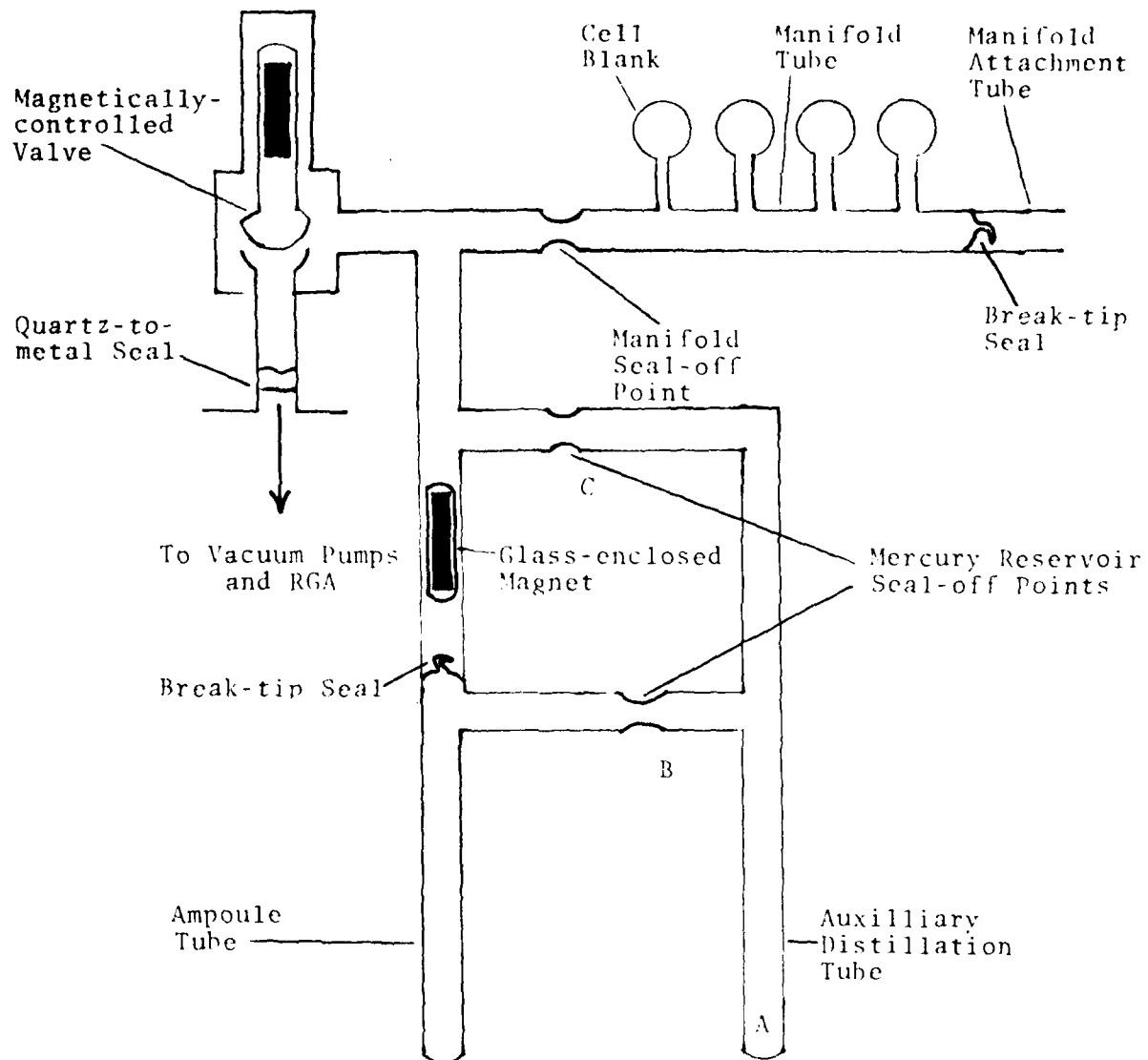


FIGURE 1 - Diagram of Vacuum System

around the auxilliary distillation tube about 2 inches above the droplet. The droplet is then evaporated by gentle heating with a torch and the mercury condenses in a large-area thin film under the trap. The temperature of the cold trap is raised from LN temperature to about -50°C by changing to a dry ice-alcohol slush and is kept at -50°C for about 1 hour while the vacuum system pumps on the thin mercury film. More impurities are removed by allowing the trap to warm up to room temperature for about 1 minute. Then the LN cold trap is placed about 2 inches above the mercury film and the evaporation process is repeated. The process is repeated several times, gradually moving the mercury film up the auxilliary distillation tube. The valve is then closed and the mercury is distilled into the ampoule tube. The distillation is done with electrically controlled heaters, keeping the temperature below 200°C . The mercury is condensed in the ampoule tube in the form of a thin film by using a LN trap. The valve is opened and the purity of the mercury is measured at this point by allowing it to warm up toward room temperature and monitoring the partial pressures of vacuum system gases with a residual gas analyzer (RGA). The mercury is considered to be clean when only the mercury vapor partial pressure rises above the background levels as the film warms up. If the partial pressures of other gases also rise, the mercury needs further cleaning. This is done by maintaining a temperature of -30°C to -40°C on the mercury film and pumping for an extended period of time. After the mercury passes the "clean" test, the mercury reservoir seal-off points B and C are closed, in that order, with a torch. The cleaned mercury is now in a break-tip ampoule, completing the distillation cleaning process.

The ampoule now remains at room temperature while the rest of the system is further cleaned by heating under vacuum. The cell manifold is kept at about 1050°C , and the rest of the fused quartz at 400°C to 500°C , while the metal parts of the system, including the RGA, are baked at lower temperatures. The heat is removed from the metal parts when the system pressure drops to about 10^{-8} torr. The fused

quartz is kept hot until the partial pressures in the system become stable as indicated by the RGA. These concentrations drop significantly during the cooling of the metal parts. The temperature of the cells and the other fused quartz parts is lowered to about 300 °C. At this point the system pressure is about 10^{-9} torr as indicated by the RGA.

The mercury ampoule is opened to the vacuum system by means of a breakable tip and a magnetic plunger. A small burst of gas is usually released and is pumped off quickly. The mercury is then formed into a thin film in the ampoule by evaporation onto a LN-cooled region. The mercury is kept at -30 °C to -40 °C and periodically tested for impurities as described above. When the mercury is considered to be clean, the heat is removed from the cell manifold, the cold bath is removed, the valve is closed, and the mercury is distilled into the manifold using a resistance heater. The valve is then opened for final pumping while the manifold is removed from the vacuum system by means of a torch.

Before individual cells are removed from the manifold, steps are taken to collect all the mercury at the seal-off end of the manifold tube and to ensure that no droplets of mercury remain in any of the cell blanks. This is done by heating all the cell blanks to 200 °C for 3 days while simultaneously maintaining the seal-off end of the main manifold tube at LN temperatures. The entire manifold is then placed for one hour in a chamber at the temperature which will produce the mercury vapor density required in the cells.

For example, an oven temperature of 30 °C will produce a mercury vapor density of about 10^{14} atoms/cm³ as long as liquid mercury is present in the manifold.

The cells, with this density of mercury vapor established in them, are then individually removed from the manifold by heating the narrow neck of each cell with a miniature torch.

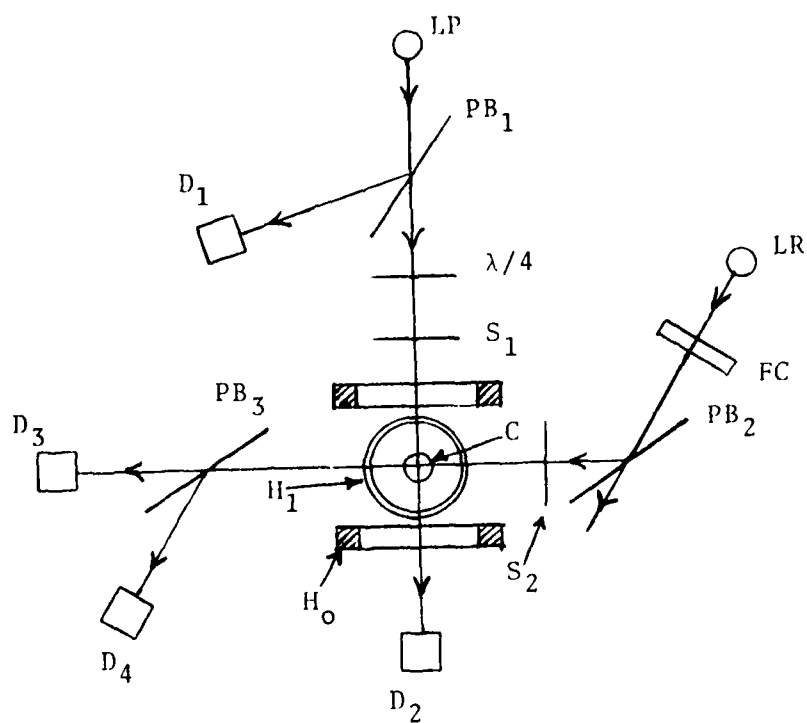
3. CELL TESTING - EXPERIMENTAL METHOD

The cell properties measured in this study include: 1) relaxation times of NMR signals, 2) depth of modulation of the NMR signals, and 3) transmittance of the NMR cell to the pumping radiation. The NMR signals are produced by an interaction between optically oriented ^{199}Hg and ^{201}Hg nuclei in an NMR cell and linearly polarized light emitted by a ^{202}Hg readout lamp (the transverse Faraday effect). A schematic of the apparatus is shown in Figure 2. The basic processes involved are described in detail elsewhere,^{1,2} but will be summarized here.

The optical orientation of the nuclear spins of the mercury atoms in the NMR cell in a longitudinal direction (parallel to the constant H_0 field) is accomplished through selective transitions induced in the atoms by absorption of circularly polarized resonance radiation. The radiation originates in the pump lamp, an electrodeless, rf-excited, ^{204}Hg lamp,³ which emits light at 253.7 nm that is absorbed efficiently by hyperfine components of both ^{199}Hg and ^{201}Hg .² The lamp is dumbbell shaped, with the center section acting as an intense source of unreversed radiation. The light travels along the axis of the H_0 field and is circularly polarized by the combined action of the polarizing beam splitter, PB_1 , and the quarter-wave plate before reaching the cell.

Each polarizing beam splitter consists of a stack of 10 fused silica plates oriented at the Brewster angle. This beamsplitter also reflects part of the light from the pump lamp to detector D_1 . The portion of the pump light that is transmitted by the NMR cell strikes detector D_2 . The ratio of the dc outputs of D_1 and D_2 is used to monitor cell transmittance, which is used as a measure of the mercury vapor density in the cell.

The NMR cell is typically a 1 cm diameter fused silica sphere containing about 10^{14} atoms of ^{199}Hg and ^{201}Hg in the vapor phase. It



C NMR cell
 D photodetector
 FC filter cell
 H_1 dc magnetic field coils
 H_0 ac magnetic field coils
 LP pump lamp
 LR read-out lamp
 PB polarizing beam splitter
 S shutter
 $\lambda/4$ quarter wave plate

The lenses in the system are not shown.

FIGURE 2 - Cell Test Apparatus

is in a constant magnetic field produced by the H_0 coils and an ac magnetic field, produced by the H_1 coils and directed perpendicular to the H_0 field. The H_1 field, oscillating at the Larmor frequency, serves to rotate the longitudinal spin distribution established by the pump lamp into a transverse direction (perpendicular to the H_0 field). The cell temperature can be set at any level from room temperature to 400 °C by a thermally regulated oven.

The readout lamp is physically similar to the pump lamp, but contains the ^{202}Hg isotope. The light emitted by this isotope is slightly off resonance for both ^{199}Hg and ^{201}Hg . This light is linearly polarized by the polarizing beam splitter PB_2 and passes through the NMR cell in a direction perpendicular to the H_0 field. The interaction of the transversely oriented spin distribution with this beam causes a modulation of the plane of polarization of the light at the Larmor frequency. This angular or spatial modulation is converted into a light amplitude modulation by the analyzer PB_3 . The transmitted and reflected beams from PB_3 are detected at D_3 and D_4 , respectively. Since the NMR signals at D_3 and D_4 have a phase difference of 180° , the two individual signals are subtracted to provide the total output signal. The depth of modulation is the ratio of the ac signal to dc output of the readout beam detectors.

The optical frequency distribution of the light emitted by the readout lamp is adjusted by applying a magnetic field of about 0.4 kilogauss to the lamp. The frequencies of the optical components can be shifted to optimum values by adjusting the strength of the magnetic field (Zeeman shift).

The filter, FC, cell contains an isotopically enriched mixture of ^{199}Hg and ^{201}Hg in vapor form. This cell absorbs most of the light in the readout beam that can be absorbed by atoms in the NMR cell and cause relaxation.

Previous measurements¹ have demonstrated that under our normal operating conditions the longitudinal relaxation time, T_1 , is equal to the transverse relaxation time, T_2 . Since we have found the measurement of T_2 to be the more convenient one, all of the NMR relaxation times in this report refer to the transverse component of the magnetization.

Relaxation times can be measured under several light exposure conditions by using the shutters. They are usually measured by establishing a transverse orientation distribution and then simultaneously shutting off both the pump beam and the transverse magnetic field, H_1 . One can also shut off both beams along with the H_1 field and monitor the relaxation process by periodically opening the readout beam shutter. This technique is used for observing extremely long relaxation times, when even the weak relaxation effect of the filtered readout beam would significantly affect the measured relaxation time. This is sometimes referred to as "relaxation in the dark."² Examples of relaxation time measurements made "in the dark" for two cells are plotted vs temperature in Figure 3. A comparison of the characteristics of 2 different types of cell materials can be made from these data since one cell, W101, is made from a high purity fused silica, Suprasil W, and the other cell, P40, is made from a glass, Corning 9741.

During the course of this project approximately 300 cells from a number of materials were made and tested in order to determine the factors that influence the cell characteristics.

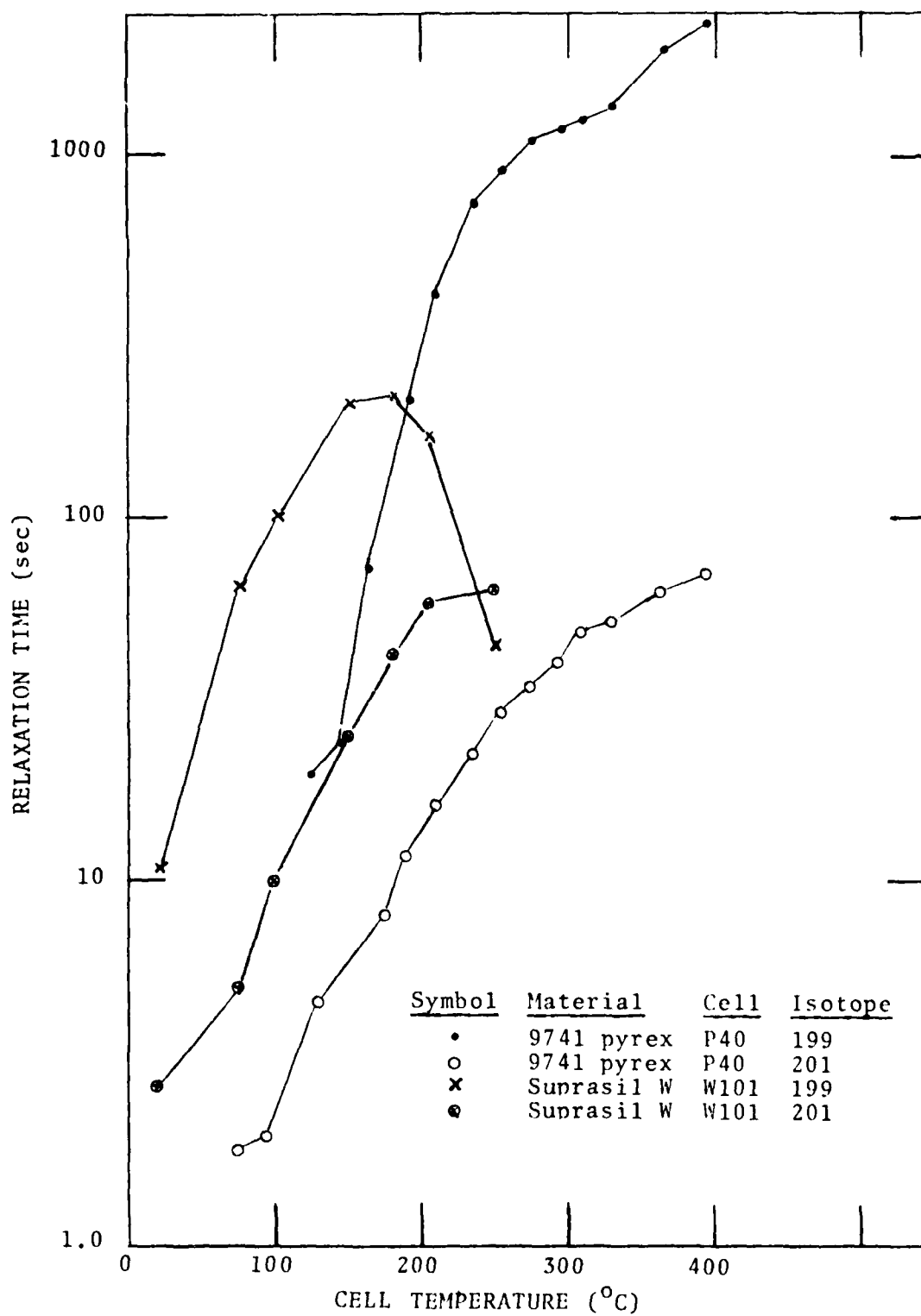


FIGURE 3 - ^{201}Hg and ^{199}Hg Relaxation Times vs Temperature for Two NMR Cells

4. INTERPRETATION OF RELAXATION AND ABSORPTION MEASUREMENTS IN NMR CELLS

Analysis of the large body of observations made on NMR cells during this project has led to certain hypotheses concerning the way in which mercury atoms interact with glass and fused silica surfaces. The general pattern of the dependence of relaxation times as a function of temperature in "stable" NMR cells has been interpreted in terms of an activation energy and the presence of paramagnetic centers in the wall material. By applying the general theory of NMR relaxation to the case of a vapor in contact with a wall, equations have been developed which allow one to determine the activation energy and relative concentration of paramagnetic centers characteristic of a cell wall, based upon relaxation measurements of ^{201}Hg and ^{199}Hg in the cell. Well-defined exceptions to this general pattern have also been observed and interpreted.

Several complementary studies were made in order to elucidate some of the NMR relaxation measurements and to distinguish between alternative competing models. These complementary studies included measurement of mercury vapor density in NMR cells and in contact with large-surface-area forms of SiO_2 . Analysis of mercury vapor measurements has led to a hypothesis involving the interaction between excited mercury atoms and fused silica surfaces. All of the experiments involving NMR cells are included in this section and the rest are covered in Section 5.

Since much of the subsequent discussion depends upon the models used for the cell walls and the collision processes, the first part of this section is devoted to a detailed picture of the possible physical characteristics of the cell wall and of the possible atom-wall interactions as developed through a review of the pertinent literature.

This is followed by a presentation of the general theory of relaxation as it applies to this physical model. The NMR relaxation measurements

are interpreted in terms of this theory. Activation energies and relative concentrations of paramagnetic centers (PMC) are calculated.

Concluding this section are an interpretation of resonant light transmittance measurements and a comparison of several cell wall materials.

4.1 REVIEW OF MERCURY-WALL INTERACTION

When a mercury atom reaches a wall, it may interact with the wall in one of several ways:

- 1) Physisorption - A mercury atom can form a weak van der Waals bond at certain wall sites. Such a bond is reversible and short-lived at normal cell operating temperatures and has an activation energy of between 0.1 and 1.0 volt. During its sojourn on the wall, the mercury atom may also diffuse on the surface.
- 2) Chemisorption - A mercury atom can form a chemical bond with a surface atom. This reaction might involve the breaking of chemical bonds between surface atoms, or a dangling bond might have been present. Chemisorption activation energies are typically from 1.0 to 10.0 eV, but can be higher for very stable surface-adsorbent states.
- 3) Chemisorption of Excited Mercury Atoms - During the process of optical pumping, a mercury atom is transformed briefly from the stable 1S_0 ground state to a reactive 3P_1 excited state with an additional energy of 4.9 eV. When an excited atom hits the wall, chemisorption of this atom is more likely to occur than is chemisorption of ground-state atoms.

- 4) Diffusion - It is possible for mercury, as metallic ions, to diffuse from surface sites into the interior of the wall. For example, diffusion of alkali ions in fused silica is characterized by an activation energy, E_a , of 1.0 to 1.4 eV. The E_a values are unrelated to ion size and are constant below certain characteristic temperatures ($\sim 300^\circ\text{C}$), but decrease at higher temperatures⁴.

While the observations presented later in this section indicate that the predominant processes in the NMR cells are physisorption of ground-state mercury atoms and chemisorption of excited-state mercury atoms, it is possible that the other processes are also occurring, although at a very slow rate.

4.2 SILICA SURFACE MODEL

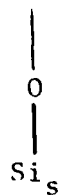
Although the silica surface probably consists of a random network of pure fused silica molecules, the possibilities of surface crystallization and surface impurities are also considered in this section.

A commonly used model for the bulk structure of fused silica is a three dimensional random network model in which each silicon atom is connected to four oxygen atoms in a tetrahedron. The oxygen atoms act either as bridging (bonded to two silicon atoms) or non-bridging (bonded to only one silicon). The tetrahedra are arranged primarily in five-, six-, and seven-membered rings, according to S.V. King⁵. The surface of this structure would be a partially random array of silicon and oxygen atoms in a variety of configurations and bonding states.

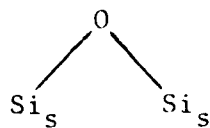
Possible surface terminations of pure fused silica include^{6,7} (see Figure 4) are:

- (1) A non-bridging oxygen — an oxygen attached to one silicon atom. Since this atom has a dangling bond, it may react with any vapors present, strain the surface structure while

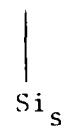
non-bridging
oxygen



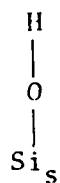
bridging
oxygen



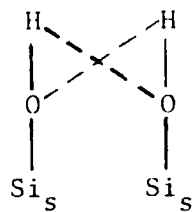
three-
coordinated
silicon



surface
silanol



hydrogen-
bonded
surface
silanols



$\text{Si}_s \equiv$ surface silicon atom

FIGURE 4 - Surface States of Fused Silica

attempting to form a bond with its unpaired electron, or participate in crystallization until annihilated.

- (2) A bridging oxygen — an oxygen atom which is attached to two silicon atoms, forming a very stable structure.
- (3) A stretched bridging oxygen— an oxygen atom connecting two silicon atoms which are farther apart than usual. A weakened bond with a locally stressed underlying solid is formed.
- (4) A "freely vibrating" OH group — also called a silanol.
- (5) A hydrogen-bonded pair of OH groups — this bonding requires the OH groups to be situated near each other. These structures form adsorption sites for water.
- (6) A three-coordinated silicon — it has a dangling bond, which can attack other bonds by ionic attraction and can couple to a non-bridging oxygen.

While the silica surface is generally considered to be a random structure, it is also quite probable for some quartz crystal growth to occur on the surface. This structure consists of a regular array of six-membered rings⁵ for all low-pressure SiO_2 crystalline phases. A study of the rate of crystallization of fused silica by Fratello et.al.⁶ produced the following conclusions:

1. Crystallization occurs by bond rearrangements at the amorphous-crystalline interface.
2. The linear dependence of crystallization rate on hydroxyl and chlorine content results from the direct participation of these species in the crystallization process. The somewhat lower constant of proportionality for chlorine may be due to its lower mobility.

3. The activation energy results mainly from the formation of an active defect by breaking a strained bond. The simultaneous bond formation and breaking is a relatively low-energy process.
4. Oxidizing the sample leads to higher rates of crystallization by turning annihilation sites (three-coordinated silicons) into active defects (non-bridging oxygens).
5. Since broken bonds are the active defects, sources of non-equilibrium concentrations of broken bonds such as fresh fracture surface or a dislocation will locally enhance rearrangement rates.
6. The synthetic silicas contain significantly smaller concentrations of bond weakening impurities, resulting in a lower pre-exponential factor in the crystallization rate.

In this model, the main mechanism for crystallization in fused silica is thought to be a non-bridging oxygen acting with a highly mobile hydroxyl group in a rapid, low-energy rearrangement process involving simultaneous bond formation and breaking. Each step of the process results in displacement of a dangling half-bond to another atomic site and leads to rearrangement of the amorphous ring structure to the six-membered rings of the crystalline state. The dangling half-bonds propagate until they are annihilated by recombination with another half-bond.

The material that Fratello⁸ found to have the lowest crystallization rate is a form of Suprasil, the material that has produced our best NMR cells. The exact connection is not known at this time, but these data indicate certain possibilities: (1) crystalline surface areas are strong relaxation sites, (2) the disruption of the surface during the process of crystallization produces strong relaxation

sites, and (3) one or more of the impurities that promotes crystallization also forms or promotes the formation of strong relaxation sites.

These data are also a further indication that the performance of the best NMR cells is determined by the intrinsic material impurities rather than by surface contamination and therefore that the mercury is interacting directly with the fused silica surface.

During the vacuum system processing of the NMR cells, they are heated to 1000 °C. The data of M.L. Hair⁷ indicates that heating fused silica above 800 °C eliminates the hydrogen-bonded OH groups, causing them to change irreversibly into a bridging oxygen and a liberated water molecule.

The heating of the quartz also increases the rate of the above-mentioned crystallization process through two mechanisms: (1) the process rate is exponential with inverse temperature⁸ and (2) heating and cooling the quartz through phase transition regions can increase the number of active defects by creating broken bonds.

Impurities, if present, can significantly affect the characteristics of a fused silica surface. Impurities can enter a NMR cell in a number of ways:

- 1) Gases can diffuse into the cell.
- 2) Impurities contained in the original cell wall material can migrate to the interior.
- 3) Contamination can enter during cell fabrication or filling.

As mentioned above, cells are heated to about 1000 °C during vacuum system processing and also after being removed from the manifold. As the temperature increases, the permeation of gas into and through a quartz wall increases exponentially.^{9,10} If the outer cell surface

is exposed to the atmosphere during heating, hydrogen, helium, and neon diffuse into the wall, with hydrogen being the most abundant gas, according to the data of Norton.⁹ The interstitial protons can bond to oxygen ions to form OH molecules.¹¹

Even the purest fused silica contains traces of metallic impurities and chlorine. Table 1 lists the major metallic impurities of Suprasil W. This list was taken from a larger list provided by Amersil Inc. on page 4 of its brochure entitled "Optical Fused Quartz and Fused Silica." It also contains about 90 ppm of chlorine.⁸

TABLE 1 - Metallic Impurities in Suprasil W

<u>Element (weight)</u>	<u>PPM by Weight Suprasil W</u>
Al (26)	.1
Ca (40)	.1
Fe (56)	.2
Mg (24)	0-.1
P (31)	0-.1
Na (23)	.04
Ti (48)	0-.1

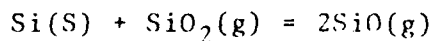
The most abundant metallic impurity in all fused silicas is aluminum.¹¹ It exists in quartz in the 3+ valence state, substituting for silicon (4+) and requiring an additional 1+ ion to compensate for the missing charge. This can occur in several ways: (1) the aluminum ion can trap an interstitial proton which bonds to an oxygen, forming an adjacent OH⁻ molecule, (2) the aluminum can trap a hole at an adjacent oxygen ion, leaving an unpaired electron and thus a paramagnetic defect, or (3) it can trap a positive alkali ion, forming centers which cause local lattice deformation, but which are not paramagnetic. Observations made on high-quality quartz crystals by Brown and Kahan¹² indicated that all substitutional aluminum ions are initially alkali-compensated. If dissociation of

an aluminum-alkali center occurs, the aluminum can trap a hole or an interstitial hydrogen ion.¹¹ In quartz crystals, heating the material above 600 K destroys the aluminum-hole centers and the aluminum-hydroxyl centers and restores the aluminum alkali centers.

It is possible for the silica to be contaminated during the fabrication or filling processes. Such contamination would drastically alter the wall properties. The variation in performance that has been observed between cells that were processed with presumably identical procedures may have been due to low levels of contamination. However, direct evidence of contamination has not been observed. The surface analysis tests, which will be described in detail in another section, have shown no evidence of crystalline structure or contamination on interior cell surfaces; only a smooth fused silica surface was observed.

To produce and maintain atomically clean surfaces requires vacuum system pressures less than 10^{-10} torr. This is not the case in the vacuum system used for cell processing, even with the mercury sealed off from the system in its break-tip ampoule. After the mercury ampoule is opened, the system pressure greatly increases due to the mercury vapor pressure and those of the gases it invariably contains. Thus the fused silica surface can be expected to have all adsorption sites filled. The experimental evidence, which will be presented in a later section, indicates that these sites occupy only a small fraction of the total surface area.

During the seal-off process of the cell from the manifold, or during subsequent flaming of cell tips, it is possible that some sublimation of SiO_2 occurs. If SiO_2 sublimation does occur the following reaction can exist¹³



The SiO can then produce Si and SiO₂ deposits by sublimation on neighboring surfaces. This raises the possibility that regions consisting of a mixture of Si and SiO₂ exist inside NMR cells.

4.3 VAPORS IN THE CELLS

Total residual gas pressure in the vacuum system is reduced to 10⁻⁹ torr before the mercury is driven into the cell manifold. Although the mercury has been carefully purified, it still contains some gases, chiefly helium and argon. Gases are also generated during the sealing-off operations of the manifold from the vacuum system and of the individual cells from the manifold. These gases are likely to be primarily water and carbon dioxide. The quantities generated depend upon the history of the silica and on the amount of heating done during the seal-off operation. Much of the gas generated during the removal of the manifold from the vacuum system will be gettered by the mercury droplets in the manifold.

The vapor pressure of mercury in a resonance cell is usually about 10⁻³ torr. The other gases present at the time of cell seal-off probably have pressures of about 10⁻⁷ torr.

Additional vapors can be introduced into the cell if the cell is heated in air. As indicated earlier, the helium and hydrogen components of the atmosphere can diffuse through the quartz wall into the interior quite readily.

In summary, a NMR cell, consisting primarily of mercury vapor enclosed in a fused silica envelope, may have its NMR characteristics affected by a number of factors:

- 1) degree and type of surface crystallinity,
- 2) types and densities of electronic and chemical surface states,

- 3) impurities on the fused silica surface which may have been in the original material, introduced during fabrication, or diffused into the material during processing, and
- 4) gaseous impurities.

4.4 INTERPRETATION OF RELAXATION MEASUREMENTS

Relaxation measurements on ^{201}Hg and ^{199}Hg in NMR cells made from various materials can be interpreted in terms of activation energy, concentration of paramagnetic centers, and stability of surface characteristics.

The theory of nuclear magnetic resonance relaxation phenomena is reviewed and developed in a unified way in Abragam.¹⁴ The general theory in Abragam has been applied to describe the relaxation of an optically oriented vapor in contact with a solid.^{2,15,16,17}

A brief review of the theory is given. The model for relaxation assumes that the mercury vapor is of low density, $\sim 10^{11}$ to 10^{12} atoms/cm³; the mean free path is large compared to the dimensions of the cell; and the cell is optically thin. Under these conditions the nuclei will experience relaxing interactions only during collisions with the walls.

An atom on colliding with the wall is adsorbed for an average time τ_a . During the time on the wall, the atom may diffuse on the surface between several sites, the average time between jumps in the diffusion process being τ_d . Both the diffusion and sticking processes are thought to be described by potential barriers with well defined activation energies. The temperature dependence of the average sticking and diffusion times is given by

$$\tau_a = \tau_{a0} \exp(E_a/RT), \quad (1)$$

and

$$\tau_d = \tau_{do} \exp(E_d/RT), \quad (2)$$

where τ_{ao} and τ_{do} are the high temperature limits, E_a and E_d are the molar activation energies for adsorption and diffusion, respectively, R is the molar gas constant, and T is the temperature in kelvins.¹⁵

An estimate of the magnitude of τ_a can be made for the mercury atoms at room temperature using equation (1). If an atom loses one degree of freedom of translation, $\tau_{ao} = h/kT = 1.6 \times 10^{-13}$ sec at room temperature.¹⁸ Using this value and assuming that $E_a = .25$ eV, $T = 300$ K, one gets $\tau_a = 2 \times 10^{-9}$ sec. For $T = 400$ K, one gets $\tau_a = 2 \times 10^{-10}$ sec. The value of E_a used here is derived from experimental results which follow in this section.

The interval between collisions is equal to the mean time of flight of an atom traversing the cell. The equation for this in a spherical cell is¹⁹

$$\tau_v = \frac{5}{2}r (2m/\pi kT)^{1/2}, \quad (3a)$$

$$= AT^{-1/2} \quad (3b)$$

where

m = molecular weight,
 k = Boltzman's constant, and
 r = cell radius.

For a cell with a 1 cm diameter at room temperature,

$$\tau_v \sim 5 \times 10^{-5} \text{ sec.} \quad (4)$$

During the wall collision, the nucleus of the atom is subjected to a randomly fluctuating interaction that can induce transitions at the resonance frequency. For a highly mobile atom, $\tau_a \gg \tau_c$, the relaxation rate (the inverse of the relaxation time) is¹⁶

$$\tau^{-1} = \langle \mathcal{H}_1^2 \rangle \frac{\tau_c}{1 + \omega_0^2 \tau_c^2} P_1 \frac{\tau_a}{\tau_a + \tau_v} \quad (5)$$

where $\langle \mathcal{H}_1^2 \rangle$ is the mean square average of the random Hamiltonian, P_1 is the probability of the atom striking the surface at the site of the source for \mathcal{H}_1 , ω_0 is the resonance frequency, and τ_c is the correlation time for the randomly fluctuating fields. The correlation function for the random Hamiltonian is assumed to be a stationary random function of time, with correlation time τ_c which is of the order of τ_d^{16} . For the temperatures used in relaxation measurements in this report, $\tau_a < 2 \times 10^{-9}$ sec, so that the second denominator above, $\tau_a + \tau_v$, can be approximated by τ_v .

In all of the experiments reported here, the magnetic field is ~1.3 gauss, the frequencies of ^{199}Hg and ^{201}Hg are 1 kHz and 369 Hz, respectively, and τ_c is less than 10^{-8} sec. Therefore the condition for extreme narrowing is fulfilled, i.e., $\omega_0 \tau_c \ll 1$, and one can simplify the first denominator in equation 5. Using these simplifications, and substituting from equations (1) and (2),

$$\begin{aligned} \tau^{-1} &= \langle \mathcal{H}_1^2 \rangle P_1 \frac{\tau_a \tau_c}{\tau_v} \\ &= \langle \mathcal{H}_1^2 \rangle \frac{P_1 \tau_a \tau_d \exp(E_a + E_d)/RT}{\Delta T^{-1/2}} \end{aligned}$$

Mercury isotope ^{199}Hg , which has a nuclear spin $I = \frac{1}{2}$, possesses only a nuclear magnetic dipole moment. The perturbing Hamiltonian will be that of a magnetic interaction. Relaxation can occur only when the nucleus encounters a binding site which is in the vicinity of a magnetic moment, such as that of a paramagnetic center (PMC).

The mean square value of the Hamiltonian is¹⁷

$$\langle H_1^2 \rangle = 2\gamma_{199}^2 \langle h_0^2 \rangle, \quad (7)$$

where $\langle h_0^2 \rangle$ is the mean square amplitude of the fluctuating field along a particular coordinate, and γ_{199} is the gyromagnetic ratio for ^{199}Hg . It is assumed that the perturbing field is isotropic; the amplitudes of the field along all three coordinate axes are equal.

Similarly, the magnetic interaction Hamiltonian for ^{201}Hg is

$$\langle H_1^2 \rangle = 2\gamma_{201}^2 \langle h_0^2 \rangle, \quad (8)$$

where γ_{201} is the gyromagnetic ratio for ^{201}Hg . The magnetic interaction is about seven times stronger for ^{199}Hg than it is for ^{201}Hg . Therefore, if no other relaxing mechanisms are present, the relaxation rate of ^{199}Hg will be seven times greater than that of ^{201}Hg under identical conditions.

Mercury ^{201}Hg has a nuclear spin $I = 3/2$ and possesses a nuclear electric quadrupole moment in addition to a magnetic dipole moment. This provides an additional mechanism for the relaxation of ^{201}Hg . The energy of the nuclear electric quadrupole moment is proportional to the electric field gradient at the nucleus. The electric field gradient can arise from an electric charge distribution on the surface and/or a distortion of the spherically symmetric electron shells of the atom when it binds to the surface.

An expression for the Hamiltonian for a quadrupole interaction was obtained by C. Cohen-Tannoudji²⁰. In his derivation he shows the quadrupole interaction to be

$$\mathcal{H}_{1q} = \frac{eqQ_0}{1(2I-1)} \sqrt{\frac{\pi}{5}} \sum_{r=-2}^{r=2} A_2^r Y_2^{-r}(\theta, \phi). \quad (9)$$

The A^r are constructed from spin operators, and the Y_2^r are the spherical harmonics. The variables θ, ϕ describe the angle of the electric field gradients. The electric field gradients are assumed to be cylindrically symmetric, and

$$q \equiv \frac{\partial^2 V}{\partial z_1^2},$$

where z_1 is a coordinate along the axis of symmetry. In his derivation Cohen-Tannoudji assumed all angles of θ and ϕ are equally probable and averaged the product $A_2^r Y_2^{-r}$ over all angles. This yields the result that the mean square amplitude of the Hamiltonian has the form

$$\langle \mathcal{H}_{1q}^2 \rangle = \frac{8\pi}{5} \frac{e^2 Q_0^2}{h^2} q^2. \quad (10)$$

Quadrupolar perturbations which can shift the energy levels of the ^{201}Hg , causing a splitting of the ^{201}Hg resonance will not be considered in this section, but will be discussed in detail in a later section, where an important exception to the above theory is developed.

In summary, for ^{199}Hg , in spherical cells,

$$\tau_{199}^{-1} = \gamma_{199}^2 \langle h_0 \rangle^2 P_1 A^{-1} T^{\frac{1}{2}} \tau_0 \exp E_s/RT, \quad (11)$$

where

$$E_s = E_a + E_d,$$

$$\tau_0 = \tau_{ao} \tau_{do},$$

$$A = \frac{3}{2} r (2m/\pi k)^{\frac{1}{2}},$$

and for ^{201}Hg ,

$$\tau_{201}^{-1} = \tau_{201d}^{-1} + \tau_{201q}^{-1} \quad (12a)$$

$$= \left[\gamma_{201}^2 \langle h_o^2 \rangle P_1 + \frac{e^2 Q_o^2}{h^2} \langle q^2 \rangle P_2 \right] A^{-1} T^{\frac{1}{2}} \tau_o \exp E_s / RT \quad (12b)$$

$$= \frac{1}{7} \tau_{199}^{-1} + \frac{e^2 Q_o^2}{h^2} \langle q^2 \rangle P_2 A^{-1} T^{\frac{1}{2}} \tau_o \exp E_s / RT, \quad (12c)$$

where τ_{201d}^{-1} refers to the dipole contribution to the ^{201}Hg relaxation rate, τ_{201q}^{-1} is the quadrupole contribution to the ^{201}Hg relaxation rate, and P_2 is the probability of the atom striking the surface at a source of q . According to Putyrskii,²¹ the most probable value for E_d is $1/6 E_a$, therefore, one might use $.83 E_s$ as a likely value for E_a . From the above equation one finds that

$$\tau_{201q}^{-1} = \tau_{201}^{-1} - \frac{1}{7} \tau_{199}^{-1} \quad (13a)$$

$$= \frac{e^2 Q_o^2}{h^2} \langle q^2 \rangle P_2 A^{-1} T^{\frac{1}{2}} \tau_o \exp E_s / RT \quad (13b)$$

If τ_{199}^{-1} and τ_{201}^{-1} are measured in an NMR cell under identical conditions, one can determine τ_{201q}^{-1} as shown by equation (13a).

In a cell in which the magnitude and direction of the electric field gradients on the inner surface are stable, one can determine E_s by measuring the slope of a semi-logarithmic plot of $\tau_{201q}^{-1} T^{\frac{1}{2}}$ against T^{-1} . This is commonly known as an Arrhenius plot.

Figure 5 contains E_s plots for 4 cells. Two of the cells are made of Suprasil W, a high purity, low-OH synthetic fused silica made by Amersil Inc. One cell is made from Suprasil, a high purity, OH-containing synthetic fused silica from the same company. The fourth

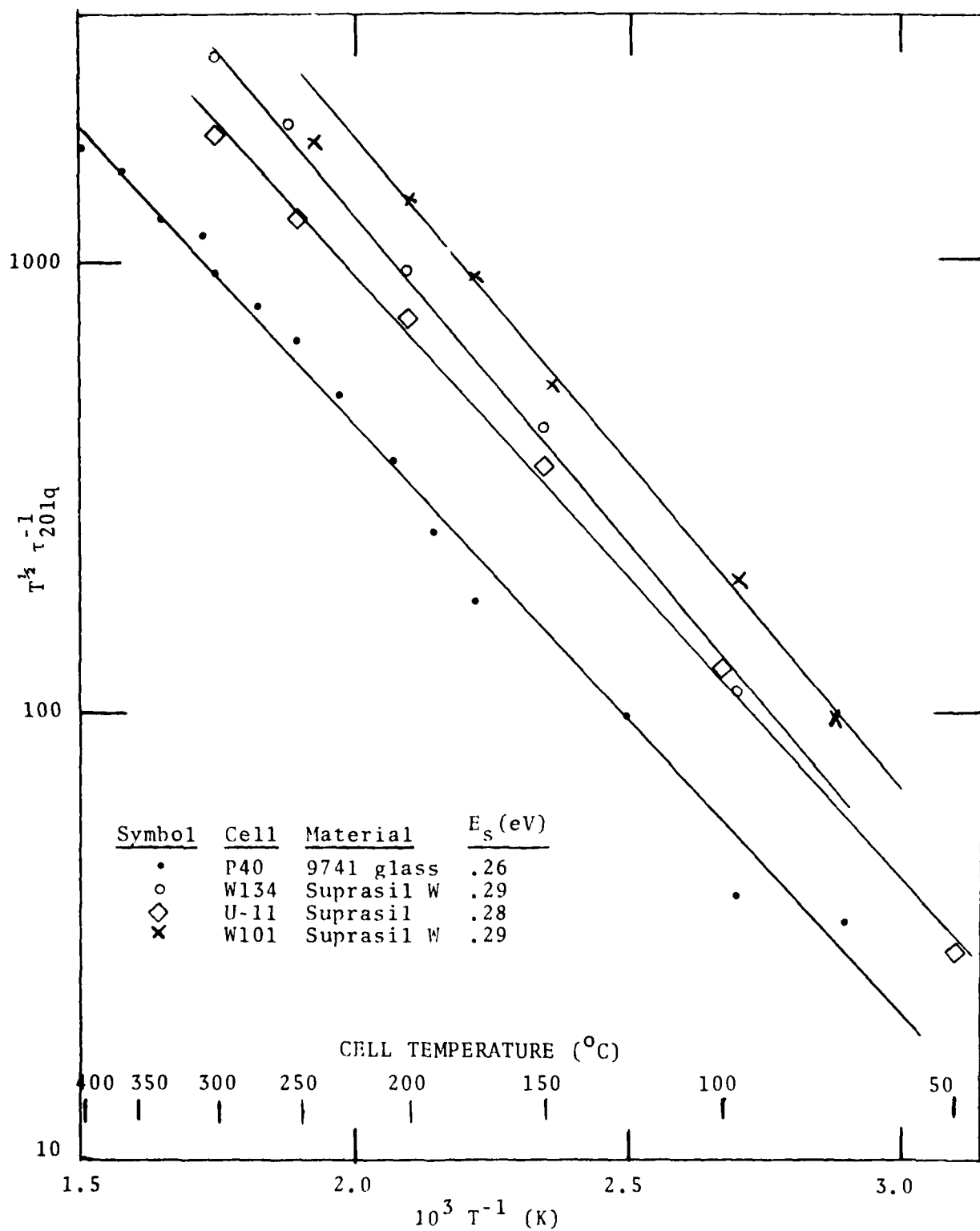


FIGURE 5 - Activation Energy Plots for Several Materials

cell is made from Corning 9741, an ultraviolet-transmitting glass. It can be seen from the figure that E_s is nearly the same for the three materials, ranging from .26 to .29 eV. This corresponds to a range of .22 to .24 eV for the activation energy E_a . These values of E_a indicate that physisorption involving van der Waals forces of about the same strength is occurring on all three materials.

These observations show that E_s and $\langle q \rangle^2 P_2$ are constant over the approximate temperature range 50 °C - 300 °C for these materials. One can use this information to calculate the temperature dependence of the product $\langle h_o \rangle^2 P_1$ in the expression for τ_{199}^{-1} . If one divides equation (11) by equation (13b), one gets

$$\tau_{199}^{-1} \tau_{201q} = \frac{h^2 \gamma_{199}^2 \langle h_o \rangle^2 P_1}{e^2 Q_o^2 \langle q \rangle^2 P_2} \quad (14)$$

Under these conditions, any variation with temperature of the expression on the left of equation (14) can be assumed to be due to a temperature dependence of the product $\langle h_o \rangle^2 P_1$. This product is a measure of the PMC concentration and strength on the surface of the wall. A semi-logarithmic plot of $\tau_{199}^{-1} \tau_{201q}$ data vs temperature for the four above-mentioned cells W-101, W-134, U-11, and P-40 is shown in Figure 6.

The semi-logarithmic format is used primarily to accommodate the large percentage changes in the data, rather than as an analytical tool. This plot indicates that the product of concentration and strength of the PMC's tends to increase with temperature for the silica materials, but decreases for the glass over the same temperature region.

These cells are considered stable; the values of relaxation time as a function of temperature are reproducible from one test cycle

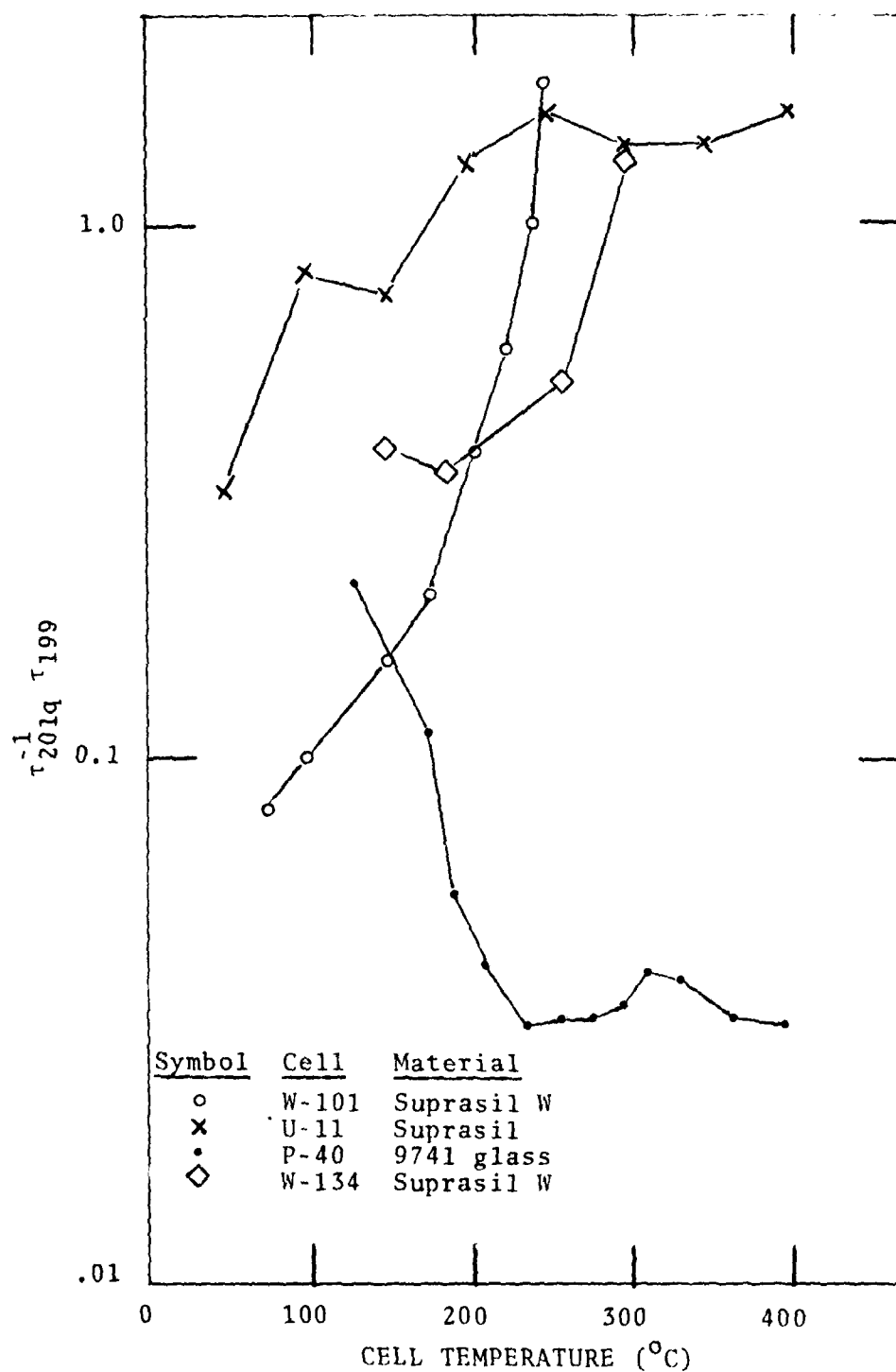


FIGURE 6 - Paramagnetic Center Concentration vs Temperature for Several Materials

to the next. The constancy of the measured E_s values is also an indication of wall stability.

This method of analyzing the relaxation time data was used to study the evolution of NMR cells from their first temperature cycle until stable performance was achieved. As an example, the data indicating the evolution of the above-mentioned cell W-134 is shown in the semi-logarithmic plots, Figures 7 and 8. The history of heat treatments received by this cell is given in Table 2.

TABLE 2 - Heat Treatments Received by Cell W-134

<u>Date</u>	<u>Temperature ($^{\circ}\text{C}$)</u>	<u>Duration (min)</u>
2/6/81	850	15
3/3/81	850	15
3/4/81	850	15
3/11/81	950	15
3/12/81	950	5
4/9/81	950	15
4/22/81	950	15
4/27/81	950	5
5/5/81	950	5

The data indicate that this cell in its early stages had a strongly relaxing surface with highly variable characteristics. The relaxation times were observed to vary as a function of temperature, pump-lamp intensity, and time.

At the end of the series of treatments, certain characteristics were evident:

- 1) The electric quadrupole interaction had diminished, probably due to a decrease in the density of relaxation sites.

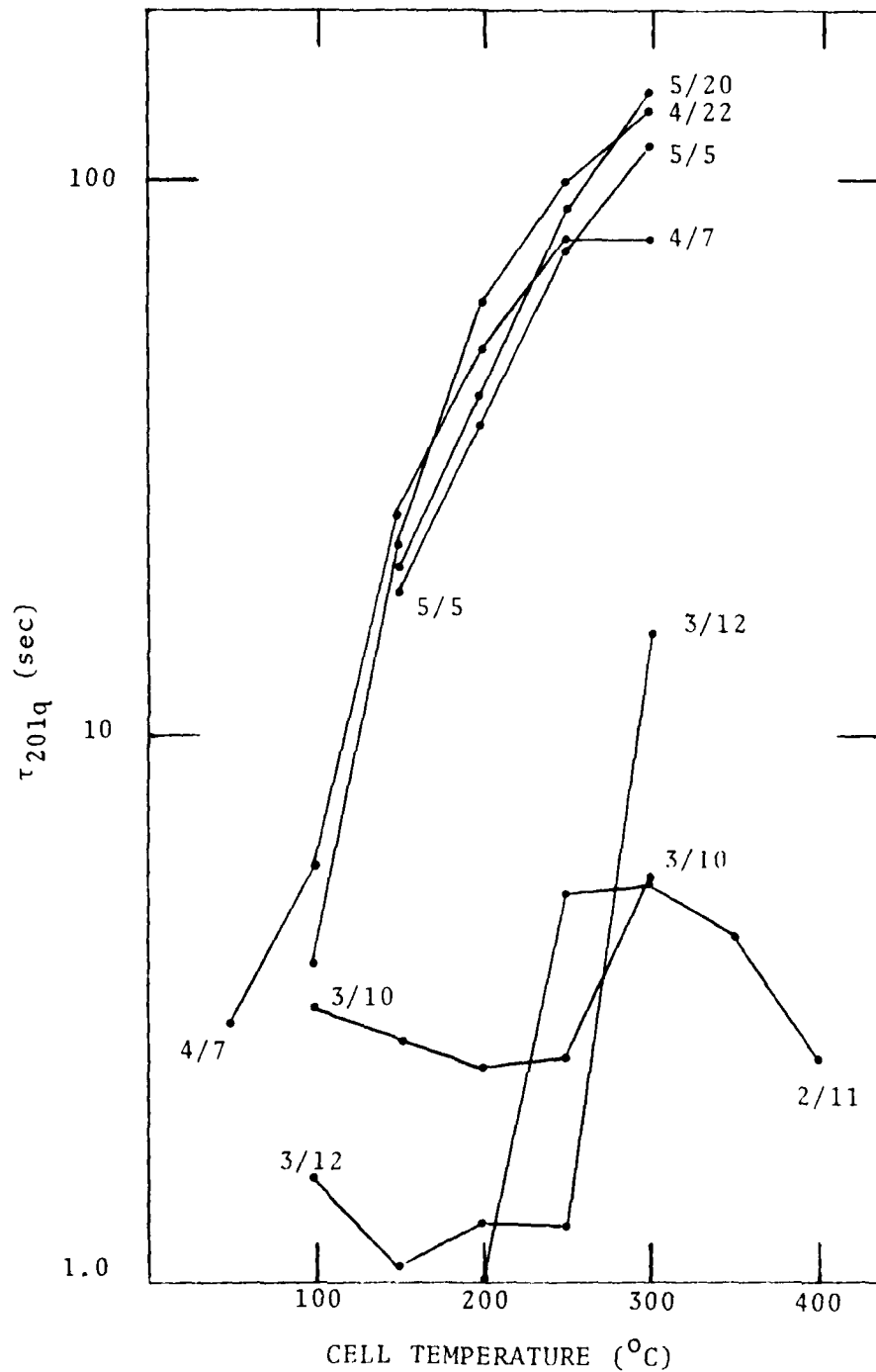


FIGURE 7 - Effects of Heat Treatments on τ_{201q} of Cell W-134

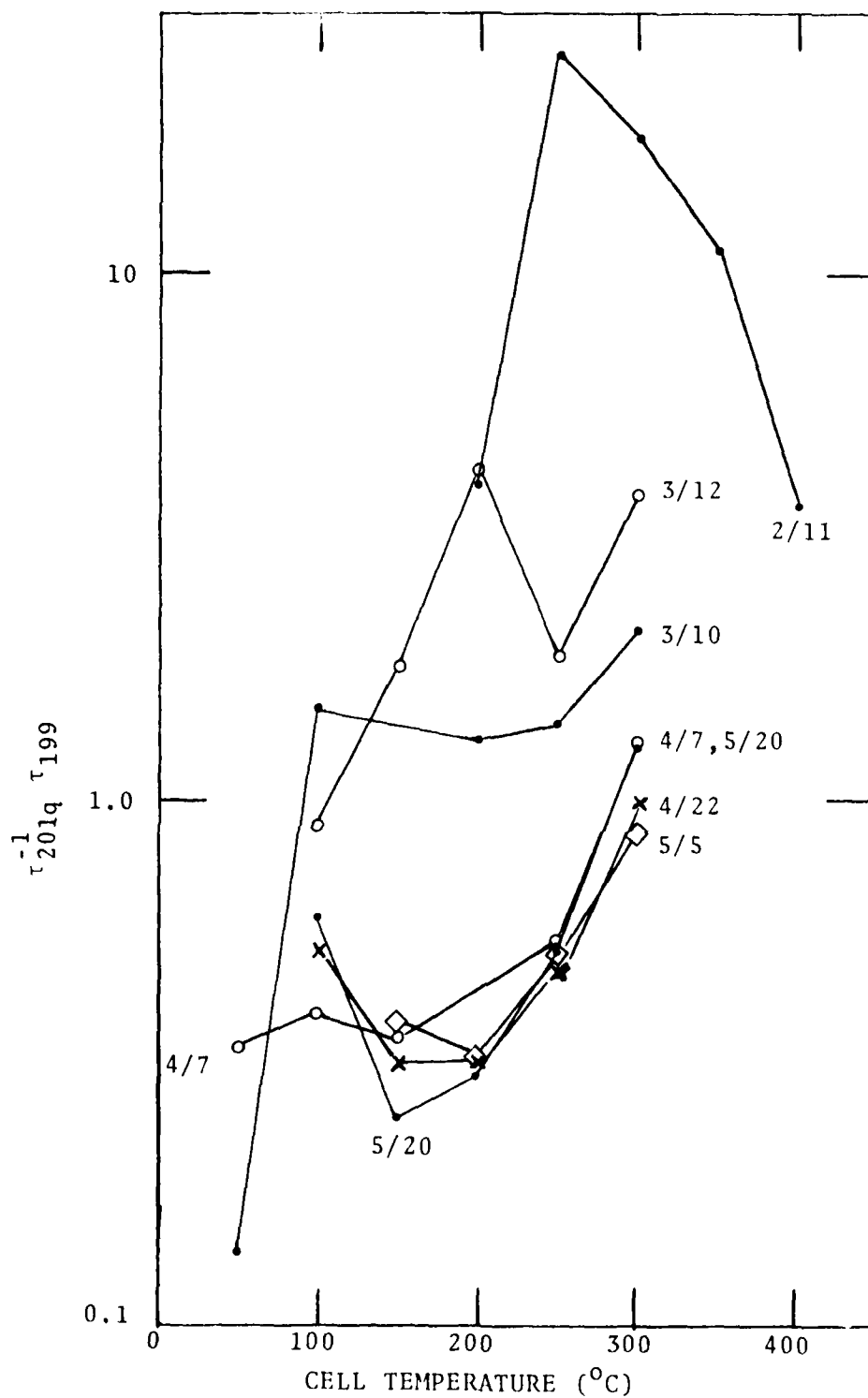


FIGURE 8 - Effects of Heat Treatments on PMC Concentration of Cell W-134

- 2) The activation energy became constant at .24 eV over the 100 °C to 300 °C region (see Figure 5).
- 3) The concentration of PMC diminished and became a reproducible function of temperature (see Figure 8). The concentration stayed constant below 200 °C, but started increasing at 250 °C.
- 4) The mercury vapor density became a reproducible function of temperature.

Since the cells were baked at 1000 °C for an extended period of time while attached to the vacuum system, the 900 °C heatings of the sealed-off cells might seem superfluous. Several possible reasons exist that might necessitate the additional heat treatments: (1) the act of sealing off the cell might introduce contaminants that have to be neutralized or gettered, (2) the act of sealing off might have caused the cell to receive a fresh interior coating of SiO₂ that now has to be "cured", e.g. some hydrogen bonded silanols might require removal, (3) some contaminants may have been introduced along with the mercury vapor, or (4) a high temperature treatment in the presence of mercury vapor may be required to effect the necessary changes in the surface.

It is likely that several processes are occurring simultaneously in a cell as it evolves from an unstable cell to a stable cell through a series of heat treatments and tests. Since cells that receive a large number of heat treatments eventually start to degrade with additional treatments, it appears as if some of the processes that occur are beneficial, while others are deleterious to the cell performance. Possible processes include surface crystallization, change of state of crystalline surface areas, changes in surface chemical states, and chemical reactions between mercury and impurities. More specific information about the state of the wall surface is needed in order to understand the cell evolution process.

ESCA, a surface analysis technique which has the potential for providing this information, was performed on several cells, and will be discussed in Section 5.

Although most cells that are stable exhibit a τ_{201q}^{-1} temperature dependence that can be characterized by an E_s of .28 eV, there were exceptions. One such case is shown by the E_s plot for cell W-111 in Figure 9. This curve apparently has two different, distinct slopes, each characteristic of a temperature region. There are several possible interpretations of this data:

- (1) Model A - The surface is stable and contains two types of sticking sites, each one characterized by an activation energy. The one with the higher activation energy dominates at lower temperature, and the other dominates at higher temperatures. An attempt to fit the curve of Figure 9 using the model

$$\tau_{201q}^{-1} T^{-1/2} = A_e^{E_1/RT} + B_e^{E_2/RT} \quad (15)$$

yields

$$E_1 \sim .1 \text{ eV}, \quad E_2 \sim .5 \text{ eV},$$

$$A/B \sim 7 \times 10^4.$$

One would expect one of the above E_s values to be close to the .28 eV value which is characteristic of stable cells of this material and others. Since the values found with this model are both substantially different from the characteristic .28 eV, the model itself must be questioned.

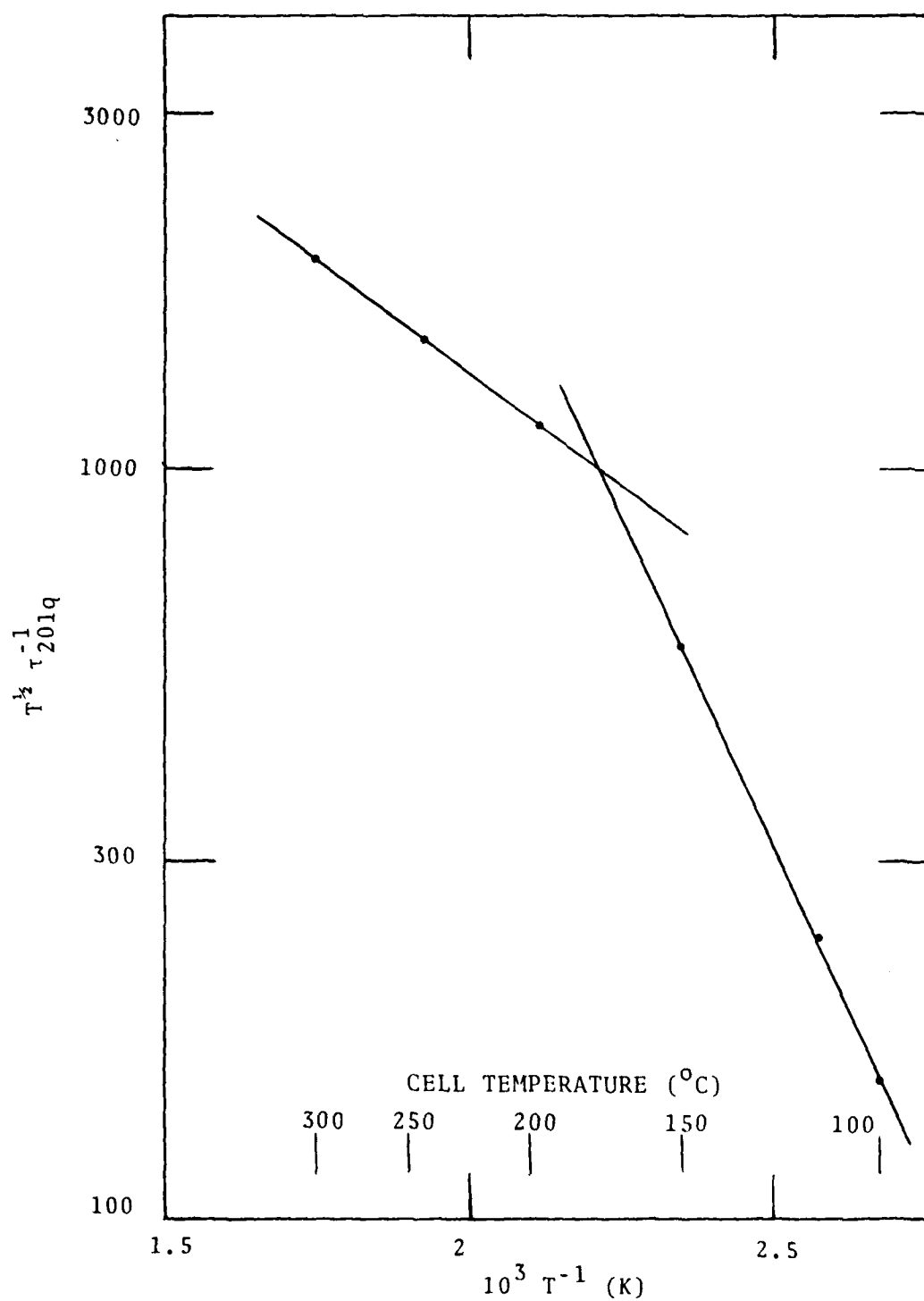


FIGURE 9 - Activation Energy Plot for Cell W-111

- (2) Model B - At a certain temperature, a phase change occurs in the micro-crystalline areas of the surface, or in the entire surface, so that the surface is now characterized by a different activation energy. This model leads to a low temperature E_s of .35 eV and a high temperature E_s of .12 eV for this data, with a change of state occurring at about 200°C. A change of .23 eV in E_s at 200 °C produces a change of a factor of

$$e^{E_s/RT} = e^{\frac{.23}{473 \times 8.62 \times 10^{-5}}} \quad (16a)$$

$$= e^{5.64} \quad (16b)$$

$$\approx 280 \quad (16c)$$

In the equation

$$\tau_{201q}^{-1} T^{-1/2} = \tau_o e^{E_s/RT} \quad (17)$$

If a change of state produces this type of change in E_s , it seems that a large change in τ_{201} should occur, unless a compensating change in τ_o occurs. An uncompensated change in τ_{201q} would appear as a discontinuity of the curve in Figure 8. No such irregularity appears in Figure 8.

- (3) Model C - E_s is constant, but another surface factor which affects τ_{201q} is changing with temperature. A relaxation mechanism, which may come into existence or be increased due to a change of state of micro-crystalline quartz areas and which increases logarithmically with temperature, will cause an apparent change in E_s . It can be seen from the PMC data of Figure 6 that surface changes occur as a function

of temperature, even in "stable" cells.

The nearly identical values of E_s for different types of quartz and glass suggests that van der Waals' forces of a similar type are acting in all cases, and that a sudden, large change in the strength of this force due to a "change of state" for a given material is unlikely. For the above reasons, hypothesis (3) seems to be the most likely one at this time. Future work may help to clarify the situation.

4.5 INTERPRELATION OF RESONANT LIGHT TRANSMITTANCE MEASUREMENTS

One way to study the adsorption of mercury in NMR cells is to measure the temperature dependence of the mercury vapor density. This can be done by monitoring the transmittance of 253.7 nm mercury resonance radiation through the cell and relating this quantitatively to the mercury vapor density.

The transmittance of the mercury vapor in a cell is given by

$$T = \frac{\int I(\omega) d\omega}{\int I_0(\omega) d\omega} = \frac{\int I_0(\omega) e^{-nk(\omega)d} d\omega}{\int I_0(\omega) d\omega}, \quad (18)$$

where

$I_0(\omega)$ and $I(\omega)$ are the incident and transmitted intensities, respectively at a frequency ω ,

n is the density of the vapor (atoms/unit volume),

$k(\omega)$ is the absorption coefficient per atom, and

d is the optical path length through the cell.

The calculation of transmittance is described in detail in reference 22, but a brief summary is presented here. In order to calculate the transmittance for a particular lamp/vapor combination, it is necessary to calculate the intensity profile $I_0(\omega)$ of the lamp and the absorption

coefficient $k(\omega)$ of the vapor, assuming a given operating temperature for both. The isotopic hyperfine structure of the lamp radiation and vapor absorption must be included in such a calculation, since the lamp and cell are usually fabricated using different mercury isotopes. The results of preliminary measurements showed that the effects of small quantities of other mercury isotopes, which are always present, must also be included.

Figure 10 shows the theoretically calculated curve of transmittance vs vapor density for a pure ^{204}Hg lamp through a vapor of 50% ^{199}Hg , 50% ^{201}Hg , which is the usual isotopic configuration for optically pumped Hg NMR. Also shown is the curve calculated for the actual isotopic concentrations of the lamp and vapor, according to assays performed by the supplier of the separated mercury isotopes. The predictions of this calculation were checked experimentally, as described below.

Experimental Details

In order to verify the predicted transmittance vs vapor density relation, measurements of transmittance were made using a wet cell, shown in Figure 11. The 1 cm spherical end is placed in an oven as well as in the path of the light beam, and is connected to the reservoir through a small constriction. The other end of the reservoir, containing a droplet of liquid mercury, is placed in a controlled temperature bath. The vapor pressure of mercury above the droplet, P_C , can be controlled by varying the bath temperature T_C . If the mean free path of the vapor atoms is small compared to the diameter of the reservoir tube, then normal hydrostatic conditions occur, and P_H , the pressure at the other end of the reservoir, is equal to P_C . For low vapor densities, where the mean free path is larger than the reservoir diameter, the conditions for Knudsen flow are met, and

$$P_H = P_C T_H/T_C. \quad (19)$$

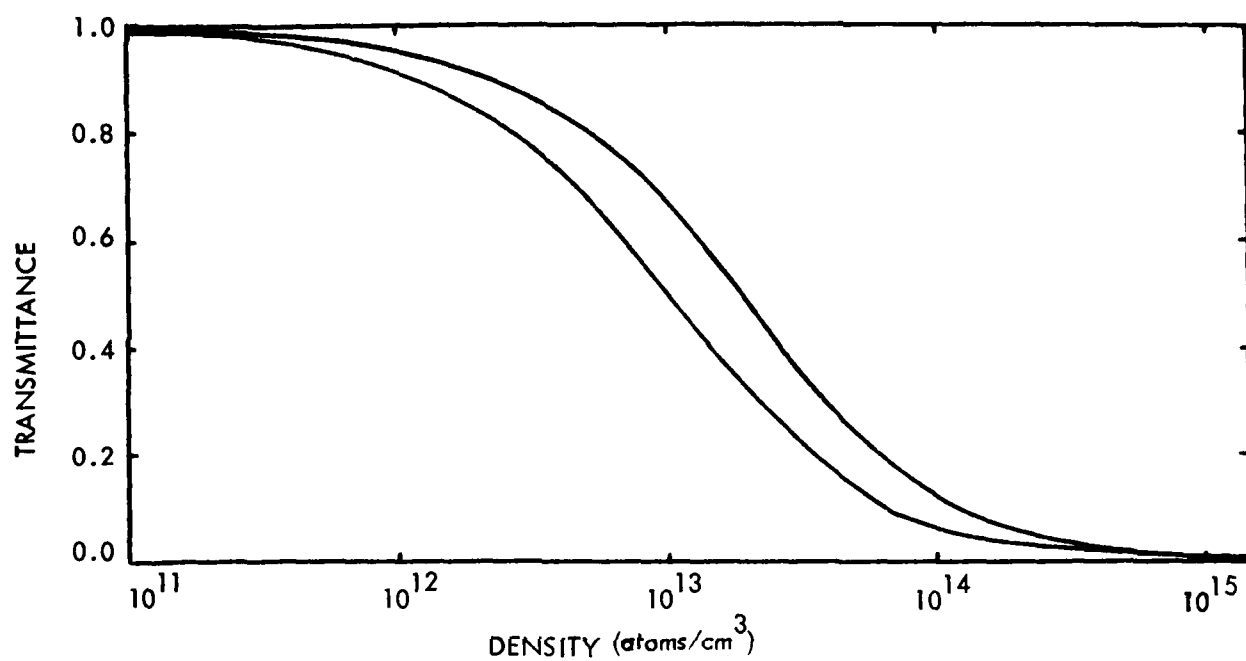


FIGURE 10 - Calculated Variation of Transmittance with Vapor Density for a 1 cm Path Length.

Lower Curve: Transmittance of radiation from a pure ^{204}Hg lamp through a vapor of 50% ^{199}Hg , 50% ^{201}Hg .

Upper Curve: Transmittance based upon isotopic impurities in the lamp and vapor.

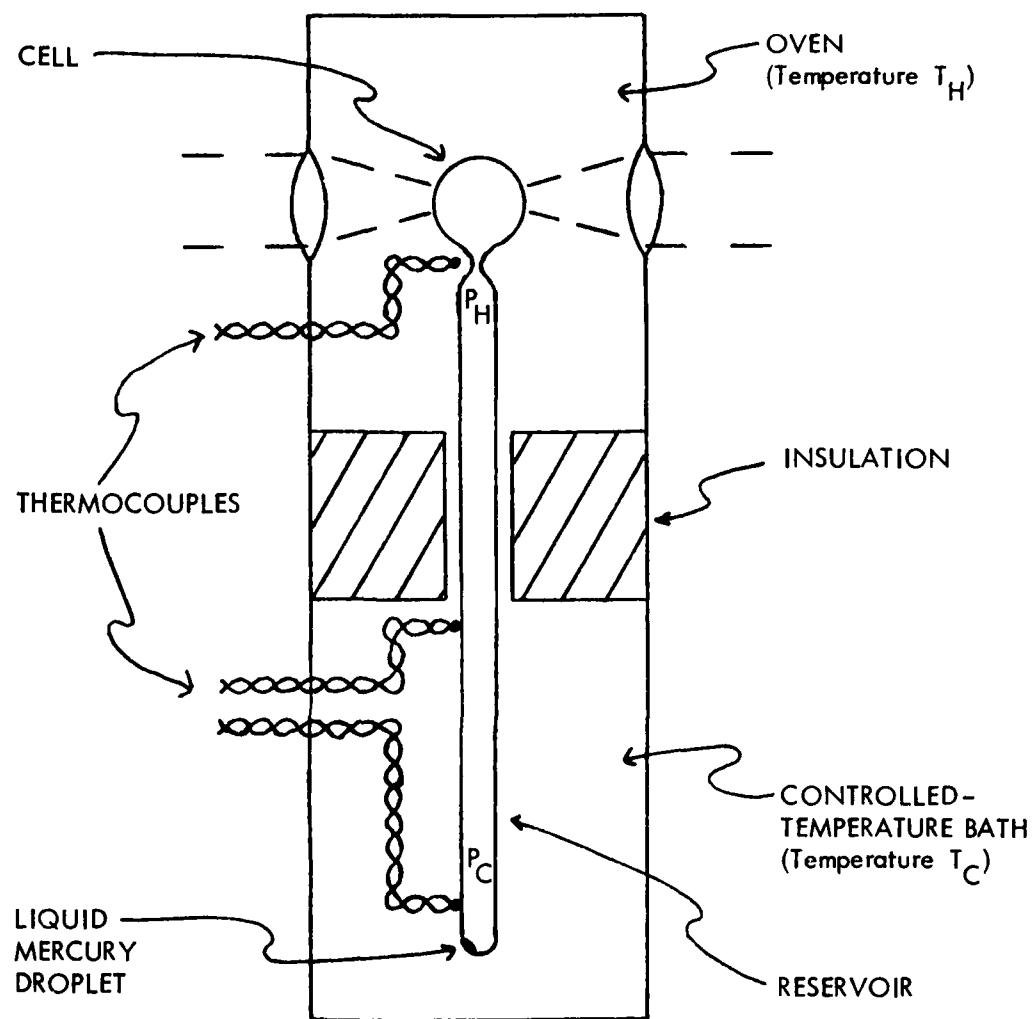


FIGURE 11 - Transmittance Measurement Apparatus

The mean free path is roughly equal to the 0.5 cm tube diameter at a vapor density of 2×10^{14} atoms/cm³, which corresponds to $T_C \approx 30^\circ\text{C}$, so both cases are realized in this experiment. However, the difference between Knudsen and hydrostatic densities is less than 20% over the temperature range attainable in the apparatus. The vapor on both sides of the constriction between the cell and reservoir is at the same temperature, so the pressure in the cell is equal to P_H . Since the pressure and temperature of the vapor in the cell are known, the density can be computed using the ideal gas law (which is valid for the low densities in the cell).

In order to measure the transmittance of the vapor within the cell, reflection and other losses due to the cell wall surface must be accounted for. This was done by placing the wet-cell reservoir in a liquid nitrogen bath to remove the mercury vapor from the cell.

Experimental Results

Figure 12 shows the results of a typical measurement on a wet cell. The abscissa is the vapor density in the cell, based upon the cell and reservoir temperatures, as measured by copper-constantan thermocouples (see Figure 11), assuming Knudsen flow conditions. The ordinate is the transmitted intensity, expressed as a fraction of the intensity for an "empty" cell, which occurred when the reservoir was immersed in liquid nitrogen. The transmittance of the "empty" cell was reproducible to within two percent. The curve is the calculated transmittance, assuming isotopic impurities, and it can be seen that the experimental results agree well with the predicted results.

Measurements of the transmittance of several empty cell blanks yielded values between 75% and 85%. This variability is attributed to differences in cell dimensions and mounting positions. Exterior surface contamination was removed by HF rinsing.

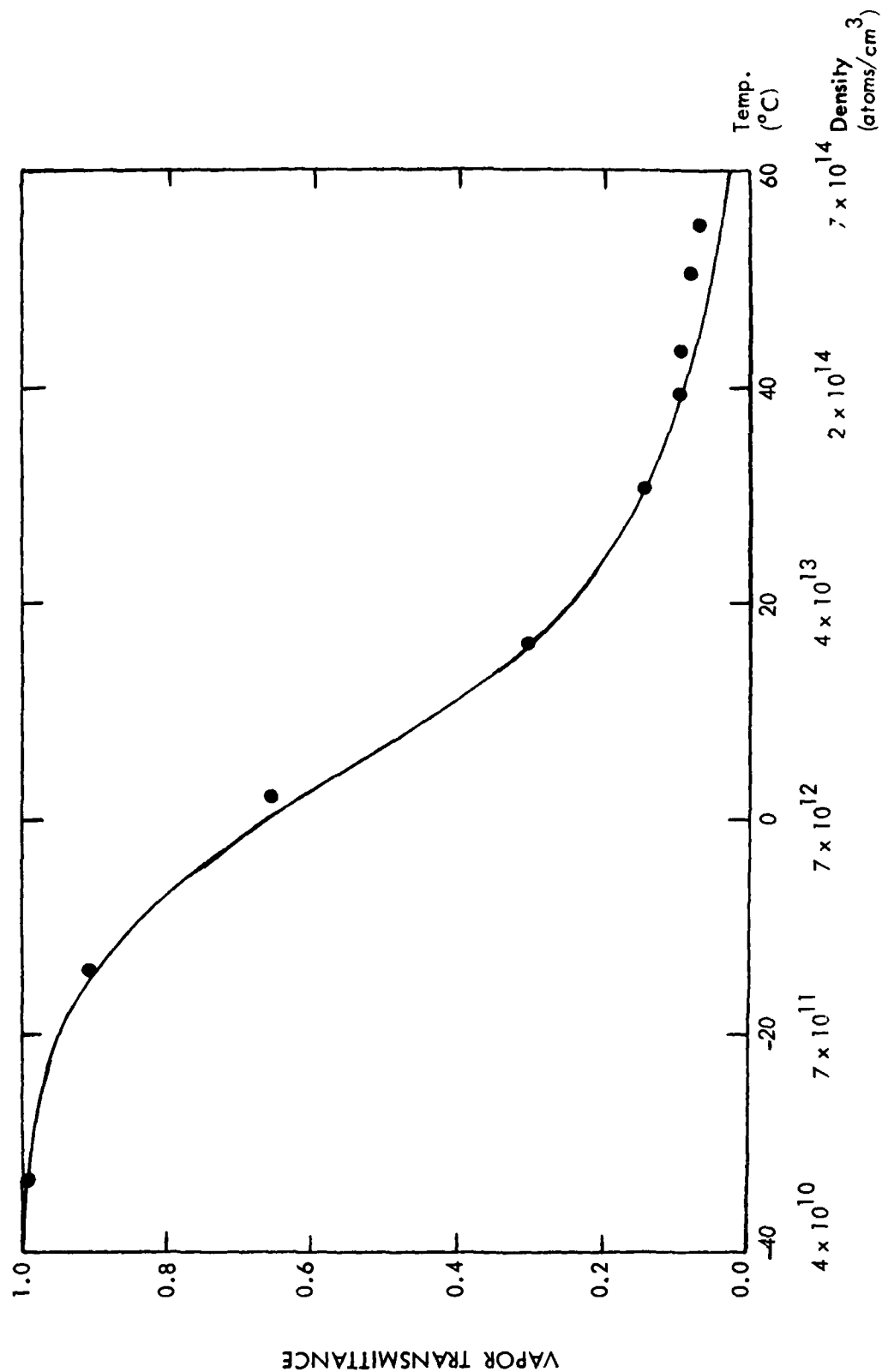


FIGURE 12 - Transmittance of Wet Cell vs. Reservoir Temperature

Most NMR cells at elevated temperatures have transmittances from 10% to 25%, which corresponds to a range of mercury vapor density of about 10^{13} to 10^{14} atoms/cm³. Large variations of transmittance of individual cells with temperature and exposure to resonance radiation have been observed. These variations are not attributable to the physisorption mentioned previously. The fraction of mercury atoms bound to the walls by physisorption is given by the ratio $\tau_s/(\tau_s + \tau_v)$. At 300 K and with $E_a = .3$ eV, this ratio is 4×10^{-4} , indicating that physisorption by the walls has no significant effect on the mercury vapor density above room temperature.

In some NMR cells the mercury vapor density is strongly affected by the resonance radiation of the pump lamp. The proposed mechanism is that the mercury atoms that are raised to the 3P_1 excited state by the pump lamp are interacting with the wall. These atoms, which have absorbed a 253.7 nm photon, possess 4.89 eV of energy above their ground-state energy level. This energy can enable the atoms to react with the silica surface by breaking existing bonds and forming new ones. One can estimate the number of excited mercury atoms striking the wall each second (ϕ). Given,

N_o = total number of gaseous mercury atoms,

T_{ex} = excited state lifetime $\sim 10^{-7}$ sec,

T_p^{-1} = pumping rate $\sim 10^{-1}$ sec,

τ_v = average time of flight of mercury atoms $\sim 5 \times 10^{-5}$ sec,

one gets

$$\phi \sim \tau_p^{-1} T_{ex} \tau_v^{-1} \quad (20a)$$

$$\sim 2 \times 10^{-4} N_o \left(\frac{\text{atom}}{\text{sec}} \right) \quad (20b)$$

$$\sim 10^{-2} N_o \left(\frac{\text{atom}}{\text{min}} \right) . \quad (20c)$$

If all excited mercury atoms that struck the wall stuck, and none were released, the number of atoms in the vapor would be given by

$$N_0 = N_I e^{-t/100}, \quad (21)$$

where

t is time in minutes, and

N_I is the initial number of vapor atoms.

Figure 13 shows the change in mercury vapor density in NMR cell W-123 at 200°C plotted against the time of exposure to the pump beam. When the pump beam was blocked, the density remained fairly stable. When the cell was exposed the density changed in a manner which can be approximated by

$$N_0 = 2 \times 10^{14} e^{-t/219}. \quad (22)$$

This is approximately $\frac{1}{2}$ the estimated rate of excited mercury atoms striking the wall. Relaxation measurements made during the course of the above experiment indicated that the sticking time for ground state atoms was very short and that the relaxation properties of the wall were changing only slightly.

During the course of the experiment, about 10^{14} mercury atoms were removed from the vapor phase. These atoms would form about 0.1 surface monolayer if they all bonded to the surface and remained on the surface during the experiment. If a 0.1 monolayer was formed, it is remarkable that the relaxation properties of the surface were not significantly affected. Other possible explanations exist for the change in mercury vapor density: The mercury may be interacting with an impurity, gaseous or on the surface, or the mercury may be diffusing into surface cracks, for example. However, no direct evidence exists at this time to indicate that these processes are occurring at the rate at which the mercury vapor disappeared in this experiment.

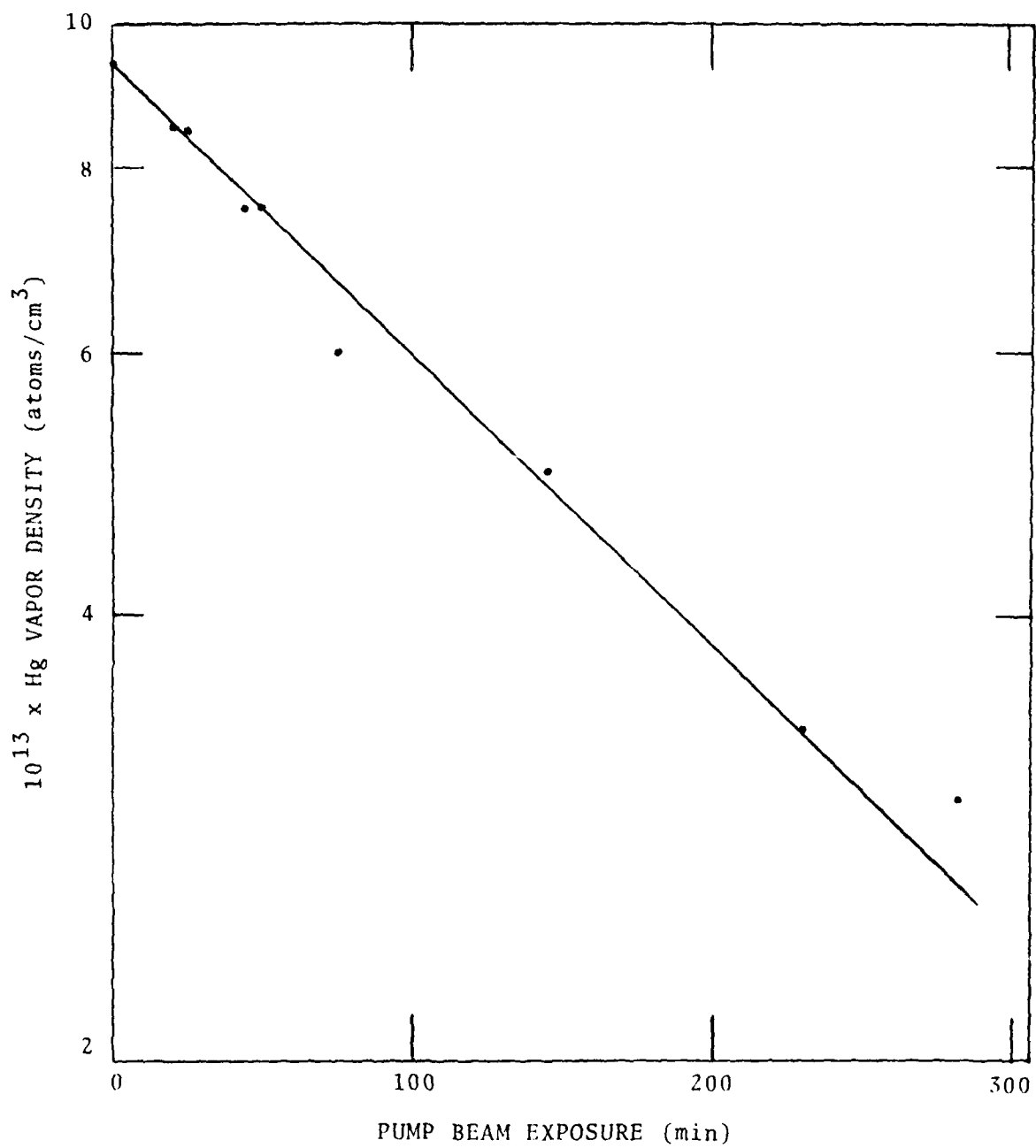


FIGURE 13 - Mercury Vapor Density vs Pump Beam Exposure
for Cell W-123

The mercury vapor density can often be restored after such a disappearance by heating the cell to 900 °C. We have no specific model for the process that is occurring. In this case, cell W-123 was raised to 900 °C for 15 minutes. Subsequently, the mercury vapor density at 200 °C was 1.3×10^{14} atoms/cm³, about 65% of the original value. The density at 200 °C was reduced during testing of the cell at temperatures up to 400 °C, but the density eventually stabilized at 6×10^{13} atoms/cm³ at 200 °C. Fused silica cells have generally had initially large variations in mercury vapor density which gradually diminish during a series of high temperature heat treatments.

4.6 COMPARISON OF CELL WALL MATERIAL

The different types of fused silica that were tested in this program are listed in Table 3, along with comparative performances. The stability column refers to the constancy of the mercury vapor density and the relaxation times, when the cell is at 200 °C and is exposed to pumping radiation. Suprasil W proved to be a significantly better wall material than the others. It is also one of the purest in terms of OH content and metallic impurities according to manufacturers estimates and the data of Fratello et al.⁸ A major contaminant in fused silica is chlorine, which is relatively low in Suprasil, although the data is incomplete for the other materials. Although there is a strong correlation between cell performance and material purity, it is not clear what variable or variables determine the cell wall performance. While these data point up differences among materials, the temperature dependence of relaxation times brings out a general similarity in the way in which ground state mercury atoms interact with cell walls of different materials.

TABLE 3 - Comparison of Cell Wall Materials

	Manufacturer	Type	OH Content (ppm)	Metallic Impurities (ppm)	E_a (eV)	Maximum Relaxation Times (sec) τ_{199} τ_{201}	Mercury Vapor Density
Suprasil W	Amersil Inc.	Synthetic	low	~.2	.24	695 265	stable
Suprasil	Amersil Inc.	Synthetic	high	~.2	.23	94 91	unstable
GE204	General Electric	Natural	low	50	---	<1 <1	stable
Tetrasil SE	Electro- quartz (France)	Synthetic	low	<.2	---	60 60	stable
9741 glass	Corning Glass Works	Pyrex glass		20-300 Na_2O	.22	1020 43	unstable
Spectrosil WF	Thermal American Fused Quartz Co.	Synthetic	low	<.2	---	86 58	unstable

5. COMPLEMENTARY INVESTIGATIONS

In order to obtain more information on the interaction between mercury atoms and a fused silica surface, several experiments were performed. Two experiments were done using a commercially available, finely divided, silica powder. One experiment (Section 5.1) involved mercury vapor transmittance measurements similar to those described above, and the second one (Section 5.2) involved infrared transmittance measurements of the fused silica. The second experiment could indicate specific silica sites that were interacting with the mercury vapor. A third approach (Section 5.3) involved direct examination of cell walls using X-ray photoelectron spectroscopy. Some properties of "glassblower's smoke" and its effect on cell characteristics are presented in Section 5.4. A study of a dark film that appears in mercury lamps is presented in Section 5.5.

5.1 ADSORPTION MEASUREMENTS OF MERCURY ON SILICA POWDER

The requirement for achieving a high surface area was met by using silica powder (also called pyrogenic or fumed silica), which consists of particles with diameters of about 20 nm, resulting in a surface area of nearly 200 m²/g. Its density is about .03 g/cm³ and it can be compressed easily to about 1 g/cm³ with only a small (~10%) loss in surface area with a small sample size. The experiments which are described in this chapter were conducted using Cab-O-Sil, a powdered silica commercially available from Cabot Corp., Boston, MA.

The powdered silica received a vacuum treatment which was similar to the treatment given to NMR cells. After being compressed as mentioned above, it was baked under vacuum at about 800 °C. While this temperature was not as high as the typical 1000 °C cell bakeout temperature, it was high enough to remove a large fraction of the chemisorbed water²³ and to allow for substantial outgassing of other impurities. Since the starting material, the fabrication methods, and the subsequent heat treatments were very similar to

those of the high-purity fused silica, such as Suprasil W, which is used for NMR cells, and since the powder particle size was large on an atomic scale, it was reasonable to assume that the powder surface was similar to the surface of the NMR cell wall.

In this experiment a small amount of mercury was sealed off in a tube with a predetermined amount of powdered silica. Changes in the density of the vapor were assumed to result from adsorption of mercury atoms onto the silica.

The experimental apparatus is shown in Figure 14. A small amount (0.6 mg) of ^{204}Hg was placed in one arm of a T-shaped evacuated tube. The second arm was connected to a disk-shaped transmittance cell, which provided an interior path length of 1/4" between 1" diameter windows. The remaining arm was connected, via a break-tip seal, to an ampoule, which contained about one gram of powdered silica. The powdered silica had been compressed, and then baked in the ampoule at 800 °C for one hour at 5×10^{-6} torr before the ampoule was sealed. The tubing and transmittance cell were constructed from fused silica.

The experimental procedure was to monitor the mercury vapor density by measuring the transmittance of 253.7 nm light from a ^{204}Hg lamp during the following procedures:

1. Before breaking the seal: The vapor density was determined by the vapor pressure of the liquid mercury droplet. By dipping the tube containing the droplet into liquid nitrogen, the mercury vapor could be removed from the transmittance cell, providing a measurement of the transmittance of the empty cell.
2. After breaking the seal: The vapor density would drop as vapor was adsorbed by the silica powder.

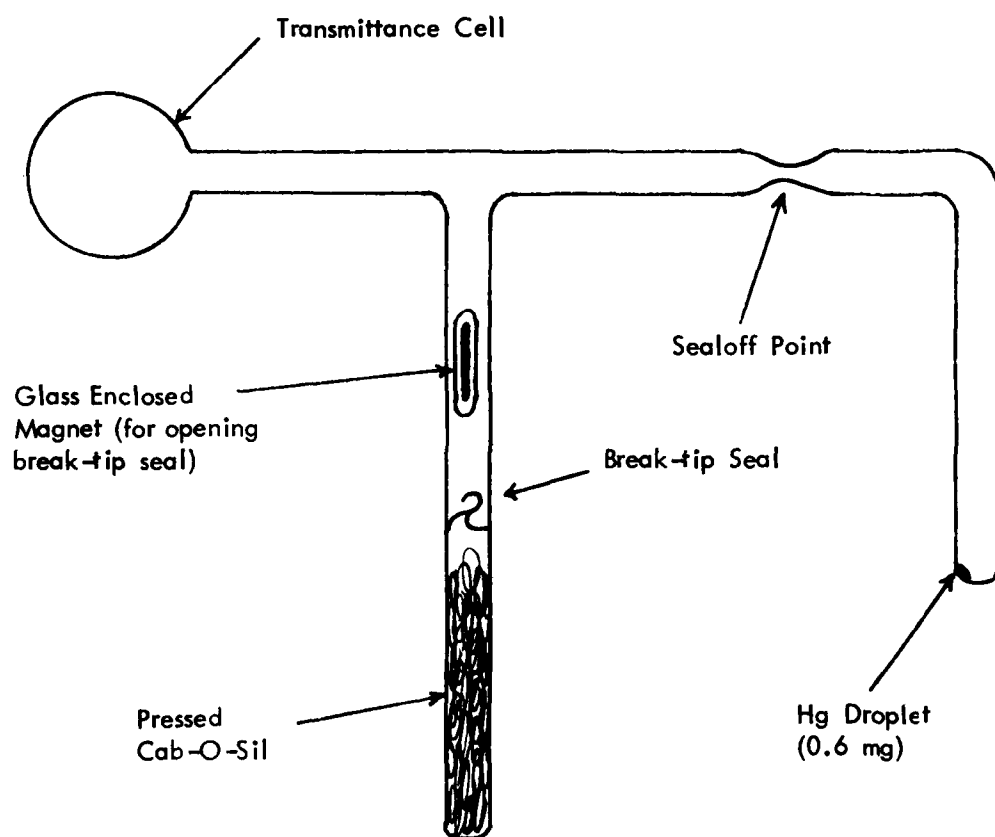


FIGURE 14 Apparatus for Adsorption Experiment

- a) If the mercury were completely adsorbed, the vapor density would stabilize at a value lower than the starting density. Subsequent heating of the silica powder would desorb some of the mercury, and would provide a means of studying adsorption vs temperature.
 - b) If the mercury were not completely adsorbed, the vapor density would return to its initial value. Examination of the liquid droplet might reveal a change in its size.
3. After removing the physisorbed mercury: By placing the tube end (which may or may not still have contained liquid mercury) into liquid nitrogen, the mercury vapor would be condensed into the tube. Once this portion of the tube was sealed off, the vapor density in the rest of the system would be near zero, causing any physisorbed mercury to desorb from the powdered silica. The vapor density would therefore increase and then stabilize at some non-zero value.
 4. After heating and cooling the powdered silica: Heating the powder would cause more mercury to desorb, thereby increasing the vapor density. Subsequent cooling would cause readsorption and a lower vapor density.

The results of this experiment are shown schematically in Figure 15. The vertical axis is the transmittance of the mercury vapor, drawn such that the transmittance increases toward the bottom of the figure and points nearer the top of the figure correspond to higher vapor densities. The horizontal axis corresponds to time, but it is not drawn to scale. The transmittance always stabilized within a few hours or less, although several days often elapsed between the various events shown. Therefore, the flat portions of the curve

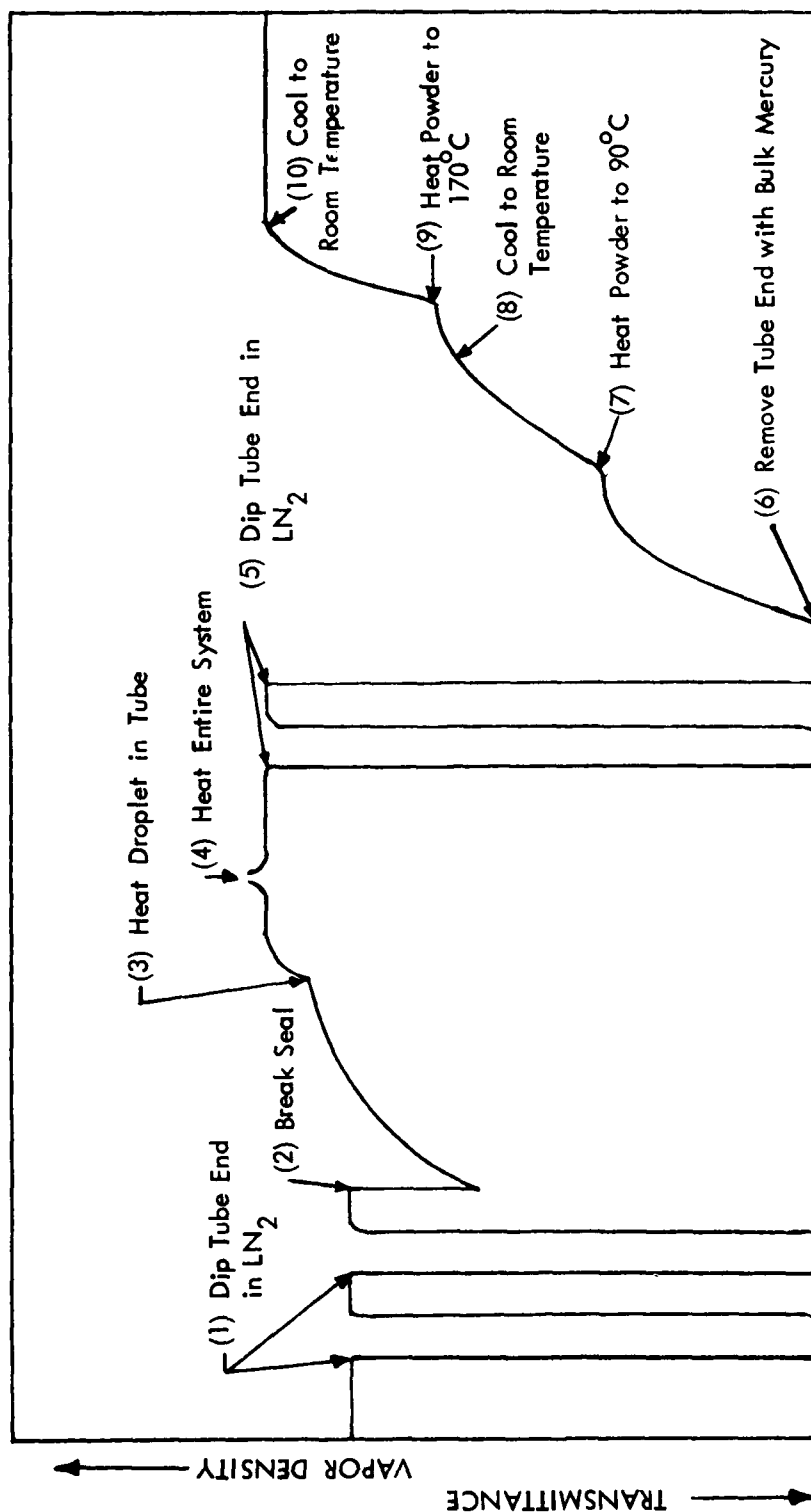


FIGURE 15 - Changes in Mercury Vapor Density During Mercury-Silica Adsorption Experiment

correspond to a much longer time interval than the sloped portions. The results are as follows:

1. The initial transmittance was determined by immersing the tube containing the droplet into liquid nitrogen several times. As the droplet warmed up, the vapor density returned to its previous value.
2. When the break tip was broken, the vapor density decreased slightly. By the next morning, it had stabilized at a value slightly higher than the density before breaking the seal. The droplet was still visible, and had not decreased noticeably in size. A possible explanation for the increase in vapor density is that impurities are often present as a film on the surface of liquid mercury, which limits the vapor pressure of that liquid. If such a film were present, the sudden change caused by breaking the tip could possibly have ruptured the film, increasing the vapor pressure of the droplet. This is also a possible explanation for the results of the next step.
3. The tube containing the droplet was heated to 76°C for 5 minutes. The vapor density increased slightly, and did not decrease when the tube was returned to room temperature. There was still no visible change in droplet size.
4. The entire system was heated to 155°C . This temperature had been calculated to be sufficient to vaporize the entire droplet. The vapor density could not be measured while the system was being heated in a separate oven. During cooling, the tube end was kept in ice water. Several droplets of mercury condensed in the tube, but the vapor density returned to its previous value.

5. The tube end was dipped in liquid nitrogen, and sealoff began.
6. The sealoff was completed within three minutes. The vapor density gradually increased, and stabilized at a value approximately 25% of the density before sealoff.
- 7-10. When the powder was heated, the vapor density increased, but it did not decrease upon subsequent cooling. Eventually, the vapor density reached its value before sealoff. Two weeks later, it had not changed.

A possible explanation for the lack of a decrease in vapor density is that there were microscopic droplets of mercury trapped in the spaces between the particles of the silica powder. Such mercury probably would have been introduced during the heating of step 5, and would be liberated during the heating of steps 7 and 9.

A clear result of this experiment is that very little mercury was adsorbed by the powdered silica. If all of the 0.6 mg of mercury had been adsorbed by the 1 g of powdered silica with a surface area of $200 \text{ m}^2/\text{g}$, the coverage would have been one atom in an area of 100 nm^2 (10^4 \AA^2). One monolayer is approximately 15 atoms per nm^2 (or one atom per $7 \times 10^{-2} \text{ nm}^2$). Since the droplet did not change visibly in size, a conservative estimate is that at most 10% of the liquid was adsorbed, which yields a coverage of one atom per 10^3 nm^2 . Since, at room temperature, approximately $3 \times 10^{17} \text{ atoms/cm}^2 \text{ sec}$ strike the sample surface¹⁸, this coverage would correspond to an upper limit on the average sticking time of $3 \times 10^{-7} \text{ sec}$, which is consistent with the previously mentioned value of $2 \times 10^{-9} \text{ sec}$, determined from our NMR measurements.

The result for sticking time is also consistent with that of Bonnot and Cagnac¹⁵ as determined by the magnetic field dependence of mercury NMR relaxation times. The adsorption results also agree

with those of Liebich and Fink,²⁴ who measured the adsorption of radioactive ^{203}Hg on Aerosil (another brand of silica powder) by monitoring the radioactive decay of those atoms which were adsorbed. Working at vapor densities about 5-50 times higher than in the above experiment they found a coverage of less than one atom per 10^4 nm^2 .

5.2 CHEMISORPTION OF MERCURY ON SILICA POWDER

If mercury atoms bond chemically to a fused silica surface, the IR absorption properties of certain surface features can be altered. Various possible surface states are shown schematically in Figure 4. Many of these features can be detected easily by infrared transmission spectroscopy of a powdered silica sample which has been compressed into a self-supporting disk. A portion of a typical transmittance spectrum between 4000 and 3000 cm^{-1} ($2.5\text{-}3.3\mu\text{m}$) is shown in Figure 16. The spectrum contains features which have been identified as arising from the vibrational motion of isolated surface silanols, hydrogen-bonded surface silanols, and molecular water trapped within the disk.²³

The isolated silanol O-H group can be modelled as two masses attached by a spring, with a stretching vibration which causes a sharp infrared absorption band at 3748 cm^{-1} ($2.64 \mu\text{m}$). If another atom (for instance, mercury) interacts with any of the atoms which make up the silanol, the effective masses or the spring force constant is changed, resulting in a shift of the vibrational frequency and of the wavelength of the infrared absorption. For instance, at -190°C , argon causes a shift of as much as 40 cm^{-1} , and nitrogen as much as 43 cm^{-1} . Ammonia at room temperature causes a shift of 900 cm^{-1} . If chemisorption occurs, then the O-H bond is replaced by a new bond, and the 3748 cm^{-1} band weakens or disappears. Therefore, the interaction between mercury vapor and these silanols can be studied by monitoring the intensity and position of this silanol absorption band. If the silanols are found to be active sites for mercury interaction, then efforts might be made to eliminate them from the surface of the NMR cells. Conversely, if they do not interact strongly with mercury,

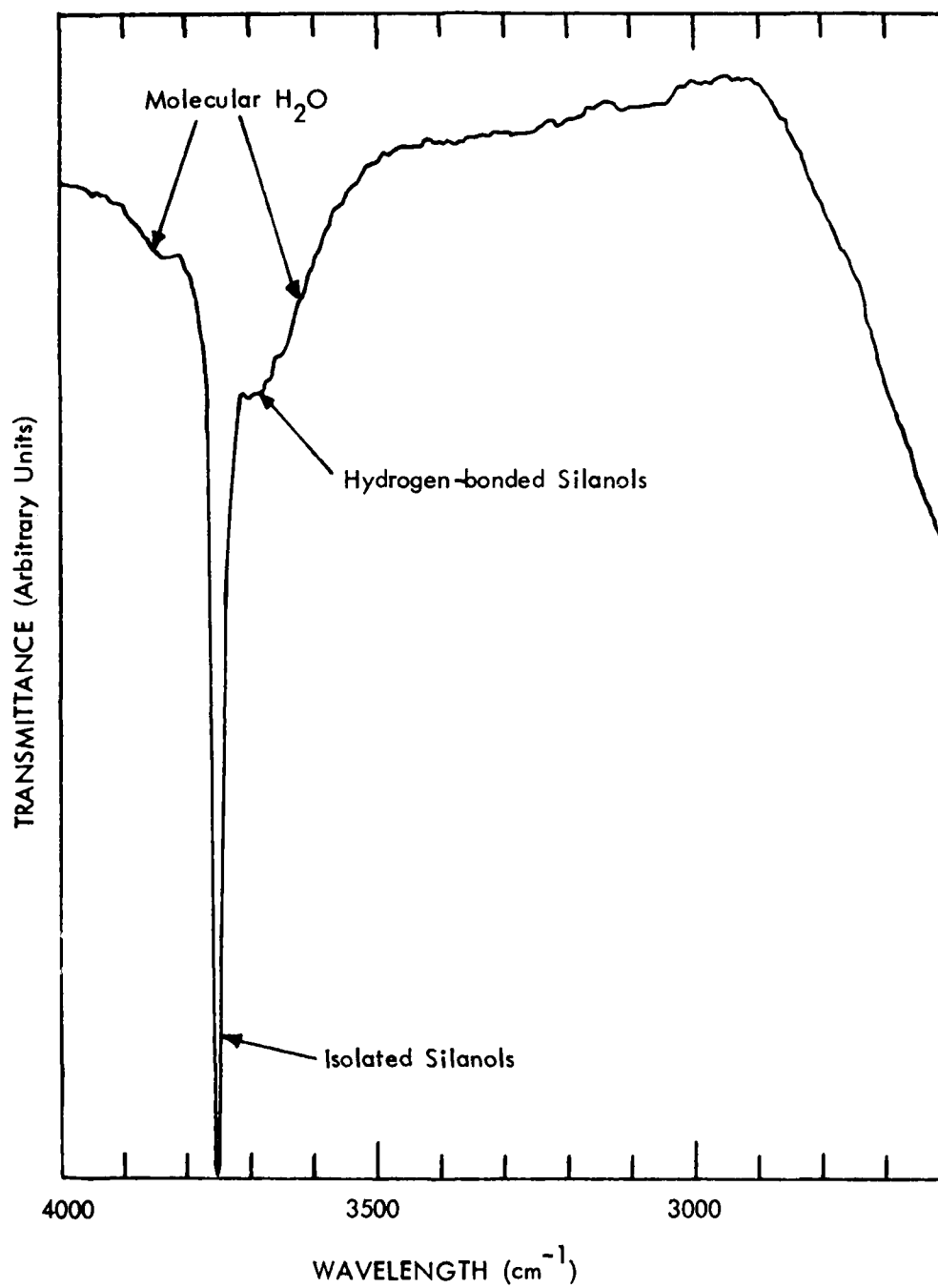


FIGURE 16 - Infrared Transmittance Spectrum of Powdered Silica

then attempts might be made to determine the effect of increasing the concentration of this type of surface site.

The vacuum system for studying infrared transmittance is shown in Figure 17. The area around the sample is made from square-cross-section water-free fused silica tubing which can fit into the infrared spectrophotometer. Since water-free fused silica is transparent at wavelengths below $3.5\ \mu\text{m}$, the flat sides of the tubing serve as suitable windows. This small system is attached to another system (with greater pumping capacity) for initial pump-down and bake-out. After seal-off from the larger system, the small system is continuously pumped by the getter. Mercury is introduced by breaking the break-tip seal, and is removed by immersing the mercury reservoir in liquid nitrogen. Note that this system is the opposite of the one described above, where the powdered silica was in a region separated from the rest of the system by a break-tip seal. Using this system, a pressed-silica disk can be studied before, during, and after exposure to mercury vapor.

The sample was baked under vacuum overnight at $500\ ^\circ\text{C}$, and then heated to $720\ ^\circ\text{C}$ for 1 hour. After cooling, the sample holder was removed from the vacuum system, and infrared transmittance spectra were measured as follows:

1. Immediately after sealoff
2. The next day
3. Immediately after exposure to mercury vapor
4. After four days exposure
5. After five hours exposure to resonance radiation from a ^{202}Hg lamp, still in the presence of the mercury vapor
6. After 13 hours exposure to uv
7. After 21 hours exposure to uv
8. After 120 hours exposure to uv
9. After about 100 hours exposure to uv with the sample heated to $300\ ^\circ\text{C}$ during the time of exposure
10. After four months exposure to mercury vapor at room temperature without resonance radiation.

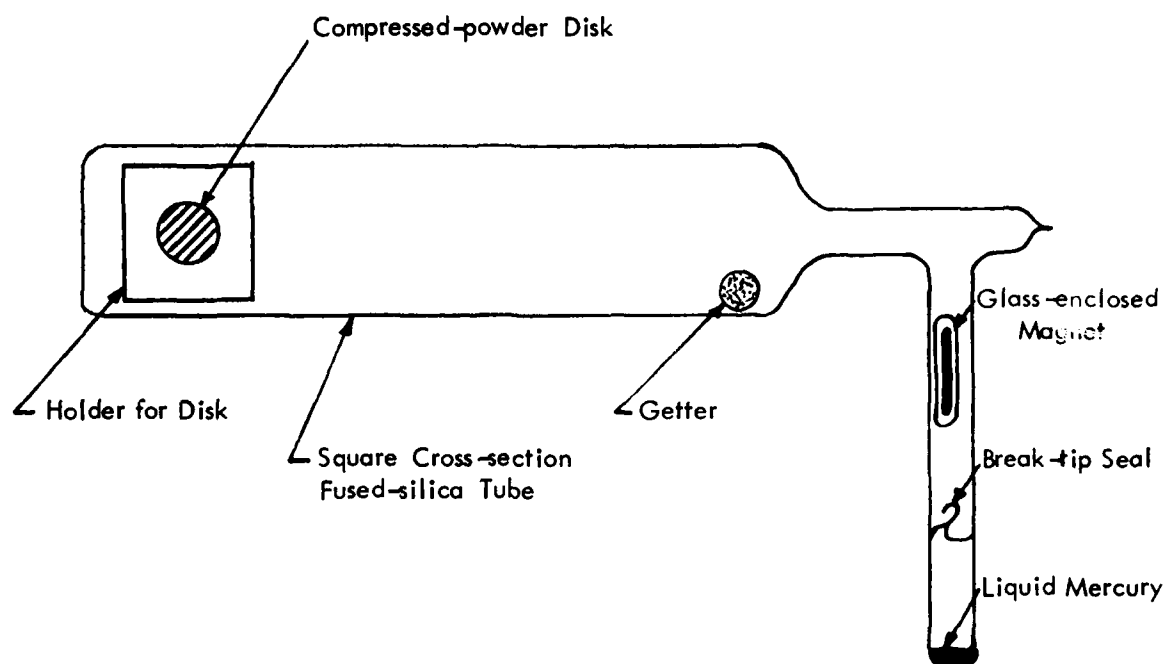


FIGURE 17 - Sample Holder for Infrared Transmittance Measurement Under Vacuum

Figure 18 shows the transmission spectrum of the powdered silica in the wavelength region of the isolated-silanol absorption band. The wavelength axis is expanded by a factor of 20 over that of Figure 18, in order to pinpoint the position and the amount of minimum transmission. The difference between the measured value (3754 cm^{-1}) and the expected value (3748 cm^{-1}) of the band minimum is within the wavelength adjustment tolerance of the spectrophotometer.

The spectrum in the figure was taken after step 10 above, but, except for a random scatter of $2\text{-}3\text{ cm}^{-1}$, it looks exactly like the spectra taken after all the other steps. No significant shift in the position of the 3748 cm^{-1} band was found within the 5 cm^{-1} resolution of the spectrophotometer. The intensity of the band center was constant, with the transmittance always less than one percent. These results indicate that the mercury vapor did not measurably affect the surface silanol groups, even during exposure to mercury resonance radiation.

In the experiments involving the silica powder, no interaction was observed between the mercury vapor and the silica surface. These results can be used to indicate an upper limit to certain possible mercury-silica interactions, but provide no specific indication of the processes that occur in NMR cells. It is possible however that a refinement or an extension of these experiments, would provide results on other processes such as interactions between mercury vapor and the stretched bridging oxygens, which form when silica is heated above 900°C in vacuum.

5.3 SURFACE ANALYSIS OF CELL WALL MATERIALS

Much information on the relaxation of mercury nuclear spins has been obtained through measurements of the decay rate of signals arising from optically-detected precession of the spins. However, this technique cannot measure directly the interaction between the cell wall and a mercury atom at a specific site on the wall during a single short sticking time, and it cannot characterize the state of the

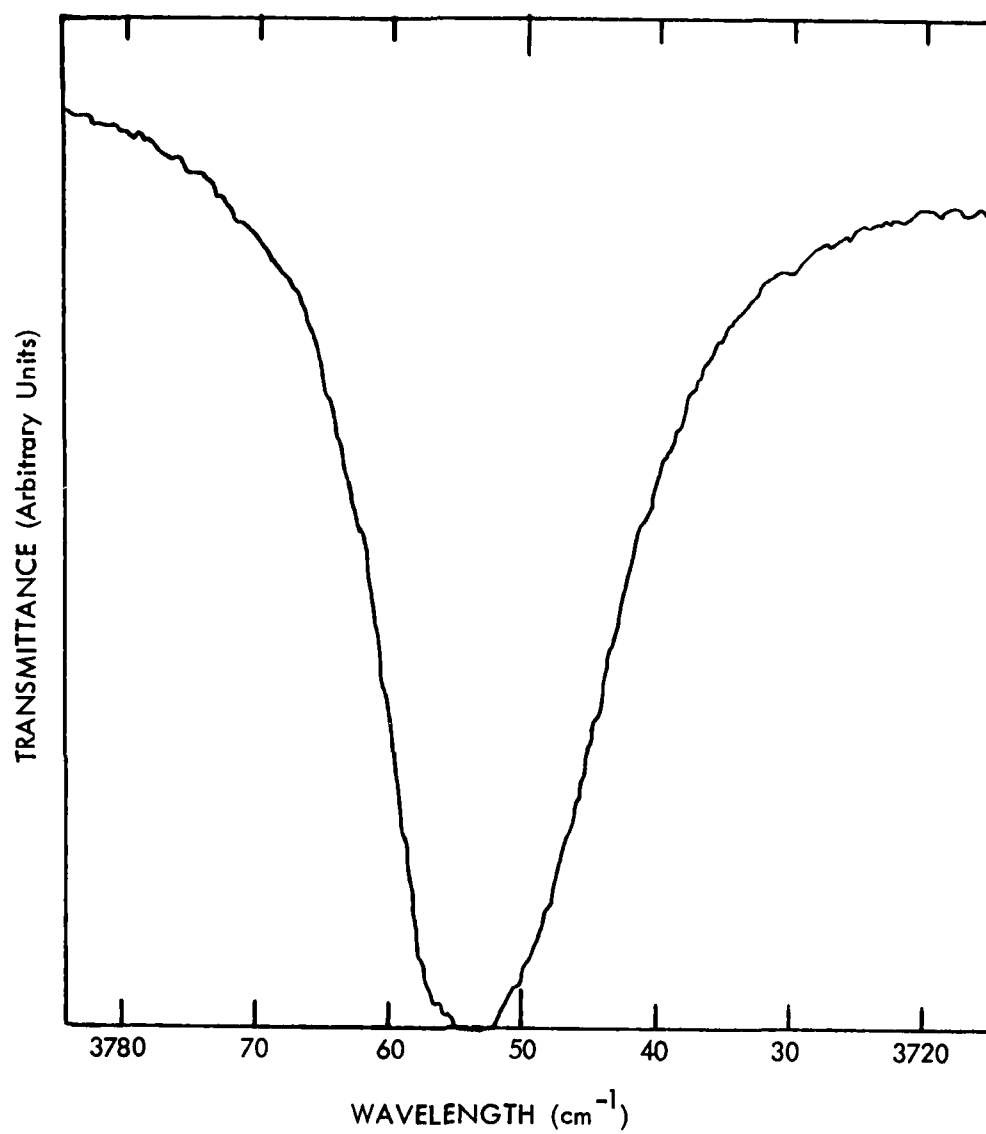


FIGURE 18 - Expanded-Wavelength Infrared Transmittance Spectrum of Powdered Silica Showing Surface Silanol Absorption Band.

1

wall surface, except in general macroscopic terms. Various surface spectroscopic techniques, including X-ray photoelectron spectroscopy (XPS or ESCA), secondary-ion mass spectroscopy, ion scattering spectroscopy, and Auger electron spectroscopy, recently have become readily available. These techniques are sensitive to the atomic composition and oxidation states of the atoms in the first few atomic layers, which is the portion of the cell which interacts most strongly with the nuclear spins of the mercury vapor atoms. X-ray photoelectron spectroscopy can identify the atoms present at the surface and can also determine their oxidation state. Secondary-ion mass spectrometry is extremely sensitive for detection of certain impurities, especially alkali metal atoms. Ion scattering spectroscopy is sensitive only to the outermost atoms at the surface, which are the atoms which interact most strongly with the mercury nuclear spins. Auger electron spectroscopy is sensitive to the electronic state of the surface atoms, and has an imaging capability with a resolution of 0.2 microns.

The main disadvantage of these techniques is that the cell must be broken in order to perform the analyses. It is possible that the cell wall might change during the process of breaking the cell, mounting a piece of the cell wall into a sample holder, and inserting it into the vacuum system for analysis. Despite this drawback, these analysis techniques can aid greatly in characterizing impurities that might be present on the cell surface.

Several cell surfaces were analyzed by XPS. This technique was chosen because knowledge of the oxidation state of the atoms was desirable and because XPS causes the least amount of damage to surfaces such as silica. The analyses were performed at the analytical laboratory of Perkin-Elmer, Physical Electronics Div., Eden Prairie, Minn.

Three cells were investigated: W-133 (a high-quality cell), W-132 (a high-quality cell which had been degraded by exposure to resonant

uv) and a control cell (a cell which had been sealed off with mercury, but had not been heat treated). All cell surfaces were found to have silicon and oxygen in chemical states identical to that of SiO_2 . No mercury and no other impurities were detected. No differences in surface composition or structure were found, except for variations in the distribution of chemical states of carbon adsorbed from the lab atmosphere. It is not known whether this difference was significant in relation to cell performance or if it was due to random variations among the samples. The results of these tests indicate that the difference between good and bad cells is not due to an overall change in composition, but that it is due either to some subtle change of the entire cell surface or to a gross change of a small portion of the cell surface area.

These observations indicate that the fabrication, bakeout, and processing of the cells remove most foreign substances and result in cells with clean SiO_2 walls. Hydrogen, as well as oxygen combined with elements other than silicon, may also have been present, but could not be observed by the techniques employed.

5.4 SILICA GLASSBLOWER'S SMOKE

It had been suggested that the relaxation of mercury in fused silica cells might be affected by particles of so-called "glassblower's smoke" which may end up in the cell after sealoff. This "smoke" is a white, powdery film which is produced during the strong heating needed for shaping of fused silica and perhaps during the sealoff of cells. The film was determined by XPS surface analysis to be fused silica (SiO_2). Such small particles of fused silica may have different surface properties than the silica of the cell wall, and may cause relaxation of the mercury nuclear spins. Experiments were performed to test whether this material would be affected by the heat treatments which are known to improve the performance of NMR cells.

Several samples of silica "glassblower's smoke" were prepared to test whether such smoke is affected by a typical 950 °C cell heat treatment. The samples were divided into three groups: one receiving a bakeout at 980 °C for ten days under vacuum, another receiving a similar baking in the ambient air, and a control receiving no treatment. After treatment, no differences among the samples were seen under a 30X microscope. The samples were then examined under an electron microscope, where again no differences could be detected. Therefore, the glassblower's smoke, if present in the cell after sealoff, is probably not eliminated by heat treatment.

One of the NMR cells, W-164, contained a clearly visible amount of glassblower's smoke on its inside surface. The deposit was probably produced and distributed over the surface during fabrication of the cells and manifold. The performance of this cell was not markedly different from that of the other Suprasil cells in this batch, indicating that the surface relaxation properties of the deposit are similar to those of the cell wall.

5.5 THE DARK FILM IN MERCURY LAMPS

An rf-excited electrodeless-discharge mercury lamp is a system where mercury-silica interactions are expected to be stronger than the interactions in NMR cells. The dark film which often forms in these lamps has been investigated, using surface analysis and analytical chemical techniques, in order to gain insight into the mercury-silica interactions which can occur in both lamps and cells.

A presentation on this work was made at the March 1980 meeting of the American Physical Society, and a paper has been published in Applied Physics Letters.²⁵ (See Section 9.1)

The results of this investigation support the hypothesis that the interaction between mercury and fused silica is very weak, since the proposed chemical reactions only occur after the silica has been decomposed by sputtering.

6. QUADRUPOLE EFFECTS UPON THE ^{201}Hg MAGNETIC RESONANCE

In the previous section the transverse magnetic moments of ^{199}Hg and ^{201}Hg were considered to relax in a manner described by a simple exponential function. While this is true for ^{199}Hg , quadrupole perturbations can cause a non-exponential decay of ^{201}Hg .

6.1 INTRODUCTION

The nucleus of ^{201}Hg has a spin of $3/2$, and can be affected by quadrupole perturbations from various sources. Such perturbations can affect the relaxation of the nuclear spins, as well as their steady-state free precession.

A quadrupole perturbation is a small change in the magnetic energy levels of a system with a spin greater than one half. It has two properties of interest: energy levels with different values of $|m|$ have different shifts in energy, and the strength of the perturbation V varies with the angle θ between the perturbation symmetry axis and the quantization direction:

$$V \propto \frac{1}{2}(3\cos^2\theta - 1) = P_2(\cos\theta) \quad (23)$$

where $P_2(\cos\theta)$ is a second-order Legendre polynomial. Note that V changes sign as θ is varied from 0° to 90° , passing through $V = 0$ at $\theta = 54.74^\circ$, and that $V(\theta) = V(-\theta)$.

A quadrupole perturbation also causes a torque T , which is given by the derivative of V with respect to θ :

$$T \propto \cos\theta\sin\theta \propto \sin 2\theta \quad (24)$$

The torque is zero at $\theta = 0^\circ$ and at $\theta = 90^\circ$, but not at $\theta = 54.74^\circ$.

A rigorous quantum-mechanical description of a quadrupole perturbation yields terms proportional to the energy shift and to the torque,

along with a third term whose classical analog is less clear. This term can couple magnetic energy levels whose quantum numbers m differ by two, and it varies with angle as $\sin^2\theta$. It will be called the "2 ω " term in the discussion below.

The angular dependence of these three terms is illustrated in Figure 19.

6.2 QUADRUPOLE PERTURBATIONS DUE TO THE CELL WALL

There are two major sources of quadrupole perturbations in mercury magnetic resonance experiments: interactions with the cell wall, and interactions with the optical-pumping and readout light. Understanding the interactions between the mercury nuclei and the cell wall is the primary goal of this investigation.

The nucleus of ^{201}Hg has an electric quadrupole moment, and therefore a quadrupole perturbation can arise from the effects of an electric field gradient at the nucleus. Such a field gradient exists whenever the mercury atom is adsorbed onto the cell wall, regardless of the mechanism for adsorption. If an atom is adsorbed onto a surface, then there must be an electric field pulling it back toward the surface if it moves away, pushing it away from the surface if it gets too close, and equal to zero at the equilibrium distance from the surface (see Figure 20). Therefore, the electric field has a gradient normal to the surface.²⁶ A weakly adsorbed atom such as mercury on fused silica is usually free to hop about the surface, which indicates that any electric field gradients parallel to the surface are much weaker than the component normal to the surface.

The quadrupole moment Q of the nucleus is defined by

$$eQ = \int_{\text{volume of nucleus}} \rho r^2 (3\cos^2\theta - 1) dV \quad (25)$$

— Energy Shift
- - - Torque
..... 2ω

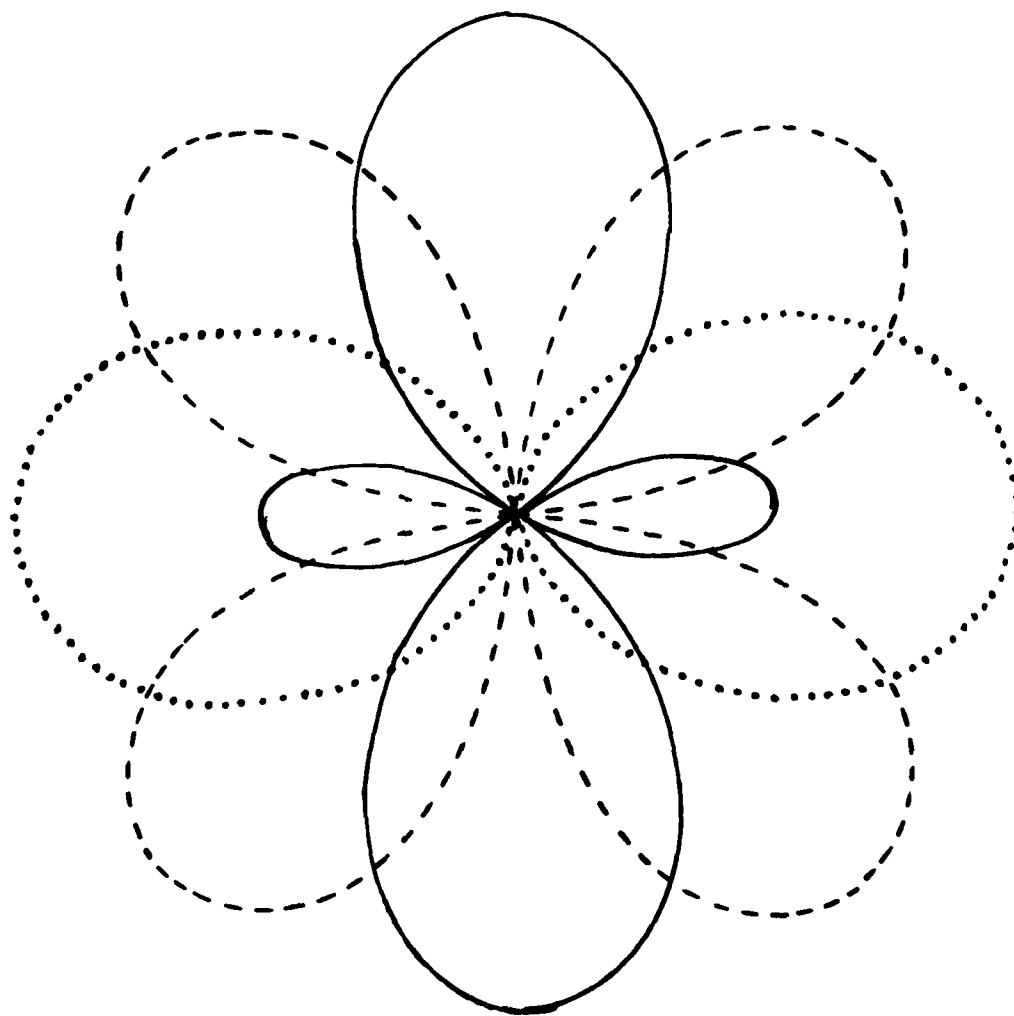


FIGURE 19 - Angular Dependence of Quadrupole Terms (Arbitrary Scale)

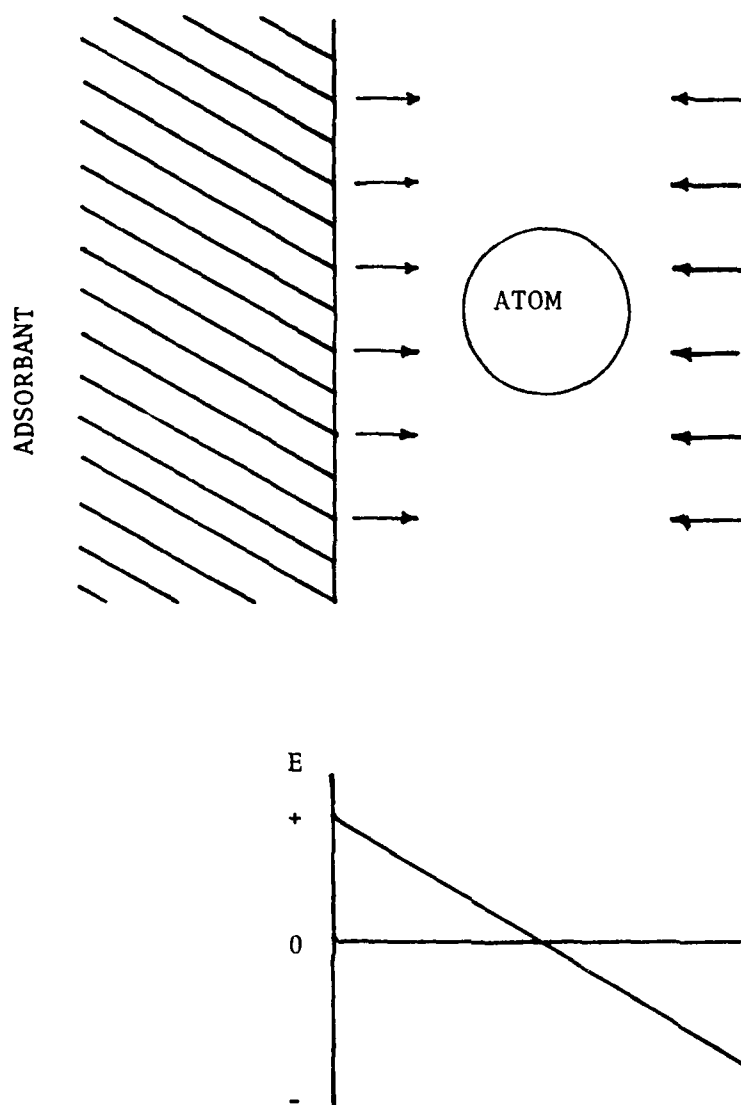


FIGURE 20 - Electric Field Near an Adsorbed Atom

where e is the magnitude of the electronic charge ($e > 0$), ρ is the charge density within the nucleus, and the integral is to be done for the nucleus in the $m = +1$ state (i.e., $m = +3/2$ for ^{201}Hg). The quadrupole moment of the nucleus is positive²⁷, which indicates that the nucleus is cigar-shaped, with the cigar parallel to the quantization direction when $m = \pm 3/2$. If this cigar-shaped distribution is placed in the electric field gradient described above, it will tend to orient its axis perpendicular to the field gradient axis. If the quantization axis is parallel to the field gradient axis ($\theta = 0^\circ$), then this orientation corresponds to a linear combination of $m = \pm 1/2$ states, and it indicates that the $\pm 3/2$ states have the higher energy. This corresponds to a positive quadrupole perturbation, which for a spin $3/2$ particle is defined as a perturbation which raises the $\pm 3/2$ levels relative to the $\pm 1/2$ levels at $\theta = 0$.

A polarized atom is adsorbed and desorbed many times before it is relaxed, and it therefore samples the entire cell surface. This results in a randomly fluctuating perturbation. If the strength of the field gradient is uniform over the entire cell wall, then it can be shown that both the energy shift term and the torque term average to zero over a cell which is a perfect sphere or a perfect cube. The 2ω term does not average to zero. A slight departure from these shapes, caused, for instance, by the sealoff tip, can result in a non-zero average value for the energy shift and torque terms as well, which implies a steady-state perturbation. The effects of this non-zero average energy shift have been studied previously.^{1,28}

In summary, the forces which cause adsorption on the cell wall also give rise to an electric field gradient at the nucleus, which causes a quadrupole perturbation on ^{201}Hg . The axis of this field gradient (and, therefore, of the perturbation) is directed normal to the surface. The average value of this randomly fluctuating perturbation is determined in part by the geometry and the orientation of the cell.

Explicit expressions describing the time dependence of free-precession signals of ^{201}Hg in the presence of quadrupole perturbation have been derived. They were checked experimentally using optical perturbations and the results were published.²⁹ (See Section 9.2)

6.3 COMBINED QUADRUPOLE PERTURBATION/TRANSVERSE MAGNETIC FIELD/ PUMPING RADIATION/RELAXATION

The situation is frequently encountered where the mercury nuclei are subjected to the combined effects of a steady-state magnetic field H_0 , a transverse rf magnetic field H_1 , a quadrupole perturbation, optical pumping radiation, and relaxation on the cell walls. The time dependence of the density matrix ρ is then given by

$$\frac{d\rho}{dt} = -\frac{i}{\hbar} (\mathcal{H}_0 + \mathcal{H}_1 + \mathcal{H}_Q) \rho + \frac{d\rho}{dt} |_{\text{pump}} + \frac{d\rho}{dt} |_{\text{relaxation}} \quad (26)$$

where the terms \mathcal{H}_0 , \mathcal{H}_1 , and \mathcal{H}_Q are the Hamiltonians corresponding to the H_0 and H_1 magnetic fields and to the quadrupole perturbation, respectively and are given by

$$\mathcal{H}_0 = \hbar\omega_0 I_z = \hbar\omega_0 \sqrt{5} T_{10}, \quad (27)$$

$$\mathcal{H}_1 = \hbar\omega_1 e^{-i\omega_a t I_z} (I_x) e^{i\omega_a t I_z} \quad (28a)$$

$$= \sqrt{5/2} \hbar\omega_1 e^{-i\omega_a t \sqrt{5} T_{10}} (T_{1,-1} - T_{1,1}) e^{i\omega_a t \sqrt{5} T_{10}}, \text{ and} \quad (28b)$$

$$\mathcal{H}_Q = \hbar\omega_Q \text{ for } m = \pm 3/2; -\hbar\omega_Q \text{ for } m = \pm 1/2 \quad (29a)$$

$$= \hbar\omega_Q T_{20}.$$

In the above equations, ω_0 is the Larmor frequency, ω_1 is proportional to the strength of the rf magnetic field ($\omega_1 = \gamma H_1$, where γ is the gyromagnetic ratio), ω_a is the frequency of the rf magnetic field, and ω_Q is proportional to the strength of the quadrupole perturbation. The terms of the quadrupole perturbation proportional to T_{21} and T_{22} have been neglected in this calculation. This implies either that the quadrupole axis is parallel to H_0 (where these terms are zero) or that only first-order perturbation is assumed.

The last two terms in equation (26) are assumed to be given by

$$\left. \frac{d\rho_{LM}}{dt} \right|_{\text{pump}} + \left. \frac{d\rho_{LM}}{dt} \right|_{\text{relaxation}} = -\frac{1}{\tau_L}(\rho_{LM} - R_{LM}), \quad (30)$$

where τ_L is the relaxation time for a spin distribution with multipolarity L , and R_{LM} is the steady-state value of ρ_{LM} due to optical pumping when no transverse field is present. An orientation distribution has $L = 1$ and an alignment distribution has $L = 2$. Also, R_{LM} is zero unless M is zero, for the case where optical pumping produces a longitudinal distribution.

The time dependence of the density matrix can be found using the method described in reference 27. The result is fifteen coupled differential equations with the fifteen variables $\rho_{LM}(t)$ for $L = 0$ to 3 and $M = 0$ to L , which are listed explicitly in Figure 21. The steady-state solutions can be assumed to have the form

$$\rho_{LM}(t) = e^{iM\omega_a t} \rho_{LM} \quad (31)$$

where ρ_{LM} is now used to designate the steady-state magnitudes of the various density matrix elements. These solutions are then substituted into the coupled differential equations, which then can be simplified to a set of simultaneous equations for the time-independent variables ρ_{LM} . These equations are too cumbersome to solve analytically, but

$$\frac{d}{dt} \rho_{10} + \frac{1}{\tau_1} \rho_{10} + \frac{i\omega_1}{\sqrt{2}} (e^{-i\omega_0 t} \rho_{11} + e^{i\omega_0 t} \rho_{1-1}) = \frac{1}{\tau_1} R_{10}$$

$$\frac{d}{dt} \rho_{11} + \frac{i\omega_1}{\sqrt{2}} e^{i\omega_a t} \rho_{10} + (-i\omega_0 + \frac{1}{\tau_1}) \rho_{11} - i\omega_Q \sqrt{3/5} \rho_{21} = 0$$

$$\frac{d}{dt} \rho_{20} + \frac{1}{\tau_2} \rho_{20} + i\omega_1 \sqrt{3/2} (e^{-i\omega_a t} \rho_{21} + e^{i\omega_a t} \rho_{2-1}) = \frac{1}{\tau_2} R_{20}$$

$$\begin{aligned} \frac{d}{dt} \rho_{21} + i\omega_1 \sqrt{3/2} e^{i\omega_a t} \rho_{20} - i\omega_Q \sqrt{3/5} \rho_{11} + (-i\omega_0 + \frac{1}{\tau_2}) \rho_{21} + i\omega_1 e^{-i\omega_0 t} \rho_{22} \\ - i\omega_Q \sqrt{2/5} \rho_{31} = 0 \end{aligned}$$

$$\frac{d}{dt} \rho_{22} + i\omega_1 e^{i\omega_a t} \rho_{21} + (-2i\omega_0 + \frac{1}{\tau_2}) \rho_{22} - i\omega_Q \rho_{32} = 0$$

$$\frac{d}{dt} \rho_{30} + \frac{1}{\tau_3} \rho_{30} + i\omega_1 \sqrt{3} (e^{-i\omega_a t} \rho_{31} + e^{i\omega_a t} \rho_{3-1}) = \frac{1}{\tau_3} R_{30}$$

$$\frac{d}{dt} \rho_{31} + i\omega_1 \sqrt{3} e^{i\omega_a t} \rho_{30} - i\omega_Q \sqrt{2/5} \rho_{21} + (-i\omega_0 + \frac{1}{\tau_3}) \rho_{31} - i\omega_1 \sqrt{5/2} e^{-i\omega_0 t} \rho_{32} = 0$$

$$\frac{d}{dt} \rho_{32} - i\omega_Q \rho_{22} + i\omega_1 \sqrt{5/2} e^{i\omega_a t} \rho_{31} + (-2i\omega_0 + \frac{1}{\tau_3}) \rho_{32} + i\omega_1 \sqrt{3/2} e^{-i\omega_a t} \rho_{33} = 0$$

$$\frac{d}{dt} \rho_{33} + i\omega_1 \sqrt{3/2} e^{i\omega_a t} \rho_{32} + (-3i\omega_0 + \frac{1}{\tau_3}) \rho_{33} = 0$$

To get equations for $\frac{d}{dt} \rho_{L-M}$, take the equation for $\frac{d}{dt} \rho_{LM}$ and set $M \rightarrow -M$, $\omega_0 \rightarrow -\omega_0$, $\omega_a \rightarrow -\omega_a$, $\omega_Q \rightarrow -\omega_Q$, but $\omega_1 \rightarrow \omega_1$.

FIGURE 21 - Coupled Differential Equations

numerical solutions can be obtained easily using a digital computer. This was done for various values of ω_1 , ω_a , R_{LM} , and $\Delta\omega$, where $\Delta\omega = \omega_a - \omega_0$.

Before solving these equations, several items should be noted:

1. The quadrupole perturbation is the only coupling between states of different L. Therefore the orientation and alignment moments do not affect one another when ω_Q is zero.
2. The transverse H_1 magnetic field is the only coupling between states of different M. In the absence of such a field, the longitudinal and transverse moments are independent.

In many experiments, the NMR signals are obtained by using the Faraday readout signal to drive the transverse H_1 magnetic field.

A phase difference $\Delta\phi$ between the signal and H_1 , caused, for instance, by the electronics which drives H_1 , would cause a change in the frequency of the signal. Examination of the numerical solutions of the simultaneous equations indicates that $\Delta\omega$ and $\Delta\phi$ are related approximately by

$$\Delta\omega \approx A(\omega_1)R_{20}\omega_Q (1 + B(\omega_1)\omega_Q^2) - \Delta\phi(C + D(\omega_1)\omega_Q^2 + E(\omega_1)\omega_Q^4), \quad (31)$$

where the coefficients A through E are positive and are functions of ω_1 , as well as of τ_1 , τ_2 , τ_3 , and R_{10} . Several features of this relation can be noted:

1. For $\omega_Q = 0$, equation (31) reduces to

$$\Delta\omega = -C\Delta\phi.$$

This result is also predicted by modelling the ^{201}Hg spin

system and the H_1 drive as a resonator in a feedback loop. One would expect that the constant C is inversely proportional to the relaxation time τ , of the resonator.

2. For $R_{20} = 0$, the first term is zero, but there is still a dependence of $\Delta\omega$ upon ω_Q . Also, examination of the numerical solutions for ρ_{11} and ρ_{21} shows that the quadrupole perturbation produces a transverse alignment moment even if no longitudinal alignment moment is being produced by the optical pumping. At resonance ($\Delta\omega = 0$), the transverse alignment moment produced by the quadrupole perturbation is 90° out of phase with the transverse moment produced by alignment pumping.
3. For $\Delta\phi = 0$, the frequency change is proportional to the product of the alignment pumping rate and the quadrupole perturbation, when the perturbation is weak. The numerical solutions for $R_{10} = 0$ (no orientation pumping) show that the quadrupole perturbation again mixes the transverse orientation and alignment moments, and produces a transverse orientation moment which is 90° out of phase with the transverse moment produced by the orientation pumping. When the orientation pumping is not zero, these two transverse orientations moments add, yielding a net orientation moment which is out of phase with H_1 . This phase difference between H_1 and the Faraday readout signal causes a frequency shift $\Delta\omega$ in the same way that a phase shift in the electronics of the feedback loop causes a frequency shift.
4. No numerical solutions have been found for which $\Delta\omega$ is independent of ω_1 , unless ω_Q is zero or unless both R_{20} and $\Delta\phi$ are zero. This fact confirms that the response of the NMR cell to a change in H_1 amplitude is a valid check for the presence of a nonzero quadrupole perturbation.

Although the calculations described in this section do not deal directly with the relaxation of the nuclear spins on the wall, they show that a steady-state quadrupole perturbation, which can be caused by interactions between the nuclear spin and the wall, can affect the steady-state distribution of the nuclear spins.

6.4 RELAXATION DUE TO A FLUCTUATING ANISOTROPIC PERTURBATION

The relaxation of a nonthermal distribution of spins has been calculated by several authors,³⁰ but all of those calculations assumed an isotropic relaxing potential. Recent vapor-phase NMR relaxation measurements in containers of various shapes have shown the need for a theoretical treatment of relaxation caused by a potential with a fixed orientation with respect to the static magnetic field used in such experiments. Explicit expressions describing the time dependence of a ^{201}Hg system in the presence of dipole and quadrupole perturbations were derived and applied to the quadrupole relaxation of oriented vapor-phase ^{201}Hg atoms which are repeatedly adsorbed onto the walls of containers of various shapes. Predictions of the theory for a cube-shaped container indicated that although the contributions of the quadrupole perturbation to the relaxation due to the individual faces of the container vary with surface orientation, the sum of the contributions is independent of the orientation of the container. This was verified experimentally and the results were published.³¹ (See Section 9.3) The theory has been applied explicitly to a few geometrical shapes and predicted that certain of these shapes will have several characteristics in common, including the insensitivity to rotation mentioned above for the cube. These results are summarized in Table 4.

The experimental verification of these theoretical efforts using a cubic cell indicates that progress has been made toward understanding the nature and the specific details of the quadrupole interaction between ^{201}Hg and the walls of NMR cells.

TABLE 4 - Characteristics of Certain Cell Geometries

Cell Shape	Common Characteristics
1. sphere	1. Zero average shift in the energy levels of the spin system
2. cube	2. Longitudinal and transverse relaxation rates are equal and independent of cell orientation
3. tetrahedron	3. The relaxation rates are proportional to $4A/3$, where A is the surface area of the container.
4. bi-cone with half-angle = $\sin^{-1}(3^{-1/2})$	
5. right circular cylinder with length = diameter	

7. CONCLUSIONS

Relaxation measurements have indicated that ground state mercury atoms interact with a fused silica surface primarily through a weak van der Waals force. This force seems to be characteristic of the surface in general, rather than originating from specific sticking sites on the surface. The activation energy associated with this interaction, .22-.24 eV, is the same for several different wall materials with different relaxation characteristics. These measurements also indicate that the concentration and/or strength of paramagnetic centers on fused silica surfaces tends to increase with increasing temperature, while doing the reverse on the surface of Corning 9741 glass. The fact that the fused silica with the highest purity produces NMR cells with the longest τ_{201} and greatest stability indicates that the mercury in these cells is interacting directly with the fused silica surface, rather than with a layer of surface contamination.

The great variability and strong relaxation interactions that are characteristic of NMR cells before they have been subjected to high temperature heat treatments can have several causes. In fact there may be several processes occurring simultaneously in the cells. The nature of these processes and the role of the high temperature (900 °C) heat treatments in stabilizing the cells are not clear at this time. The relaxation data does show that the density or strength of paramagnetic centers and of sites that cause quadrupole relaxation diminish during the sequence of heat treatments. The cell wall usually becomes less changeable during the series of heat treatments; while the activation energy can become independent of temperature, the concentration of paramagnetic centers continues to vary with temperature, although in a reproducible manner.

The transmittance measurements on NMR cells have shown that large variations in mercury vapor density can occur. These variations usually diminish as the cells receive a series of heat treatments.

Since the mercury vapor density is affected by the resonance radiation of the pump lamp, it is proposed that excited mercury atoms, carrying 4.89 eV of energy above the ground state are interacting with the wall.

Other surface analysis techniques, such as SEM and XPS, which have the capability of providing more detailed information about the surface, have been used to examine the surfaces of NMR cells, but have not had sufficient sensitivity to detect any surface characteristics which might be associated with the mercury-wall interactions.

No interaction between mercury vapor and silica powder was detected in experiments that monitored the infrared absorption characteristics of the silica and the resonance radiation absorption of the mercury vapor. These experiments permitted calculation of an upper limit to the amount of adsorption of mercury vapor by the silica which was in general agreement with the results of the relaxation measurements. Predictions of a new theoretical analysis of the quadrupole perturbation of the energy levels of ^{201}Hg were confirmed by experiment and have led to a further understanding of the nature of the quadrupole interaction between ^{201}Hg and the cell wall.

8. REFERENCES

1. D.S. Bayley, I.A. Greenwood, and J.H. Simpson, Final Report on Contract No. F44620-72-C-0047, August 1976, KD-76-31.
2. B. Cagnac, "Orientation Nucleaire par Pompage Optique des Isotopes Impairs du Mercure," Doctoral Thesis, Universite de Paris, December 1960.
3. D.I. Shernoff, Rev. Sci. Instr. 40, 1418 (1969).
4. R.H. Doremus, Physics Chem. Glasses, 10, 28 (1969).
5. S.V. King, Nature 213, 1112 (1967).
6. V.J. Fratello, J.F. Hays, F. Spaepen, and D. Turnbull, J. Appl. Phys. 51, 6160 (1980).
7. M.L. Hair, J. Non-Crystalline Solids 19, 299 (1975).
8. V.J. Fratello, J.F. Hays, and D. Turnbull, J. Appl. Phys. 51, 4718 (1980).
9. F.J. Norton, J. Am. Ceramic Soc. 36, 90 (1953).
10. V.O. Altemose, J. Appl. Phys. 32, 1309 (1961).
11. L.E. Halliburton, (1980) (Private Communication).
12. R.N. Brown and A. Kahan, J. Phys. Chem. Solids 36, 467 (1975).
13. E.A. Irene, in "The Physics of SiO₂ and Its Interfaces," S. Pantelides, ed., Pergamon Press, New York (1978), p.205.
14. A. Abragam, "Principles of Nuclear Magnetism," Oxford (1961).
15. A.M. Bonnot and B. Cagnac, C.R. Acad. Sc., Paris, 274, 947 (1972).
16. M.A. Bouchiat and M. Brossel, Phys. Rev. 147, 41 (1966).
17. V.P. Putyrskii and T.G. Izyumova, Opt. Spektrok 37, 227 (1974).
18. J.H. deBoer, "The Dynamical Character of Adsorption," Oxford University Press (1968), p.34.
19. G. Moruzzi, M. Inguscio, F. Strumia, and P. Violino, Phys. Rev. 8A, 51 (1973).

20. C. Cohen-Tannoudji, J. de Phys., 24, 653 (1963).
21. V.P. Putyrskii, Opt. Spectrosc. 35, 593 (1973).
22. J.H. Simpson and R. Patterson, Final Report on Rate Bias Stability Investigations, August 1978, Contract No. N00019-77-C-0447.
23. M.L. Hair, Infrared Spectroscopy in Surface Chemistry, Marcel Dekker, New York, (1967), Chapter 4.
24. R. Liebich and P. Fink, Z. fur Chemie 11, 34 (1971).
25. P.A. Heimann and J.H. Simpson, Appl. Phys. Lett. 36, 963, (1980).
26. W. Happer, private communication.
27. G.H. Fuller and V.W. Cohen, Nucl.Data A5, 6 (1968), as cited in chapter 8b of American Institute of Physics Handbook, 3rd ed., D.E. Gray, ed., (McGraw-Hill Inc., New York, 1977).
28. J.H. Simpson, Bull.Am.Phys.Soc. 23, 394 (1978).
29. P.A. Heimann, Phys. Rev. A23, 1204 (1981).
30. W. Happer, Rev. Mod. Phys. 44, 169 (1972). See Table II, p.197 for a list of work on various relaxation mechanisms.
31. P.A. Heimann, I.A. Greenwood, and J.H. Simpson, Phys. Rev. A23, 1209 (1981).

9. PUBLICATIONS

- 9.1 Analysis of the dark film in rf-excited mercury lamps.
- 9.2 Quadrupole perturbation effects upon the ^{201}Hg magnetic resonance. I. Effects upon free precession of the nuclear spins.
- 9.3 Quadrupole perturbation effects upon the ^{201}Hg magnetic resonance. II. Relaxation due to an anisotropic perturbation.

Quadrupole perturbation effects upon the ^{201}Hg magnetic resonance. II. Relaxation due to an anisotropic perturbation

P. A. Heimann,* I. A. Greenwood, and J. H. Simpson
The Singer Company, Kearfott Division, Little Falls, New Jersey 07424
 (Received 13 October 1980)

The theory of relaxation of a weakly perturbed spin system is extended to the case of a nonisotropic perturbation. The calculation follows the method of Happer who uses spherical basis operators. Explicit expressions are derived for a spin-3/2 system in the presence of dipole and quadrupole perturbations. The results are then applied to the quadrupole relaxation of oriented vapor-phase atoms which occurs while these atoms are adsorbed onto the walls of containers of various shapes. Although the relaxation rates due to the cell wall depend upon the orientation of the wall with respect to the externally applied magnetic field, it is found that the sum of the contributions to the relaxation due to the six faces of a cube-shaped container is independent of the orientation of the container. This prediction is verified experimentally.

I. INTRODUCTION

The relaxation of a nonthermal distribution of spins has been calculated by several authors,¹ but all of those calculations assume an isotropic-relaxing perturbation. Recent vapor-phase NMR relaxation measurements in containers of various shapes have shown the need for a theoretical treatment of relaxation caused by an anisotropic-relaxing perturbation with a fixed orientation with respect to the static magnetic field used in such experiments. The first section of this paper extends one of the more general calculations in the literature² to the case of an anisotropic-relaxation mechanism. The second section deals with the specific example of a spin-3/2 atom relaxing due to an electric-field gradient and gives explicit expressions for relaxation of spin-3/2 atoms due to electric-field gradients on the walls of a cube-shaped cell at various orientations. The last section describes experimental results obtained using such a cube-shaped cell, and compares the results to the theoretical predictions. Good agreement is found.

The reader should keep in mind that only the relaxation due to an anisotropic-relaxing perturbation is calculated here. The relaxation rates due to isotropic mechanisms must be added to the rates predicted here in order to arrive at an estimate of the experimentally observed relaxation rates.

II. THEORY

This calculation follows the method of Happer,³ who expresses the interaction-picture density matrix σ and the relaxing perturbation V in terms of spherical basis operators $T_{L,M}$ (Ref. 3):

$$\sigma = \sum_{L,M} (-1)^M \sigma_{L,M} T_{L,M}, \quad (1)$$

$$V(t) = \sum_m (-1)^m V_{L,-m}(t) T_{L,m}, \quad (2)$$

with

$$T_{L,M} = \sum_{\mu} |\mu\rangle \langle \mu - M| (-1)^{\mu - M} C(KKL; \mu, M - \mu). \quad (3)$$

In Eq. (3), the states $|\mu\rangle$ have a total spin K and a component m along the z axis (which is assumed to be the quantization direction). $C(KKL; \mu, M - \mu)$ is a Clebsch-Gordan coefficient and is defined with the phase conventions of Rose.⁴ In Eq. (2), l is the multipolarity of the potential V . For instance, a magnetic-dipole interaction has $l=1$, and an electric-quadrupole interaction has $l=2$. This paper deals mainly with the case $l=2$, $K=3/2$, which corresponds to a ^{201}Hg nucleus experiencing an electric-quadrupole perturbation. It follows from the definition of $\sigma_{L,M}$ and $T_{L,M}$ that σ_{10} is related to the longitudinal-orientation moment, σ_{11} to the transverse-orientation moment, σ_{20} to the longitudinal-alignment moment, and σ_{21} to the transverse-alignment moment precessing at the Larmor frequency.

Happer assumes that V is isotropic and that it has an exponential correlation function:

$$\langle V_{Lm}(t) V_{Lm}(t - \tau) \rangle_{av} = \left(\frac{1}{2l+1} \right) \delta_{m,-m} (-1)^m V^2 e^{-|\tau|/\tau_c}, \quad (4)$$

where V^2 is the mean-squared strength of the perturbation, τ_c is the correlation time, and the symbol $\langle \rangle_{av}$ denotes an ensemble average. The general formula for the time dependence of the density-matrix σ , based upon second-order perturbation theory is stated in Ref. 2 as

$$\frac{d\sigma}{dt} = - \left\langle \int_0^\infty [V^*(t), [V^*(t - \tau), \sigma(t)]] d\tau \right\rangle_{av}. \quad (5)$$

where $V^*(t)$ is the potential in the interaction picture,

$$V^*(t) = e^{(i/\hbar)H_0 t} V(t) e^{-(i/\hbar)H_0 t}, \quad (6)$$

for the unperturbed Hamiltonian H_0 . Happer then shows that the time dependence of the density matrix due to relaxation can be expressed as a set of equations

$$\frac{d}{dt} \sigma_{L,M} = \sum_{L'} R_{LL'}(M) \sigma_{L',M}, \quad (7)$$

where

$$L' = L, L \pm 2, \dots, L \pm (2l - 2).$$

The fact that the relaxation couples only those elements of the density matrix with equal values of M is a consequence of axial symmetry as expressed by the $\delta_{m,-m}$ term in Eq. (4).

If we assume that V is no longer isotropic but has cylindrical symmetry about some axis, then Eq. (4) must be modified slightly. The term V^2 is replaced by a term V_{lm}^2 , dependent on l and m ,

$$\langle V_{lm}(t) V_{lm}(t - \tau) \rangle_{av} = \frac{1}{2l+1} \delta_{m,-m} (-1)^m V_{lm}^2 e^{-\tau/\tau_c}. \quad (8)$$

The terms V_{lm}^2 are the mean-squared values of $V_{lm}(t)$ defined in Eq. (2). Also, note that

$$\sum_m V_{lm}^2 = V^2. \quad (9)$$

$$R_{LL'}(M) = -\tau_c [1 + (-1)^{L+L'}] \sum_{\mu} [1 - (-1)^{L+L'+\mu}] (2\lambda+1) W(l\lambda K; LK) W(l\lambda K; L'K) \times \sum_{\mu} \frac{V_{lm}^2 C(l\lambda L; \mu, M - \mu) C(l\lambda L'; \mu, M - \mu)}{1 + i\omega\mu\tau_c}. \quad (10)$$

Equation (10) is identical to Eq. (24) of Ref. 2 except that V^2 is replaced by V_{lm}^2 , which must then be brought inside the summation over μ .

III. RELAXATION DUE TO AN ELECTRIC-FIELD GRADIENT

A. Expressions for the perturbation and for the relaxation rates

We now evaluate Eq. (10) for the special case of $K = 3/2$ and $l = 2$, which corresponds to ^{201}Hg in the presence of an electric-field gradient. The energy operator for a particle with a total spin I and with a quadrupole moment eQ (e is the elementary charge), within a cylindrically symmetric free-space electric field with a gradient q along the field symmetry axis, is given by⁷

where V^2 is defined for Eq. (4).

The term $\delta_{m,-m}$ is a consequence of the assumed axial symmetry of the potential.⁵ It will be shown that if this term were not present, then the randomly fluctuating perturbation V would be able to couple density-matrix elements of different m , which is not physically reasonable. For instance, if σ_{10} and σ_{11} were coupled, then V would be able to transform a longitudinal orientation distribution into a coherently-precessing transverse-orientation distribution. Such a transformation can only be made by a nonrandom perturbation, such as a transverse-rf magnetic field near the Larmor frequency.

In the special case for $l = 2$, Cohen-Tannoudji⁶ expresses V in terms of spherical harmonics. In this case, the $\delta_{m,-m}$ term follows from integration over the azimuthal angle ϕ . Such integration is necessary, even if the symmetry axis of the quadrupole potential has a fixed angle θ with respect to the quantization direction, since this random potential interacts with the spins at random intervals during their Larmor precession, which corresponds to random values of ϕ . Cohen-Tannoudji then integrates over the polar angle θ , since his calculation assumes an isotropic perturbation.

With the correlation function of Eq. (8), the time dependence of the density matrix can still be expressed in the form of Eq. (7), with the coefficients $R_{LL'}(M)$ given by

$$V_{op} = \frac{e^2 q Q}{4I(2I+1)} [3I_z^2 \cos^2 \theta + 3I_x^2 \sin^2 \theta + 3(I_x I_z + I_z I_x) \sin \theta \cos \theta - I^2], \quad (11)$$

where θ is the angle between the symmetry axes of the quadrupole and of the electric field, and I_x , I_y , and I^2 are spin angular-momentum operators. It is easy to show that (11) is equivalent to

$$V_{op} = \frac{e^2 q Q}{4I(2I+1)} \left[\frac{1}{2} (3 \cos^2 \theta - 1) (3I_z^2 - I^2) + (3 \sin \theta \cos \theta) (I_x I_z + I_z I_x) + \frac{1}{2} (3 \sin^2 \theta) (I_x^2 - I_y^2) \right]. \quad (12)$$

Using the definition of the spherical basis operators, and defining $V_0 = e^2 q Q / 4I(2I - 1)$, we can show that

$$V_{op} = \sum_{m=-2}^2 (-1)^m V_{2,-m} T_{2,m}, \quad (13)$$

with

$$V_{2,0} = 6V_0 \left[\frac{1}{2}(3 \cos^2 \theta - 1) \right] = 6V_0 P_2(\cos \theta), \quad (14a)$$

$$V_{2,\pm 1} = \sqrt{6} V_0 (3 \sin \theta \cos \theta) = \sqrt{6} V_0 P_2^1(\cos \theta), \quad (14b)$$

and

$$V_{2,\pm 2} = (\sqrt{6}/2) V_0 (3 \sin^2 \theta) = (\sqrt{6}/2) V_0 P_2^2(\cos \theta). \quad (14c)$$

The terms $P_2(\cos \theta)$ and $P_2^m(\cos \theta)$ are Legendre and Legendre associated functions of the first kind. Note that V_{20} corresponds to the shift in magnetic energy levels of the spin system, and that $V_{2,\pm 1}$ corresponds to a torque on the spins due to the electric-field gradient.

We substitute Eqs. (13) and (14) into Eqs. (10) and, assuming that $\omega \tau_c \ll 1$ and that σ_{30} and σ_{31} are negligible compared to σ_{10} and σ_{11} , we find that

$$\frac{d}{dt} \sigma_{10} = -R_0 \tau_c V_0^2 (2 - 2 \cos^2 \theta) \sigma_{10}, \quad (15a)$$

and

$$\frac{d}{dt} \sigma_{11} = -R_0 \tau_c V_0^2 (1 + \cos^2 \theta) \sigma_{11}, \quad (15b)$$

where the constant R_0 is equal to $54/25$, and where θ is now the angle between the electric-field symmetry axis and the quantization direction. The latter is determined by the static magnetic field in magnetic-resonance experiments.

Equations (15) make some strange predictions. For instance, at $\theta = 90^\circ$ they predict that the longitudinal-spin distribution relaxes twice as fast as the transverse distribution. This is not in agreement with magnetic-resonance relaxation-time measurements, where the transverse-relaxation rate $1/T_2$ is always faster than or equal to the longitudinal rate $1/T_1$. However, the above calculation does not consider isotropic mechanisms which can considerably increase the actual transverse-relaxation rate.

B. Relaxation on the walls of a container

The relaxation of spins of vapor-phase atoms occurs mainly on the wall of the container or cell.⁹ Each portion of the wall makes a fixed angle with respect to the static magnetic field H_0 , and therefore the relaxation rate due to an electric-field gradient can be calculated by summing or integrating the angle-dependent relaxation rates [Eqs. (15a) and (15b)] over the cell surface. An

electric field with a gradient component directed perpendicular to the cell wall is always associated with adsorption on the wall. Therefore, we let θ in Eqs. (15) represent the angle between H_0 and the normal to the cell surface. For a spherical container, the relaxation rate is obviously independent of cell orientation. For a cube-shaped cell, we must sum the relaxation rates due to the six cube faces.

For all cube orientations in which a face diagonal (dotted line in Fig. 1) is perpendicular to H_0 and in which the normal to that face (and to the opposite face) makes an angle β with the H_0 direction, it can be shown⁹ that the normals to the other two faces make an angle β' with H_0 direction, with

$$\cos \beta' = -2^{-1/2} \sin \beta. \quad (16)$$

Therefore, the longitudinal-relaxation rate due to all six cube faces is given by

$$\begin{aligned} \frac{1}{\sigma_{10}} \frac{d}{dt} \sigma_{10} &= -R_0 \tau_c V_0^2 \{ 2(2 - 2 \cos^2 \beta) \\ &\quad + 4[2 - 2(-2^{-1/2} \sin \beta)^2] \} \\ &= -8R_0 \tau_c V_0^2, \end{aligned} \quad (17)$$

and the transverse-relaxation rate is given by

$$\begin{aligned} \frac{1}{\sigma_{11}} \frac{d}{dt} \sigma_{11} &= -R_0 \tau_c V_0^2 \{ 2(1 + \cos^2 \beta) \\ &\quad + 4[1 + (-2^{-1/2} \sin \beta)^2] \} \\ &= -8R_0 \tau_c V_0^2. \end{aligned} \quad (18)$$

We therefore have the result for a cube-shaped cell that the longitudinal and transverse rates are equal and are independent of cell orientation, despite the fact that the longitudinal and transverse contributions from different cube faces in

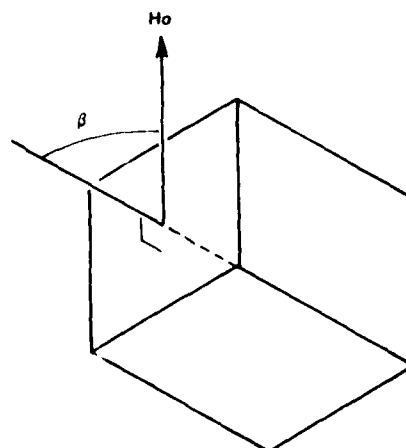


FIG. 1. Cube-shaped cell in a magnetic field H_0 .

general are different and are functions of orientation with respect to the external magnetic field.

IV. EXPERIMENTAL

A. Method

Measurements of longitudinal and transverse relaxation rates were made using a cube-shaped cell. The fused-silica cube, approximately 1 cm on a side, was evacuated and then filled with a dry vapor of mercury enriched with the isotopes ^{199}Hg and ^{201}Hg at a density of about 10^{12} atoms/cm 3 . The cell did not contain a buffer gas.

The transverse orientation moment was detected by means of the transverse rf Faraday effect using the apparatus shown in Fig. 2. The angle of linear polarization of 253.7-nm light from a ^{202}Hg readout lamp is modulated at the Larmor frequency by the precession of the transverse-magnetic moment. This modulation in angle can be converted to a modulation in amplitude, using a linear analyzer. The light from a ^{202}Hg lamp is slightly off resonance with the ^{199}Hg and ^{201}Hg absorptions, and is therefore suitable for this type of readout. Optical pumping was accomplished with circularly polarized 253.7-nm light from a ^{204}Hg lamp. Such light is absorbed efficiently¹⁰ by hyperfine components of both ^{199}Hg and ^{201}Hg . The cell was heated to 300°C in a hot-air oven at the center of a pair of shielded Helmholtz coils. The Helmholtz coils produced a magnetic field of about 3.5 G for measurements on ^{201}Hg , corresponding to a Larmor frequency of 975 Hz.

Relaxation rates were determined using modified pulsed NMR techniques.¹¹ At the start of each measurement, both shutters were closed and no current was applied to the ac coils. A longitudinal moment was established by opening the pump-beam shutter for 60 seconds, which is about ten times

longer than the pumping time. The pumping time is the time required to orient a fraction $1/e$ of the atoms, assuming no relaxation. For measurement of the longitudinal relaxation rate $1/T_1$, the pump shutter was closed, and, after a measured delay, the readout shutter was opened simultaneously with the application of a short pulse through the ac coils. This pulse was controlled by the switching circuit and was adjusted such that the longitudinal moment was rotated by 90° , making it observable with Faraday readout. The resulting amplitude was recorded on a X-Y recorder for various values of the delay time. The amplitude (after the pulse) versus the delay time was fitted using a least-squares method to an exponential function in order to determine the relaxation rate, or its inverse, the relaxation time. For measurement of the transverse relaxation rate $1/T_2$, the pulse was applied when the pump-beam shutter was closed, so that a transverse distribution existed during the measured delay time, after which the readout shutter was opened and the signal was observed. Note that the readout and pump light could not affect the measured relaxation rates, since all relaxation took place with both beams off.

It is important to check for the presence of non-exponential decay when analyzing the results of this experiment.¹² Such departure from exponential decay can occur if V_{20} , the shift in the magnetic energy levels due to the quadrupole perturbation, does not average to zero over the entire cell surface. It can be shown that this average, $\langle V_{20} \rangle$, is zero over the surface of a cube for all orientations with respect to the H_0 magnetic field. A nonzero average can be caused by the presence of the cell sealoff tip (a major source of this effect in spherical cells) or by a slight elongation of the cell causing a departure from a cubic shape (the cell walls were not flat enough to verify any elongation). It can be shown that either of these two effects will result in a value of $\langle V_{20} \rangle$ which has the same angular dependence as V_{20} , itself,

$$\langle V_{20} \rangle \propto P_2(\cos\theta) = \frac{1}{2}(3\cos^2\theta - 1), \quad (19)$$

where θ is now the angle between H_0 and an axis whose orientation with respect to the cell depends upon the cell shape. The functional form of the decay transient for transverse relaxation can be shown to be

$$S(t) = S(0)e^{-t/T} \left(\frac{2 + 3\cos\omega_Q t}{5} \right), \quad (20)$$

where $S(t)$ is the signal at time t , T is the relaxation time, and ω_Q is proportional to $\langle V_{20} \rangle$. Longitudinal decay transients are unaffected by a non-

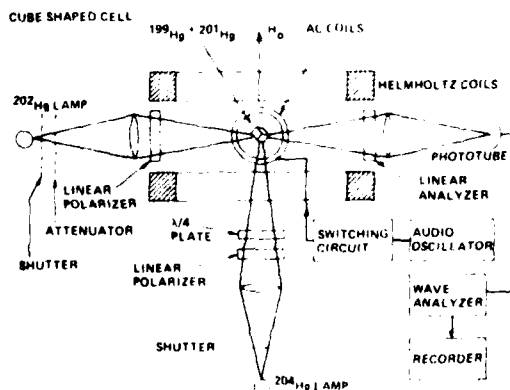


FIG. 2. Experimental apparatus.

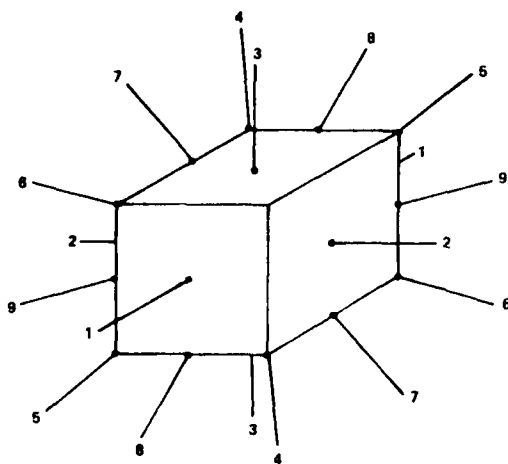


FIG. 3. Axes of orientation of magnetic field with respect to cube-shaped cell.

zero $\langle V_{20} \rangle$.

It is important to verify that the observed relaxation is due, at least in part, to electric-field gradients. Another significant relaxation mechanism is relaxation by fluctuating local magnetic fields on the surface. Since such magnetic fields do not have a preferred direction relative to the cell wall surface, this relaxation mechanism is isotropic. Its strength is proportional to the square of the gyromagnetic ratio γ of the atom.¹³ If this were the only mechanism present, then ^{199}Hg would relax about seven times as fast as ^{201}Hg , since $(\gamma_{199}/\gamma_{201})^2 = 7.338\,725$.¹⁴ The fact that ^{199}Hg was observed to relax more slowly than ^{201}Hg confirms that the latter was being affected by electric-field gradients as well as by local magnetic fields.

B. Results

Measurements of longitudinal and transverse relaxation rates, $1/T_1$ and $1/T_2$, were made for a cube-shaped cell in several orientations. Specifically, measurements were made along the three equivalent $\theta = 0^\circ$ axes, three of the four equivalent $\theta = 55^\circ$ axes, and three of the six equivalent $\theta = 90^\circ$ axes, identified by numbers in Fig. 3. Their orientations, in spherical coordinates with the z axis along axis No. 3, are listed in Table I. The term "equivalent axes" refers to the fact that a given value of θ can be obtained with respect to different cube faces. For instance, the $\theta = 55^\circ$ axis can be obtained by aligning H_0 along any of the four cube body diagonals. The individual cube faces

TABLE I. Values of ω_Q [see Eqs. (19) and (20)] for various orientations of the cube-shaped cell.

Axis (see Fig. 3)	θ	ϕ	Orientation ω_Q (sec $^{-1}$)	$P_2(\cos\theta)$
1	90	0	$(8.3 \pm 1.5) \times 10^{-3a}$	-0.5
2	90	90	14.3 ± 1.3	-0.5
3	0		21.5 ± 0.8	1.0
4	55	-135	5.1 ± 2.6^a	0.0
5	55	135	0.0 ± 0.1	0.0
6	55	45	0.0 ± 0.1	0.0
7	45	-90	5.1 ± 1.9	0.15
8	45	180	6.4 ± 3.1	0.15
9	90	-45	10.1 ± 1.6	-0.5

^a Values not reproducible from day to day.

can be identified by features such as bubbles, scratches, or the location of the sealoff tip (not shown in Fig. 3).

Longitudinal and transverse decay transients were least squares fitted to Eq. (20). All of the longitudinal decay transients yielded ω_Q equal to zero, within experimental uncertainty, and relaxation times between 40 and 44 s, showing no apparent variation with cell orientation. The transverse decay transients yielded relaxation times a few percent shorter than the corresponding longitudinal relaxation times, and values of ω_Q as shown in Table I. Note that the values of ω_Q are roughly proportional to $|P_2(\cos\theta)|$. Therefore, if we assume that the cell is elongated along axis No. 3 in Fig. 3, then the results can be explained in terms of the nonexponential decay which is predicted for cells with shapes that yield a nonzero value for $\langle V_{20} \rangle$.

V. CONCLUSIONS

The results described in this paper show that the four-level spin system of ^{201}Hg can be described conveniently in terms of spherical basis operators, and that this description can predict effects which are not predicted by the simpler but less rigorous description of ^{201}Hg as three two-level spin systems. The results also indicate that a description of a quadrupole perturbation solely in terms of the shift in energy levels, without including effects such as torques which may also be present, might not be sufficient for predicting the effects of such a perturbation. Such a simplified model would not have predicted the observed result that the relaxation rate of nuclear spins which occurs on the walls of a cube-shaped container is independent of the orientation of the container in the external magnetic field.

ACKNOWLEDGMENTS

The cube-shaped cell used in this work was fabricated by D. Shernoff, and early measurements

on this cell were performed by the late D. S. Bayley. This work was supported by the Air Force Office of Scientific Research under Contract No. F49620-76-C-0009.

*Present address: Bell Laboratories, Murray Hill, New Jersey 07974.

¹W. Happer, Rev. Mod. Phys. 44, 169 (1972); see Table II, p. 197 for a list of work on various relaxation mechanisms.

²W. Happer, Phys. Rev. B 1, 2203 (1970).

³U. Fano, Rev. Mod. Phys. 29, 74 (1957).

⁴M. E. Rose, *Elementary Theory of Angular Momentum* (Wiley, New York, 1957).

⁵Reference 1, p. 200.

⁶C. Cohen-Tannoudji, J. Phys. (Paris) 24, 653 (1963).

⁷D. P. Slichter, *Principles of Magnetic Resonance* (Harper, New York, 1963), p. 172.

⁸Reference 1, p. 201.

⁹J. H. Simpson, V. Benischek, and D. S. Bayley, Interim Progress Report, Oct. 13, 1977, prepared for AFOSR, Contract No. F49260-76C-0009, KD-77-49 (unpublished).

¹⁰B. Cagnac and J. Brosset, C. R. Acad. Sci. (Paris) 249, 77 (1959).

¹¹E. L. Hahn, Phys. Rev. 77, 297 (1950).

¹²See the first paper in this series, P. A. Heimann, *Quadrupole Effects upon the ²⁰¹Hg Magnetic Resonance I. Effects upon Free Precession of the Nuclear Spins*.

¹³Reference 1, p. 202.

¹⁴B. Cagnac, thesis, University of Paris, 1960 (unpublished). See also J. C. Lehman and R. Barbé, C. R. Acad. Sci. (Paris) 237, 3152 (1963).

Quadrupole perturbation effects upon the ^{201}Hg magnetic resonance. I. Effects upon free precession of the nuclear spins

P. A. Heimann*

The Singer Company, Kearfott Division, Little Falls, New Jersey 07424

(Received 13 October 1980)

The time dependence of free-precession signals from an ensemble of spin-3/2 atoms in the presence of a quadrupole perturbation is calculated by examining the time dependence of the density matrix which describes the ensemble. The calculations yield explicit expressions for signals obtained using either a linearly or elliptically polarized off-resonant readout light, applied to a mixture of orientation, alignment, and octupole spin distributions. The results are obtained by expressing the density matrix in terms of spherical basis operators. The theoretical predictions are in good agreement with experimental results which are characterized by "beats" in the decay transients of signals from ^{201}Hg .

I. INTRODUCTION

Nonexponential relaxation of the transverse magnetic moment of an optically pumped spin distribution has been reported^{1,2} for nuclei such as ^{201}Hg and ^{83}Kr , which have spins of $\frac{3}{2}$, but not for spin- $\frac{1}{2}$ nuclei such as ^{199}Hg or ^{129}Xe . This departure from exponential decay has been explained in terms of a quadrupole perturbation, which affects only nuclei with a spin greater than $\frac{1}{2}$. Calculations which have been reported in the past have modeled the effect of the perturbation as a splitting of the spin- $\frac{3}{2}$ resonance into three separate frequencies¹ or have calculated the effect of the perturbation in terms of a 4×4 density matrix.² Although these calculations were able to explain correctly the observed nonexponential decay, they do not directly reveal other effects of a quadrupole perturbation, such as its effect on the transverse alignment moment or on longitudinal orientation and alignment moments. This paper describes a calculation of such effects using spherical basis operators, a method which yields explicit expressions for signals observed from any transverse or longitudinal distribution. The calculation is specialized to the case of a spin- $\frac{3}{2}$ nucleus such as ^{201}Hg or ^{83}Kr .

II. THEORY

In most calculations of the effects due to perturbations, the nuclear-spin distribution is described in terms of a density matrix ρ , defined by

$$\rho = \sum_{mm'} \rho_{mm'} |m\rangle \langle m'|, \quad (1)$$

where $|m\rangle$ are basis states with a z component of angular momentum m . The density matrix has the property that the expectation value $\langle I \rangle$ of any observable I is found by multiplying the corre-

sponding operator I_{op} by ρ and taking the trace

$$\langle I \rangle = \text{Tr}(I_{op}\rho).$$

The time dependence of ρ , derived from the Schrödinger equation, is given by

$$\frac{d\rho}{dt} = -\frac{i}{\hbar} [\mathcal{H}, \rho], \quad (2)$$

and a solution for this equation is

$$\rho(t) = e^{-i\mathcal{H}t/\hbar} \rho(0) e^{i\mathcal{H}t/\hbar}, \quad (3)$$

where \mathcal{H} is the total Hamiltonian for the system.

It is possible to perform the calculation of $\rho(t)$ using the density matrix as expressed in Eq. (1), but this method leads to very complicated algebraic expressions. A much simpler method is to express the density matrix, the Hamiltonian, and the operators corresponding to observables in terms of spherical basis operators T_{LM} , defined by³

$$T_{LM} = \sum_m |m\rangle \langle m-M| (-1)^{m-M} C(KKL; m, M-m), \quad (4)$$

where K is the total spin of the atom ($K = 3/2$ for ^{201}Hg), and $C(KKL; m, M-m)$ is a Clebsch-Gordan coefficient.

The density matrix can be expressed as a linear combination of the T_{LM} 's, using the phase convention of Rose,⁴

$$\rho = \sum_{L,M} (-1)^M \rho_{L,M} T_{L,-M}. \quad (5)$$

It can be shown that the various matrix elements are proportional to the strength of the various moments of the spin distribution. For instance, ρ_{00} is proportional to the total number of spins, ρ_{10} to the longitudinal orientation moment, ρ_{11} and $\rho_{1,-1}$ to precessing transverse dipole moments, ρ_{20} to the longitudinal alignment moment, etc

AD-A107 604

SINGER CO LITTLE FALLS NJ KEARFOTT DIV

F/G 20/8

RELAXATION PHENOMENA IN OPTICALLY PUMPED MERCURY ISOTOPES. (U)

AUG 81 J H SIMPSON, P A HEIMANN, M J KELLY

F49620-76-C-0009

UNCLASSIFIED

KD-81-15

AFOSR-TR-81-0724

NL

14-2
AC
210 76/14



END
DATE
FILMED
1 82
DTIC

The terms "longitudinal" and "transverse" describe moments which are directed parallel and perpendicular, respectively, to the quantization direction, which is usually chosen as the direction of an external magnetic field H_0 . It is well known^{5,6} that the longitudinal orientation and alignment moments, ρ_{10} and ρ_{20} , can be detected optically using a light beam parallel to H_0 , and that $\text{Re}(\rho_{11})$ and $\text{Im}(\rho_{21})$ can be detected using a light beam perpendicular to H_0 . The experimental apparatus for this method is described in the next section.

The Hamiltonian \mathcal{H} can be expressed also in terms of the T_{LM} 's. If the spins are in free precession with a Larmor frequency ω_0 , and are subject to a quadrupole perturbation with an energy $\hbar\omega_Q$, then, for $K = 3/2$, the Hamiltonian is given by

$$\mathcal{H} = \hbar\omega_0(\sqrt{5} T_{10}) + \hbar\omega_Q T_{20}. \quad (6)$$

The T_{LM} 's obey the commutation relation⁷

$$\begin{aligned} [T_{LM}, T_{L'M'}] = & \sum_{L''} T_{L''M''} [(2L+1)(2L'+1)]^{1/2} \\ & \times W(LL'KK; L''K) C(LL'L''; MM') \\ & \times [(-1)^{L'+L''-1}]. \end{aligned} \quad (7)$$

This expression is not as formidable as it first might appear to be, since many of the terms in the summation over L'' are zero, and since the Racah coefficients $W(LL'KK; L''K)$ and the Clebsch-Gordan coefficients can be obtained from tables in the literature.⁸ Therefore, Eq. (7) can be used to solve Eq. (2), which leads to a set of coupled differential equations for the density-matrix elements $\rho_{LM}(t)$. These equations can be separated for different values of M .

For $M = 0$, we have

$$\frac{d}{dt} \rho_{L0} = 0, \quad L = 1, 2, 3 \quad (8)$$

which indicates that the longitudinal moments do not become time dependent in the presence of a quadrupole perturbation.

For $M = 1$, we have:

$$\frac{d}{dt} \rho_{11} = i\omega_0 \rho_{11} + i\omega_Q (3/5)^{1/2} \rho_{21}, \quad (9a)$$

$$\begin{aligned} \frac{d}{dt} \rho_{21} = & i\omega_Q (3/5)^{1/2} \rho_{11} + i\omega_0 \rho_{21} \\ & + i\omega_Q (2/5)^{1/2} \rho_{31}, \end{aligned} \quad (9b)$$

$$\frac{d}{dt} \rho_{31} = i\omega_Q (2/5)^{1/2} \rho_{21} + i\omega_0 \rho_{31}. \quad (9c)$$

These can be solved by setting

$$\begin{aligned} \rho_{L1} = & e^{i\omega_0 t} [\rho_L^0 + \rho_L^c \cos(\omega_Q t) + \rho_L^s \sin(\omega_Q t)], \\ & L = 1, 2, 3 \end{aligned} \quad (10)$$

and by applying the boundary conditions at $t = 0$:

$$\rho_{L1}(0) = \rho_L^0 + \rho_L^c, \quad L = 1, 2, 3. \quad (11)$$

The result is:

$$\begin{aligned} \rho_{11}(t) = & \frac{1}{2} [2 + 3 \cos(\omega_Q t)] \rho_{11}(0) + i(3/5)^{1/2} \sin(\omega_Q t) \rho_{21}(0) \\ & + \frac{\sqrt{6}}{5} [\cos(\omega_Q t) - 1] \rho_{31}(0), \end{aligned} \quad (12a)$$

$$\begin{aligned} \rho_{21}(t) = & i(3/5)^{1/2} \sin(\omega_Q t) \rho_{11}(0) + \cos(\omega_Q t) \rho_{21}(0) \\ & + i(2/5)^{1/2} \sin(\omega_Q t) \rho_{31}(0), \end{aligned} \quad (12b)$$

$$\begin{aligned} \rho_{31}(t) = & \frac{\sqrt{6}}{5} [\cos(\omega_Q t) - 1] \rho_{11}(0) \\ & + i(2/5)^{1/2} \sin(\omega_Q t) \rho_{21}(0) \\ & + \frac{1}{2} [3 + 2 \cos(\omega_Q t)] \rho_{31}(0). \end{aligned} \quad (12c)$$

The first term in Eq. (12a) is also predicted in Eq. (18) of Ref. 2 if the energy shift is included only to first order. This term describes fairly well the curves shown in their Fig. 9, including the apparent phase reversal which occurs when the term $2 + 3 \cos(\omega_Q t)$ becomes negative. The method used in that paper could also yield the other terms in Eqs. (12), but the calculation would be very cumbersome.

These equations do not take into account the exponential relaxation of the spin distribution due, for instance, to interactions with the walls of the container. The relaxation can be included⁹ by rewriting Eq. (2) as

$$\frac{d\rho}{dt} = -\frac{i}{\hbar} [\mathcal{H}, \rho] + \left. \frac{d\rho}{dt} \right|_{\text{relaxation}} \quad (13)$$

In many cases, each component ρ_{LM} relaxes exponentially with a relaxation time τ_L . The effect of including this relaxation in the calculation is that the terms $\rho_{LM}(0)$ are replaced by terms $\rho_{LM}(0)e^{-t/\tau_L}$, for $L = 1, 2, 3$.

In many measurements on spin distributions, the experimental parameters are adjusted such that either the transverse orientation moment or the transverse alignment moment, but not both, are detected. In the absence of a quadrupole perturbation, both types of signals are found to decay exponentially. In the presence of the perturbation, two effects are noted. Firstly, the decay transients in these experiments are no longer exponential, and they show "beats." Such beats have been observed^{1,2} when detecting the transverse orientation moment in ^{201}Hg and ^{83}Kr in the presence of a quadrupole perturbation arising from an interaction between the atomic vapor and the walls of a nonsymmetric container. Secondly, in the free precession of an initially purely orientation distribution, a transverse alignment moment signal appears, 90° out of phase with the signal which

would be detected from an initially purely alignment distribution, and vice versa for the free precession of an initially purely alignment distribution.

In Ref. 1, the orientation signals for the unperturbed system was interpreted as the sum of three orientation signals at the same frequency, arising from three two-level systems ($|\frac{1}{2}\rangle - |\frac{1}{2}\rangle$, $|\frac{1}{2}\rangle - |-\frac{1}{2}\rangle$, and $|-\frac{1}{2}\rangle - |-\frac{3}{2}\rangle$), all with the same energy difference between levels. The quadrupole perturbation then caused a slight shift in the $|\pm\frac{1}{2}\rangle$ energy levels relative to the $|\pm\frac{3}{2}\rangle$ levels, which caused the three signals to be split into three slightly different frequencies. This frequency splitting was observed as beats in the amplitude of the orientation signals.

This same picture can be used to explain the appearance of an alignment signal during free precession of an initially purely orientation distribution. Figure 1(a) shows three spins, corresponding to the three two-level systems, at

$t = 0$, when their distribution has an orientation moment along the x axis and has no alignment moment. Figure 1(b) shows these same spins at $t = N\pi/\omega_0$, where $N\pi \approx \omega_1 \gg 1$. The quadrupole perturbation has caused the spins to precess at different rates, and their distribution now has an alignment moment (along the y axis) as well as an orientation moment (along the x axis). Later, as in Fig. 1(c), the orientation moment disappears, while the alignment moment is still nonzero.

It was stated above [Eq. (8)] that the density-matrix elements corresponding to a longitudinal orientation or alignment distribution do not change in the presence of a quadrupole perturbation. Therefore, no additional time dependence is introduced. The model of three two-level systems provides a simple physical picture for this lack of change under a quadrupole perturbation. When the spins are aligned parallel to H_0 , they do not precess. Therefore there are no oscillatory signals whose frequencies can be split, and the mechanism shown in Fig. 1 does not occur.

In the absence of a quadrupole perturbation ($\omega_Q = 0$), Eqs. (12) show that the rotation of the elliptically polarized light couples only to the orientation distribution, and the ellipticity only to the alignment distribution, as mentioned in the next section. The equations also suggest that an octupole moment distribution, once established, can, in principle, be detected using optical readout of the free-spin precession in the presence of a quadrupole perturbation.

III. EXPERIMENT

The Faraday readout apparatus used for monitoring the nuclear-spin distribution is shown in Fig. 2. The mercury is contained in a 1 cm spherical fused silica cell which is evacuated and then

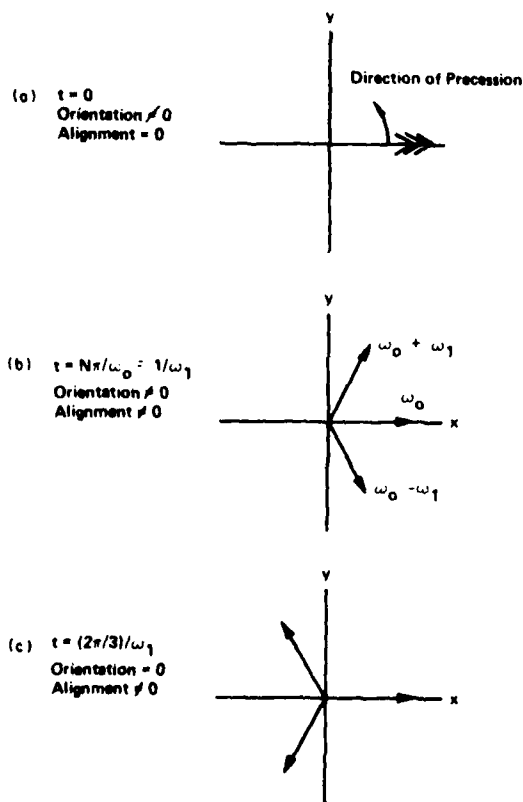


FIG. 1. Free precession of a spin- $\frac{1}{2}$ distribution described using three independent spins.

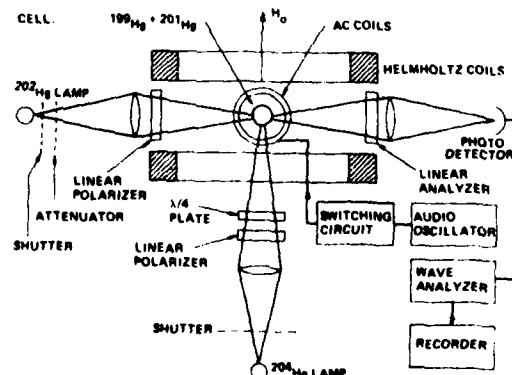


FIG. 2. Experimental arrangement.

filled with about 10^{12} atoms/cm³ of mercury vapor enriched with the isotopes ^{199}Hg and ^{201}Hg . The cell does not contain a buffer gas.

The 253.7-nm light from the ^{202}Hg readout lamp is slightly off resonance from hyperfine components of ^{199}Hg and ^{201}Hg absorptions,¹⁰ and it can be shown⁶ that if such light is directed perpendicular to the H_0 magnetic field and is elliptically polarized, then the direction of the axis of elliptical polarization is rotated through an angle proportional to $\text{Re}(\rho_{11})$, and the ellipticity of the polarization is changed by an amount proportional to $\text{Im}(\rho_{21})$. The linear analyzer in front of the phototube causes only the rotation of the polarization axis to be detected, causing a change in intensity at the phototube. A suitably oriented quarter-wave plate placed in front of the analyzer would cause only the change in ellipticity to be detected. Therefore, it is possible to monitor either ρ_{11} or ρ_{21} individually.

A longitudinal spin distribution is created by optical pumping with a ^{201}Hg lamp, whose 253.7-nm light is absorbed efficiently¹⁰ by hyperfine components of both ^{199}Hg and ^{201}Hg . If this light is linearly polarized then only an alignment distribution is established. If it is circularly polarized, then the distribution is predominantly an orientation distribution, with a small alignment moment. These longitudinal distributions are rotated by means of a transverse magnetic field at the Larmor frequency, applied through the ac coils shown in Fig. 2. In these experiments, the H_0 field was approximately 3.5 gauss for measurements on ^{201}Hg , which corresponds to a Larmor frequency of 975 Hz.

The switching circuit for the transverse magnetic field was connected to the pump-beam shutter such that the pump beam and the transverse field could be shut off simultaneously, after which the nuclear spins were in free precession, affected by only the H_0 field and the quadrupole perturbation. In these experiments, the perturbation was the result of unequal readout-light-induced frequency shifts¹¹ for the $|\pm \frac{3}{2}\rangle$ and $|\pm \frac{1}{2}\rangle$ sublevels of ^{201}Hg . Similar but weaker effects have been observed for quadrupole perturbations caused by interactions with the cell wall.^{1,2}

A typical decay curve for an orientation distribution (circularly polarized pumping light and detection of ρ_{11}) is shown in Fig. 3, along with the results of a least-squares fit to the first term in Eq. (12a). There is good agreement between theory and experiment except for the second peak (between 80 and 100 seconds). No improvement was obtained by a fit to the sum of the first and second or the sum of the first and third terms of Eq. (12a), indicating that the observed signals

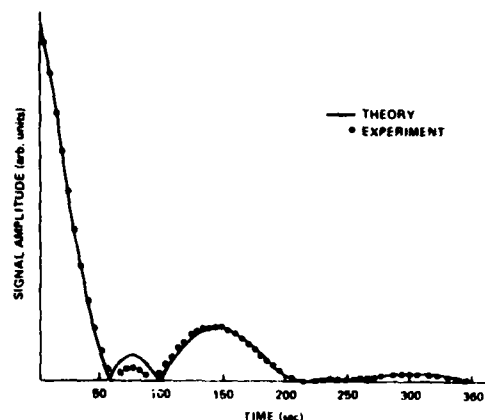


FIG. 3. Free-precession decay of a ^{201}Hg orientation distribution in the presence of a quadrupole perturbation.

were due only to an orientation distribution.

Results for an alignment distribution (linearly polarized pumping light and detection of ρ_{11}) are shown in Fig. 4. The observed nonzero signal at $t=0$ is most likely due to the presence of an orientation moment along with the alignment moment. Two possible causes for such an orientation moment are (1) optically active components in the pump beam, which result in slightly elliptically

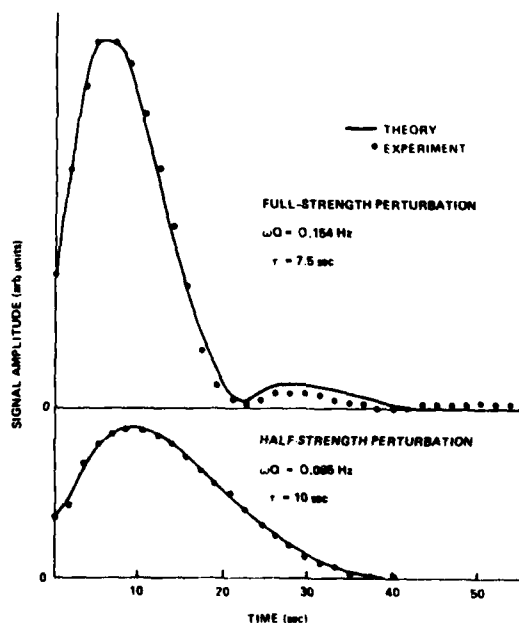


FIG. 4. Free-precession decay of a ^{201}Hg alignment distribution in the presence of a quadrupole perturbation.

polarized pumping light, and (2) the combined interaction of the transverse magnetic field (which is present until $t = 0$) and the quadrupole perturbation, which can be shown to produce a transverse orientation moment even in the presence of purely linearly polarized pumping light. The experimental data were least-squares fitted to the sum of the first and second terms in Eq. (12a), and reasonable agreement was obtained. Note that the fitted value of ω_0 in Fig. 4 is reduced by approximately one half when the readout-light-intensity, which is the source of the quadrupole perturbation, is reduced by one half, in agreement with the proportionality of the light intensity, the light-induced quadrupole perturbation, and the "beat frequency" of the decay transients.

IV. CONCLUSIONS

The calculations described above yield explicit expressions for the time dependence of a freely

precessing spin distribution in the presence of a quadrupole perturbation, and they show in a concise manner how the various transverse moments are coupled by such a perturbation. The calculations were done explicitly for a spin- $\frac{3}{2}$ system, but the method could be applied easily to other values of spin, since this value enters the calculation only through the commutation relation for the T_{LM} 's [Eq. (7)] and the coefficients in the expression for the Hamiltonian [Eq. (6)].

ACKNOWLEDGMENTS

I would like to thank J. H. Simpson and I. A. Greenwood for their encouragement and helpful discussions. Experimental data were furnished by D. Shernoff and by the late D. S. Bayley. This work was supported by the Air Force Office of Scientific Research under Contract No. F49620-76-C-0009.

*Present address: Bell Laboratories, Murray Hill, New Jersey 07974.

¹J. H. Simpson, *Bull. Am. Phys. Soc.* **23**, 394 (1978); see also Secs. 7.2 and 7.5 of D. S. Bayley, I. A. Greenwood, and J. H. Simpson, Final Scientific Report to AFOSR under Contract No. F44620-72-C-0047, 1976, KD-76-31; DTIC Report No. AD/A-033737 (unpublished).

²C. H. Volk, J. G. Mark, and B. C. Grover, *Phys. Rev. A* **20**, 2381 (1979).

³U. Fano, *Rev. Mod. Phys.* **29**, 74 (1957).

⁴M. E. Rose, *Elementary Theory of Angular Momentum* (Wiley, New York, 1957).

⁵C. Cohen-Tannoudji and F. Laloë, *J. Phys. (Paris)* **28**, 505 (1967); **28**, 722 (1967).

⁶W. Happer (private communication).

⁷W. Happer, *Phys. Rev. B* **1**, 2203 (1970).

⁸M. Rotenberg, R. Bivins, N. Metropolis, and J. K. Wooten, Jr., *The 3-j and 6-j Symbols* (MIT, Cambridge, Mass., 1959).

⁹W. Happer, *Rev. Mod. Phys.* **44**, 169 (1972).

¹⁰B. Cagnac and J. Brosse, *C. R. Acad. Sci. (Paris)* **249**, 77 (1959).

¹¹C. Cohen-Tannoudji, *Ann. Phys. (Paris)* **7**, 423 (1962); **7**, 469 (1962).

Analysis of the dark film in rf-excited mercury lamps

P. A. Heimann and J. H. Simpson

The Singer Company, Kearfott Division, Little Falls, New Jersey 07424

(Received 25 January 1980; accepted for publication 24 March 1980)

The dark film which forms in some rf-excited mercury discharge lamps has been characterized using several analytic techniques. This film is about one micron thick, and contains only mercury, silicon, oxygen, and possibly hydrogen. Several models for the physical and chemical nature of this film are presented and are compared with the experimental results. A mechanism for film growth is proposed.

PACS numbers: 81.60.Fs, 82.65.Nz, 68.55. + b

The use of sealed-off discharge lamps is common practice for generating sharp intense atomic spectra with little or no self-reversal. The usual lifetime of these lamps is limited in some cases by the growth of a dark film inside the lamp, which has been reported, for instance, in mercury discharge lamps.¹⁻³ Few systematic studies have been made to characterize the composition of the film which is observed in electrode as well as electrodeless lamps.

This letter reports the results of a study to determine the composition of the dark film in electrodeless mercury lamps made in spherical and dumbbell configurations. The spherical lamps were 1 cm in diameter, and the dumbbell lamps consisted of two 1-cm spheres connected by a capillary tube about 2 cm long with inside dimensions of 0.5×1.0 mm. The lamps were made of high-quality fused silica, evacuated, and baked at temperatures of about 1000 °C for a least 12 h at pressures of less than 10^{-7} Torr on an ion-pumped vacuum system. Residual-gas analysis during the final stages of bakeout showed the remaining gas composition to be primarily H_2 and H_2O , with a lower level of some components of the atmosphere (e.g., CO_2 , Ar, N_2). A small amount of mercury, usually enriched in one isotope, was introduced into the lamp by vacuum distillation, and 2–10 Torr of spectroscopic-grade argon was added. The lamps were then cleaned on the vacuum system by running an rf-excited discharge for a few minutes. Next, they were pumped down until the discharge was extinguished, refilled with argon, and sealed off.

The lamps were excited by 100 MHz rf through a coil wrapped around the spherical lamp or around one sphere of the dumbbell lamp. After many hours of operation (> 100 h) the dark film began to form in a pattern related to the visible parts of the discharge. Nodes and bright spots were present in the narrow portion of the dumbbell lamp and the dark film grew mainly at the nodes. Also, the film on the portion of the lamp nearest to the rf-exciting coil had a pattern which seemed to be related to the coil geometry. The film was dark gray in some areas (often those parts closest to the rf coils) and dark brown in others. It appeared to be smooth when viewed under a $30\times$ microscope. The film could be scratched by a stainless-steel razor blade, but not by a piece of copper wire, which corresponds to a Moh's hardness between 3 and 6.

A piece of a typical darkened lamp was examined under a scanning electron microscope (SEM) equipped with ener-

gy-dispersive analysis of x rays (EDAX). EDAX can determine the elemental composition of the sample and is sensitive to material in a layer about one micron below the sample surface. It can detect only elements with atomic number of 11 or more and is therefore insensitive to oxygen, carbon, hydrogen, etc. The SEM analysis revealed that the film consisted of a smooth layer about 0.5μ thick, along with rough "marshmallow puffs" of various sizes up to a few microns across, in varying concentrations on the sample surface. A micrograph taken near the edge of the sample is shown in Fig. 1. The edge of the silica piece is visible on the lower right and its inside face is exposed in the center of the picture. The smooth layer and the puffs are visible in the remainder of the micrograph. In other parts of the film, the puffs were so dense that the smooth part was not visible. Note that this film appears to peel away from the substrate, suggesting formation by deposition from the vapor. Using EDAX we found that the film, but not the substrate, contained mercury. However, the relative concentrations of mercury in the puffs and in the smooth portion of the film could not be determined reliably, owing to the sensitivity of EDAX to depths greater than the film thickness.

Other pieces of the lamp were analyzed using x-ray photoelectron spectroscopy (XPS or ESCA) to determine the

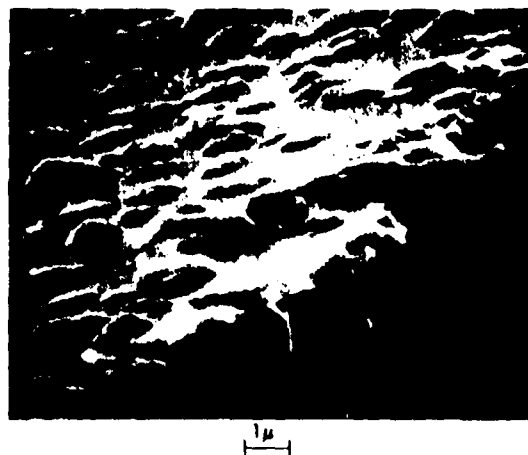


FIG. 1 SEM micrograph of film near edge of broken piece

chemical state of this film. Only silicon, oxygen, and a relatively small amount of mercury were detected by XPS, with chemical shifts corresponding to elemental mercury and to silicon and oxygen as found in fused silica. This would indicate that the film was a mixture of elemental mercury and SiO_2 . However, the x rays necessary for XPS are known to decompose mercury oxides by local surface heating.⁴ Although no time dependence was observed for the chemical shift of the mercury XPS peak, it is still possible that the film had some other chemical structure which was rapidly decomposed by x rays. A similar atomic composition was found on a region of the lamp surface where no film was visible. It is doubtful that the mercury in these clear portions was adsorbed directly from the mercury vapor in the lamp, since mercury is only weakly adsorbed onto silica.^{5,6} It is more likely that the film growth occurred to some extent over the entire lamp surface.

The film was found to be resistant to nitric and sulfuric acids, which are solvents of Hg , Hg_2O , and HgO , but it was attacked slightly by aqua regia and by NaOH , and it was attacked very quickly by a 50% HF solution. This indicates that the film is not composed solely of mercury or its oxides.

The electrical resistance of the film, measured between two points 0.5 cm apart, was greater than $2 \times 10^9 \Omega$. This can be compared with a resistance of $2 \times 10^7 \Omega$ for the 500-Å-thick carbon film used to coat the sample for SEM analysis.

Several unbroken lamps were heated to examine thermal decomposition of the film. No change was observed after heating to 250 °C for 24 h. The film began to fade when heated slowly to 380 °C, and continued to fade as the temperature was raised to 500 °C. No sudden change in film thickness was observed.

In summary, the film was fairly hard, electrically insulating, and about 0.5 μ thick. It contained only mercury, silicon, oxygen, and possibly hydrogen (not observable with EDAX or XPS). It was attacked very slightly by aqua regia, more so by NaOH , and almost instantaneously by HF , but it resisted acids which are known to attack mercury and its oxides. It decomposed at a temperature above 380 °C.

The tests described above indicate that the film is not composed solely of elemental mercury or of its oxides. It is doubtful that impurities play a major role in film growth, since impurity levels monitored during lamp filling were observed to be very low, and since no residual impurities were found in the film by EDAX and by XPS. A possible chemical composition for the film is a mercury silicate. Although zinc and cadmium, which are directly above mercury in the periodic table, form silicates which have high melting points and are stable in most acids,⁷ no detailed descriptions of a mercury silicate or of its preparation have been found in the literature.⁷⁻¹⁰ In fact, Röpke and Eysel¹⁰ reported that they were unable to synthesize Hg_2SiO_4 from HgO and SiO_2 at elevated temperature and pressure. Therefore it is possible but un-

likely that the film is composed of a mercury silicate. More likely compositions are a mixture of elemental mercury with SiO_2 , and a mixture of mercury oxide with oxygen-deficient silica. The relative concentration of mercury, as determined by XPS, was small (about 3%), and it is plausible that this small amount of mercury or mercury oxide was protected from acid attack by the silica host (except, of course, for HF). The decomposition temperature of the film was slightly lower than that of HgO ,⁷ and one would expect that elemental mercury would be driven from the film by evaporation at a much lower temperature if the film were composed of elemental mercury and SiO_2 . Therefore the most likely composition for the film is a mixture of mercury oxide and oxygen-deficient silica.

A possible growth mechanism for the film is a vapor-phase reaction between the mercury (ground-state or excited atoms, ions, or molecules) and the silicon and oxygen atoms sputtered from the silica surface by the plasma. Since mercury is only weakly adsorbed onto silica, and since no film growth has been observed in mercury cells which are exposed to resonant UV but not to a plasma discharge, the presence of the discharge is probably necessary for film growth. This hypothesis is consistent with the fact that the film accumulates mainly at the regions of weakest discharge, since any film grown in regions of strong discharge would be removed by the continuous sputtering. It is also consistent with the observation that the film appears to have been deposited from the vapor, as opposed to having grown by diffusion into the bulk.

Further experiments will be devoted toward clarifying further the chemical nature and the growth mechanism of this dark film, and toward finding modifications to the lamp wall material which will minimize the film growth.

Helpful discussions with I. Greenwood are gratefully acknowledged. This work was supported by AFOSR under Contract No. 49620-76-C-0009.

¹W. F. Meggers and F. O. Westfall, *J. Res. Natl. Bur. Stand.* **44**, 447 (1950).

²E. Jacobsen and G. R. Harrison *J. Opt. Soc. Am.* **39**, 1054 (1949).

³B. Budick, R. Novick, and A. Lurio, *Appl. Opt.* **4**, 229 (1965).

⁴L. Davis (private communication).

⁵R. Liebich and P. Fink, *Z. Chem.* **11**, 34 (1971).

⁶P. A. Heimann, J. H. Simpson, and M. J. Kelly, *Relaxation Phenomena in Optically Pumped Mercury Isotopes*, Interim Technical Report to AFOSR, Contract No. F49620-76-C-0009, KD-79-31, The Singer Co. (unpublished).

⁷*Handbook of Chemistry and Physics*, 59th ed., edited by R. C. Weast (Chemical Rubber, Cleveland, 1979).

⁸J. C. Bailar, H. J. Emeleus, R. Nyholm, and A. F. Trotman-Dickenson, *Comprehensive Inorganic Chemistry* (Pergamon, Oxford, 1973).

⁹*GMELIN Handbook of Inorganic Chemistry* (GMELIN Inst., Frankfurt, 1969), System No. 34, Vol. B4, p. 1355.

¹⁰H. Röpke and W. Eysel, *Neues Jahrb. Mineral. Monatsh.* **H 1**, 1 (1978).

APPENDIX: RESEARCH OBJECTIVES & PERSONNEL

DESCRIPTION AND OBJECTIVES

This is a basic research program for investigating the interactions that cause relaxation of an initially established nonthermal angular distribution of the nuclear spins of odd mercury isotopes. The primary long range goal of the investigation is to understand the phenomena of spin-relaxation interactions between mercury and the walls of cells made from fused silica, glass, or modifications thereof. A major requisite for achieving this primary goal is the directly related secondary goal of developing procedures for fabricating cells with stable and predictable relaxation times, mercury vapor densities, and NMR signal levels.

PERSONNEL

The following people were involved in this research effort during the period of this contract.

Donald I. Shernoff	Senior Scientist
Dr. James H. Simpson	Manager, Applied Physics Research
Ivan A. Greenwood	Manager, Advanced Research Projects
Dr. Peter A. Heimann ¹ .	Scientist
Dr. Michael J. Kelly ² .	Senior Scientist
Edward Kling	Laboratory Assistant
Ralph Patterson	Senior Scientist
Prof. Robert Novick ³ .	Consultant
Vincent Benischek ⁴ .	Staff Member
Dr. Donald S. Bayley ⁵ .	Principal Scientist
James H. Stevens	Laboratory Assistant
Joseph A. Portelli	Laboratory Associate

1. Now with Bell Laboratories
2. Now with Bell Laboratories
3. With Columbia University
4. Now with Sperry
5. Now deceased.

During the period of this contract the principal investigators, listed chronologically, were: Donald S. Bayley, James H. Simpson, Peter A. Heimann, Michael J. Kelly, and Donald I. Shernoff. This report was prepared by D.I. Shernoff. Mercury cells were produced by D.I. Shernoff and M.J. Kelly. Measurements of cell properties were performed by D.S. Bayley, J.H. Stevens, V. Benischek, P.A. Heimann, D.I. Shernoff, and J.A. Portelli. Complementary observations and quadrupole calculations were performed by P.A. Heimann. The manuscript was typed by Linda Saay.

The work was carried out at the Research Center of The Singer Company, Kearfott Division, Little Falls, N.J., except for the surface analysis of cell wall materials, which was performed at Perkin-Elmer, Physical Electronics Division, Eden Prairie, Minn. During most of the contract period the work was done in the Physics Department headed by I.A. Greenwood. The director of the Research Center was Dr. F.B. Berger, now retired.

MED
-8